

The Fabrication and Scale-Up of Organic Photovoltaic Devices via Ultrasonic Spray Coating

Nicholas William Scarratt



The
University
Of
Sheffield.

Department of Physics and Astronomy

University of Sheffield

Thesis submitted for the degree of

Doctor of Philosophy

September 2015

Acknowledgements

There are many people to thank for helping me with the last few years of my life. First I would like to thank my supervisor David Lidzey for giving me this opportunity and providing continued support, encouragement and guidance throughout my years in Sheffield. I would also like to thank Tao Wang for all the help and advice he gave me during the hours we spent together in the lab.

The EPMM group has continued to grow during my time in it, and it has been a pleasure to meet so many fantastic people. The friendships I have made within the group and the many, many conversations I have had with its members were key to my enjoyment of life both inside and outside the department and I would like to thank all those who have helped me throughout my time here. Thank you to Jon, Chris, Theo and Charlotte for our lunches, pub quizzes and countless other occasions that kept me smiling through the years.

Outside of academia, my friends have been a great source of encouragement, and I would not have been able to get where I am without them. Thank you to Josh, Mike and Dave for friendship, adventure and lively debates. Thank you to my friends from Cheshire, who still make me feel at home after all these years.

I would like to give a huge thank you to my family for always being there to listen and to give advice when needed. Their belief in me gave me the confidence to get where I am today.

Finally I would like to thank my partner Catriona for her love and support over the years we have been together. Her patience and understanding throughout my PhD helped me keep going and I couldn't have done it without her.

Abstract

At the present time, most prototype organic photovoltaic (OPV) devices are fabricated via spin-coating on to relatively small substrates. While spin-coating is a powerful tool for controllable and accurate material deposition, it is a relatively slow process and not easily scalable. In order for the technology to progress into commercial manufacturing, the fabrication of devices must be demonstrated via scalable deposition techniques.

This thesis investigates ultrasonic spray coating as a scalable technique for the fabrication of organic solar cells. Several hole transport and photoactive materials are spray-cast and characterised. OPV devices are fabricated and a partial scale up is investigated, resulting in spray-cast device metrics comparable to those fabricated via spin coating. This work details fabrication of the largest OPV devices yet reported in which the PEDOT:PSS hole transport layer and the photoactive layer are both spray coated. It is therefore suggested that that spray coating is a potentially viable roll-to-roll deposition technique.

Publications

1. T. Wang, N. W. Scarratt, H. Yi, A. D. F. Dunbar, A. J. Pearson, D. C. Watters, T. S. Glen, A. C. Brook, J. Kingsley, A. R. Buckley, M. W. a Skoda, A. M. Donald, R. a L. Jones, A. Iraqi, and D. G. Lidzey, "Fabricating high performance, donor-acceptor copolymer solar cells by spray-coating in air," *Adv. Energy Mater.*, vol. 3, no. 4, pp. 505–512, Apr. 2013.
2. J. Griffin, A. J. Pearson, N. W. Scarratt, T. Wang, D. G. Lidzey, and A. R. Buckley, "Organic photovoltaic devices incorporating a molybdenum oxide hole-extraction layer deposited by spray-coating from an ammonium molybdate tetrahydrate precursor," *Org. Electron.*, vol. 15, no. 3, pp. 692–700, Mar. 2014.
3. E. Bovill, N. Scarratt, J. Griffin, H. Yi, A. Iraqi, A. R. Buckley, J. W. Kingsley, and D. G. Lidzey, "The role of the hole-extraction layer in determining the operational stability of a polycarbazole:fullerene bulk-heterojunction photovoltaic device," *Appl. Phys. Lett.*, vol. 106, no. 7, p. 073301, Feb. 2015.
4. T. S. Glen, N. W. Scarratt, H. Yi, A. Iraqi, T. Wang, J. Kingsley, A. R. Buckley, D. G. Lidzey, and A. M. Donald, "Grain size dependence of degradation of aluminium/calcium cathodes in organic solar cells following exposure to humid air," *Sol. Energy Mater. Sol. Cells*, vol. 140, pp. 25–32, Sep. 2015.
5. T. Wang, N. W. Scarratt, H. Yi, I. F. Coleman, Y. Zhang, R. T. Grant, J. Yao, M. W. A. Skoda, A. D. F. Dunbar, R. A. L. Jones, A. Iraqi, and D. G. Lidzey, "Vertical stratification and its impact on device performance in a polycarbazole based copolymer solar cells," *J. Mater. Chem. C*, vol. 3, no. 16, pp. 4007–4015, Apr. 2015.
6. M. S. Almeataq, H. Yi, S. Al-Faifi, A. a B. Alghamdi, A. Iraqi, N. W. Scarratt, T. Wang, and D. G. Lidzey, "Anthracene-based donor-acceptor low band gap polymers for application in solar cells.," *Chem. Commun. (Camb).*, vol. 49, no. 22, pp. 2252–4, 2013.

7. J. Griffin, A. J. Pearson, N. W. Scarratt, T. Wang, A. D. F. Dunbar, H. Yi, A. Iraqi, A. R. Buckley, and D. G. Lidzey, "Organic photovoltaic devices with enhanced efficiency processed from non-halogenated binary solvent blends," *Org. Electron.*, vol. 21, pp. 216–222, Jun. 2015.
8. Y. Zhang, J. Griffin, N. W. Scarratt, T. Wang, and D. G. Lidzey, "High efficiency arrays of polymer solar cells fabricated by spray-coating in air," *Prog. Photovoltaics Res. Appl.*, p. n/a–n/a, 2015.
9. T. S. Glen, N. W. Scarratt, H. Yi, A. Iraqi, T. Wang, J. Kingsley, A. R. Buckley, D. G. Lidzey, and A. M. Donald, "Dependence on material choice of degradation of organic solar cells following exposure to humid air," *J. Polym. Sci. Part B Polym. Phys.*, p. n/a–n/a, Sep. 2015.

Conference Presentations

Oral Presentations

Edinburgh Science Festival (Invited Speaker) 2015

European Optical Society (EOS) Berlin 2014

Materials Research Society (MRS) San Francisco 2014

International Symposium on Flexible Organic Electronics (ISFOE) Thessaloniki 2013

Materials Research Society (MRS) San Francisco 2013 – Oral

European Optical Society (EOS) Aberdeen 2012 - Oral

Poster Presentations

UK Semiconductors 2014 - Poster

Hybrid and Organic Photovoltaics (HOPV) Lausanne 2014 – Poster

Winner of Conference Poster award – Second Place

Contents

Chapter 1	Introduction	11
1.1	Thesis Summary and Motivation.....	13
1.2	References	14
Chapter 2	Background Theory	16
2.1	Introduction	16
2.2	Atomic Orbitals.....	16
2.3	Orbital Hybridisation	17
2.4	Molecular Orbitals	21
2.5	Conjugated Polymers.....	23
2.6	Device Photophysics.....	25
2.6.1	Exciton Generation	25
2.6.2	Exciton Diffusion.....	28
2.6.3	Exciton Dissociation	29
2.6.4	Charge Transport	30
2.6.5	Charge Extraction	32
2.7	Device Characterisation.....	35
2.8	Device Architecture	38
2.8.1	Early Devices.....	38
2.8.2	Donor and Acceptor Bilayers	39
2.8.3	Bulk Heterojunction.....	39
2.8.4	Fullerenes	40
2.9	Donor Polymers.....	41
2.9.1	PCDTBT.....	41
2.10	Interlayers	41
2.10.1	PEDOT:PSS	42
2.10.2	Vanadium Oxide	42
2.11	Large Scale Deposition Methods.....	43
2.12	Roll To Roll Deposition Techniques	43
2.12.1	Ultrasonic Spray Coating	43

2.12.2	Doctor Blading.....	46
2.12.3	Slot Die.....	46
2.12.4	Screen Printing.....	47
2.12.5	Gravure Printing.....	48
2.12.6	Spray Coating in This Thesis.....	49
2.13	Wetting.....	49
2.13.1	Contact Angle.....	49
2.13.2	Spreading Parameter.....	50
2.14	References.....	52
Chapter 3	Device Fabrication and Characterisation	58
3.1	Spin Coating.....	58
3.2	Solution Preparation.....	59
3.3	Spin Coating and Spray Coating Comparison.....	59
3.4	Vacuum Evaporation.....	60
3.5	Device Fabrication.....	60
3.5.1	Substrate Preparation.....	60
3.5.2	PEDOT:PSS.....	60
3.5.3	Photoactive Layer.....	61
3.5.4	Cathode Layer.....	62
3.5.5	Encapsulation.....	62
3.6	Solar Spectrum Simulator.....	62
3.7	Light Beam Induced Current Mapping.....	62
3.8	Atomic Force Microscopy.....	65
3.9	Contact Angle and Surface Tension.....	66
3.10	Optical Absorption.....	68
3.11	Optical Ellipsometry.....	69
3.12	References.....	70
Chapter 4	Spray Coating and Scale Up of PCDTBT:PC₇₀BM As a Photoactive Material	71
4.1	Introduction.....	71

4.2	Chapter Summary.....	72
4.2.1	Device Preparation	73
4.3	Deposition Parameters.....	74
4.3.1	Spray Speed.....	74
4.3.2	Deposition Temperature.....	79
4.4	Materials.....	79
4.4.1	Solvent Choice	79
4.4.2	Solution Concentration.....	85
4.4.3	Film Thickness	86
4.4.4	Spray Height	88
4.5	Thermal Annealing	89
4.6	Film Uniformity	90
4.7	Scale Up	93
4.7.1	Large Area Surface Roughness.....	93
4.7.2	36 Pixel Architecture.....	94
4.7.3	Large Single Pixel	96
4.8	Conclusion.....	97
4.9	References	98
Chapter 5 Spray Coating and Scale-up of Vanadium Oxide and Molybdenum Oxide as Hole Transport Layers.....		102
5.1	Introduction	102
5.2	Chapter Summary.....	103
5.3	Device Preparation	104
5.4	Vanadium Oxide in Solution.....	105
5.5	Spray Speed and Film Thickness	105
5.5.1	Transmission of Vanadium Oxide Films.....	107
5.5.2	Spray Speed.....	107
5.5.3	Effect of Film Thickness on Device Performance	110
5.6	Surface Roughness	111
5.7	PCDTBT:PC70BM	113

5.7.1	Film Thickness	113
5.7.2	Comparison with PEDOT:PSS	114
5.8	Scale Up	117
5.9	Molybdenum Oxide in Solution	118
5.10	Scale up Of Spray Cast Molybdenum Oxide	118
5.11	Conclusion	120
5.12	References	120
Chapter 6 Spray Coating and Scale Up of PEDOT:PSS as a Hole Transport Layer		122
.....		122
6.1	Introduction	122
6.2	Chapter Summary	123
6.3	IPA As a Wetting Agent	124
6.4	Ethyl Glycol as a Binding Agent.....	125
6.5	Device Preparation.....	126
6.6	Film Thickness	127
6.7	Film Uniformity	129
6.8	Spray coating PEDOT:PSS and PCDTBT:PC ₇₀ BM	130
6.9	Scale Up	131
6.9.1	Large 36 Pixel	132
6.9.2	Large Four Pixel.....	138
6.10	Conclusion	141
6.11	References	142
Chapter 7 Conclusions and Further Work		144
7.1	Conclusions	144
7.2	Further Work	145
7.3	References	146

Chapter 1 Introduction

As the energy demands of society increase, energy generation must increase to meet them. Due to environmental concerns and limited fossil fuel resources, renewable energy sources are becoming increasingly important. In 2014, 5.3% of global power generation was from renewable sources such as wind, solar, hydrothermal, biofuels and waste [1] (excluding hydroelectric). Energy from sources other than fossil fuels, including nuclear and hydroelectric, contributed over 17% of the world total.

Worldwide electricity generation in 2014 was over 23 thousand terawatt-hours, a 1.5% increase from that of 2013 [1]. Around 885 million terawatt-hours of sunlight reach the Earth's surface every year. Harnessing a fraction of this energy could therefore help to match the world's increasing energy consumption. Sunlight can be harvested via solar photovoltaic cells, which convert incident sunlight into an electrical energy via the photoelectric effect. If the sun is directly overhead, the amount of atmosphere that light must travel through to reach the Earth's surface is defined as one atmosphere, or air mass one (AM1). This is only the case in equatorial regions however, and the tilt of the Earth requires sunlight to travel through more air to reach the ground at other latitudes. Many of the Earth's population centres are at a latitude mid-way between the equator and the pole, therefore a standardised reference solar spectrum was developed based on these locations[2]. Figure 1-1 shows solar irradiance at the Earth's surface as a function of wavelength at an air mass of 1.5 and a zenith angle of 48.2° . An integrated flux over the wavelength range is also displayed.

Solar cells based on silicon were discovered over 60 years ago in 1941, with power conversion efficiencies (PCE) of <1%. This was improved upon over the next decade, with 10% efficiency cells fabricated in 1955 [3]. Single crystal silicon panels have now reached a record PCE of ~25% [4]. The low band gap (1.1 eV, 1127 nm) and high dielectric constant (~12) of silicon makes it an efficient light harvester, as even

low energy photons can excite electrons to the conduction band of the material and charges are easily separated.

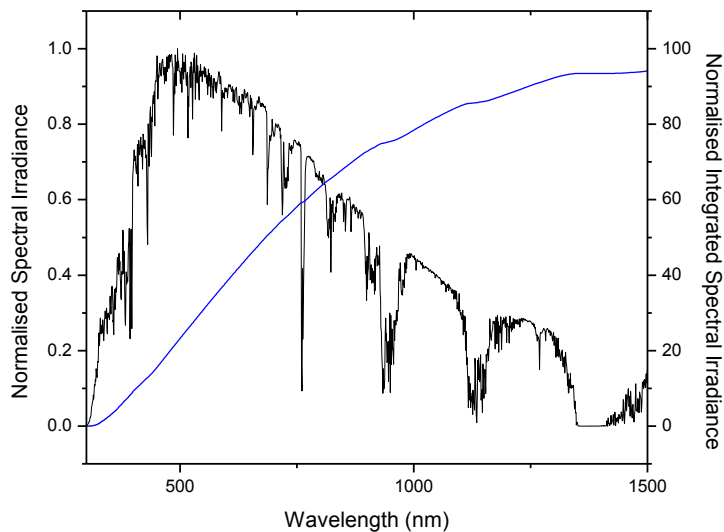


Figure 1-1: Normalised AM1.5 solar spectrum and integrated flux.

Other popular photovoltaic materials include gallium arsenide (Gas), indium phosphate (Imp) and cadmium telluride (Cite), which have achieved PCEs of 29%, 22% and 21% respectively.

Efficiencies are not the only metric by which each system must be measured however, as factors such as energy pay-back time, scarcity of materials, toxicity, cell thickness and weight must also be considered.

A potentially low-cost alternative solar cell technology is organic photovoltaic's (OPV). This research field aims to produce solar cells from polymer materials for a much lower cost than traditional silicon. The goal is to produce low-cost, light-weight, flexible solar cells via roll-to-roll fabrication. The materials here on deposited from solution, allowing rapid deposition processes to be used. The high absorption coefficient and low charge motilities of the polymer materials result in optimum thicknesses of <100 nm. This allows the production of solar cells on flexible substrates such as PET in a roll-to-roll environment.

Within the OPV research field, there has been a not-unreasonable tendency to push for higher efficiency 'hero' devices. This is achieved more easily with smaller device sizes and small-scale accurate deposition methods such as spin coating. While this push for higher performing materials is a very important part of the development process, the reality of taking a material or deposition system from laboratory testing to large scale manufacture is often overlooked. There are however many research groups now working on scale up processes and some have constructed roll-to-roll systems to fabricate large sheets of OPV cells [5].

1.1 Thesis Summary and Motivation

This thesis aims to investigate the feasibility of an ultrasonic spray coating process for scale up of OPV devices. Both solution processed layers in an OPV device are spray cast and spray-cast devices achieve comparable device performances to spin-cast references. The spray coating process is then used to scale up device sizes from those typically seen in the literature to a size more consistent with industrial requirements.

Chapter 2 provides an overview of the background theory of organic semiconductors and their use within organic photovoltaic devices. Potential scale-up deposition techniques and the progress towards roll-to-roll production is also discussed.

Chapter 3 details the experimental techniques used to fabricate and characterise the OPV materials and devices within this thesis.

Chapter 4 is the first experimental chapter, wherein an ultrasonic spray coating process is optimised for the deposition of PCDTBT:PC₇₀BM active layers. The ultrasonic spray coater deposition technique is investigated and the following parameters explored: solvent blend, spray speed, solution concentration, deposition temperature, layer thickness and spray height. An optimised process is then used to fabricate devices, with a maximum PCE of 4.79% achieved. The process was then applied to a large scale 36-pixel device, achieving a 100% yield and

efficiencies above 3.5%. Finally, a 900mm² single pixel is fabricated with a PCE of 1.75% achieved. Light beam induced current maps show a variation in photocurrent generation across the cell.

In **Chapter 5**, a spray coating process is been optimised for the metal oxide hole transport layers vanadium oxide and molybdenum oxide. Small-area devices are fabricated and performances matched those of devices with spin cast PEDOT:PSS hole transport layers of around 5% PCE. Film uniformity is characterised via atomic force microscopy, showing that the vanadium oxide film matches the surface morphology of the ITO substrate on to which it is cast. Large 36 pixel devices are then fabricated, providing high pixel yields of 86% and 89% for vanadium oxide and molybdenum oxide devices respectively.

Chapter 6 describes the formulation of an ink for deposition of the hole transport material PEDOT:PSS. By combining an aqueous solution with isopropyl alcohol and ethylene glycol, wetting is improved on an ITO surface. OPV devices are then fabricated via spray casting the PEDOT:PSS layer and spin casting a PCDTBT:PC₇₀BM active layer, achieving efficiencies of ~5%. The PCDTBT:PC₇₀BM layer is also spray cast during fabrication, creating devices wherein no layer is spin cast. The spray coating process is then scaled up to larger substrate areas, and large device architectures are fabricated. A 36 pixel architecture achieves similar results to the small device sizes, indicating that the film is unchanged when spray cast over a larger area. A large four pixel device structure shows a decrease in performance when compared with the small area devices, potentially due to a mottling effect created by the drying film.

Chapter 7 presents conclusions on the findings of this thesis and potential future work.

1.2 References

- [1] British Petroleum, "BP Statistical Review of World Energy, June 2015," *Nucl. Energy*, no. June, p. www.bp.com/statisticalreview, 2015.

- [2] C. A. Gueymard, D. Myers, and K. Emery, "Proposed reference irradiance spectra for solar energy systems testing," *Sol. Energy*, vol. 73, no. 6, pp. 443–467, Dec. 2002.
- [3] M. A. Green, "The path to 25% silicon solar cell efficiency: History of silicon cell evolution," *Prog. Photovoltaics Res. Appl.*, vol. 17, no. 3, pp. 183–189, 2009.
- [4] P. K. Nayak and D. Cahen, "Updated Assessment of Possibilities and Limits for Solar Cells," *Adv. Mater.*, vol. 26, no. 10, pp. 1622–1628, Mar. 2014.
- [5] F. C. Krebs, N. Espinosa, M. Hösel, R. R. Søndergaard, and M. Jørgensen, "25th anniversary article: Rise to power - OPV-based solar parks," *Adv. Mater.*, vol. 26, no. 1, pp. 29–39, 2014.

Chapter 2 Background Theory

2.1 Introduction

In order to understand how variations in the performance of organic photovoltaic devices arise, a detailed understanding of the optoelectronic properties involved and the physical phenomena of device fabrication is required. The origin of the semiconducting properties of organic materials is fundamental to this understanding. This chapter introduces the background theory behind the photophysics, fabrication and characterisation of organic photovoltaic devices.

2.2 Atomic Orbitals

Electrons surrounding an atom are located in discrete energy levels called orbitals [1]. The characteristics of these orbitals depend on their four quantum numbers: the principle quantum number and potential energy of the electron (n), the magnitude of electron's angular momentum (l), the orientation of the electron's angular momentum (m_l), and the spin direction of the electron (m_s). The quantum numbers n , l and m_l all have integer values, while m_s has a value of $\pm 1/2$. The values of these numbers are determined by the conditions:

$$1 \leq n \quad \text{Equation 2.1}$$

$$0 \leq l \leq n - 1 \quad \text{Equation 2.2}$$

$$-l \leq m_l \leq l \quad \text{Equation 2.3}$$

$$-s \leq m_s \leq s \quad \text{Equation 2.4}$$

These are used to calculate the quantum numbers of each atomic orbital, determining their shape and how many electrons they can contain. No two electrons in a shell can share all of the same quantum numbers due to the Pauli Exclusion Principle. This means that the total number of electrons that can occupy a shell is the number of the possible combinations of quantum numbers for that shell.

S orbitals have a quantum number of 1 and an angular momentum quantum number of 0, therefore there can only be two electrons in an s shell. P Orbitals however can have an angular momentum quantum number of 1, allowing for more combinations of quantum numbers and up to 6 electrons within the shell. For example, the first atomic orbital is called the 1s shell and can contain two electrons corresponding to the two possible spin direction quantum number (m_s) values. The possible quantum numbers of the first two orbitals are shown in Table Chapter 2-2-1 [2].

n	l	m_l	m_s	Orbital Name	Total Electrons	
1	0	0	+1/2	1s	2	
			-1/2			
2	0	0	+1/2	2s	2	
			-1/2			
	1	-1	-1	+1/2	2p _x	6
				-1/2		
		0	0	+1/2	2p _y	
				-1/2		
1	1	1	+1/2	2p _z		
			-1/2			

Table Chapter 2-2-1: Properties of the first two shells including quantum numbers, orbital names and the total number of electrons that a shell can contain.

The angular momentum direction m_l for the 2p orbitals can have three values, creating three equally energetic orbitals 2p_x, 2p_y and 2p_z.

2.3 Orbital Hybridisation

A classical polymer such as PMMA and polystyrene comprises a series repeated covalently bound organic monomers, and is an electrical insulator. There are however certain types of polymer that exhibit electronic properties similar to those

of semiconductors. This section explores the formation and behaviour of the molecular orbitals, which confer semiconducting properties.

There are six electrons in a neutral carbon atom, all filling positions in the atomic orbitals. An inner orbital containing two electrons ($1s^2$) is surrounded by a second s-orbital with two more electrons ($2s^2$) and finally two p-orbitals, each with one electron ($2p_x^1$ and $2p_y^1$) [3], with the electronic configuration being $1s^2 2s^2 2p_x^1 2p_y^1$. In a carbon atom, there are four unoccupied orbitals in the outermost 2p shell. Due to the Pauli Exclusion Principle, there is no more room for another electron in the 2s orbital, therefore this leaves only 2 p-orbital electrons free to form covalent bonds. This is not enough to fill the entire outer p-orbital. A lack of available bonding electrons can be overcome via a process called hybridisation.

If a 2s electron is promoted to an empty 2p orbital ($2p_z$), the electronic configuration becomes $1s^2 2s^1 2p_x^1 2p_y^1 2p_z^1$. In this state, there are now four electrons free for use in bonding. Hybridisation is the process in which the 2s orbital combines with one or more of the 2p orbitals to create a new orbital (sp), with an energy level lying between the original 2s and 2p orbitals (Figure 2-1) [3].

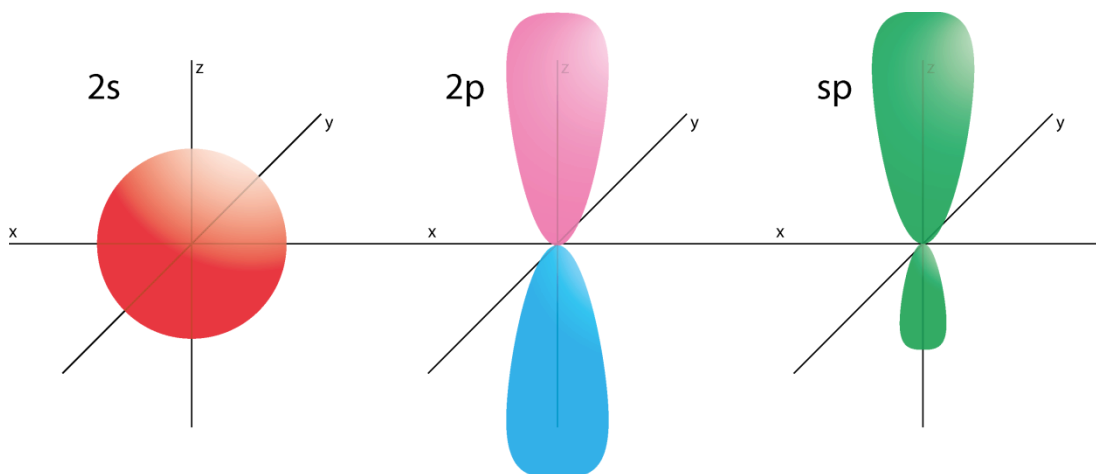


Figure 2-1: Hybridisation of a 2s and a 2p orbital into an sp orbital.

There are three possibilities (sp^1 , sp^2 and sp^3), depending on how many p orbitals the s orbital hybridises with. These are displayed in Figure 2-2.

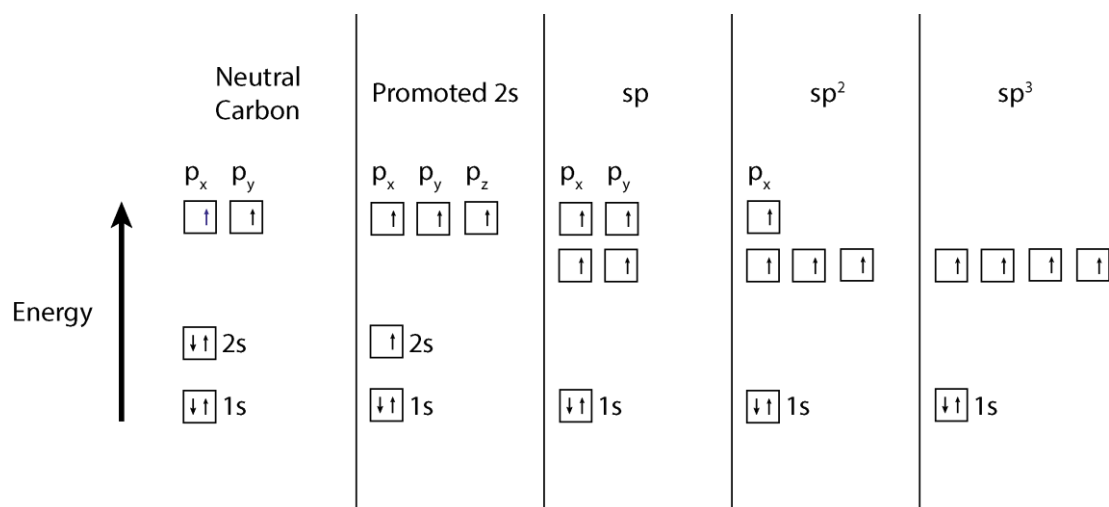


Figure 2-2: Orbital Hybridisation Possibilities.

In the case of a semiconducting polymer, sp^2 hybridisation is the process responsible for their electronic properties. When sp^2 hybridisation occurs, the electronic configuration becomes $1s^2sp^3p_z^1$ as shown in Figure 2-3. The sp^2 orbitals form a trigonal arrangement on a common plane, with bond angles of 120° . The remaining p orbital is perpendicular to the sp^2 orbitals.

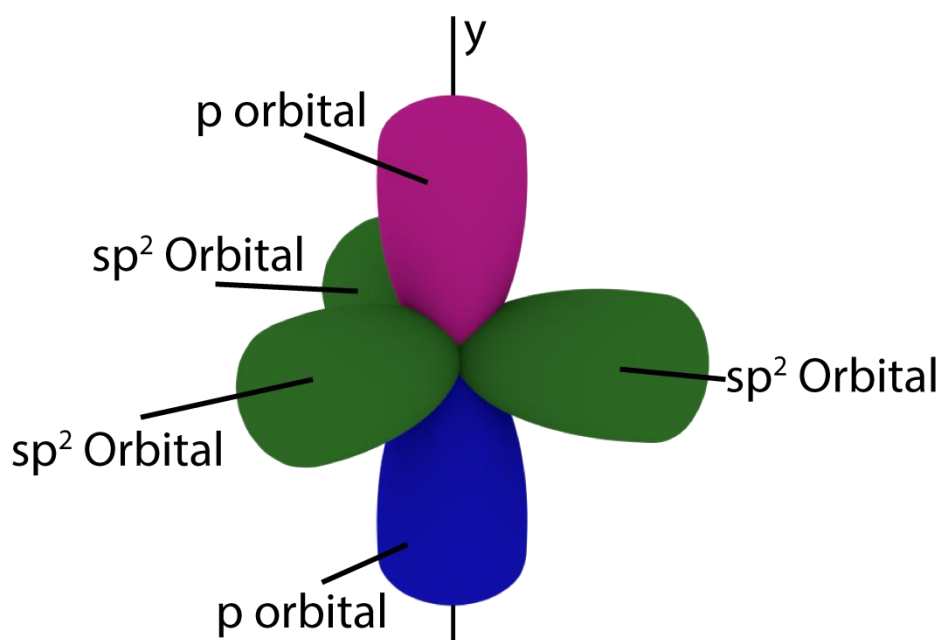


Figure 2-3: Orbitals of a Carbon atom that has undergone sp^2 hybridisation. The small components of the sp^2 orbitals are not shown.

The sp^2 orbitals of a hybridised carbon atom can bind with the sp^2 orbitals of neighbouring carbon atoms to create a sigma bond, which is cylindrically symmetric along the internuclear axis (Figure 2-4). The $2p_z$ orbitals are perpendicular to this axis and therefore cannot merge to create a sigma (σ) bond. As the $2p_z$ orbitals from neighbouring atoms approach each other, they create a pi (π) bond by pairing electrons. The π bonds are weaker than the σ bonds and are therefore not as localised. A σ bond on its own is called a single bond, and a σ bond combined with a π bond is called a double bond.

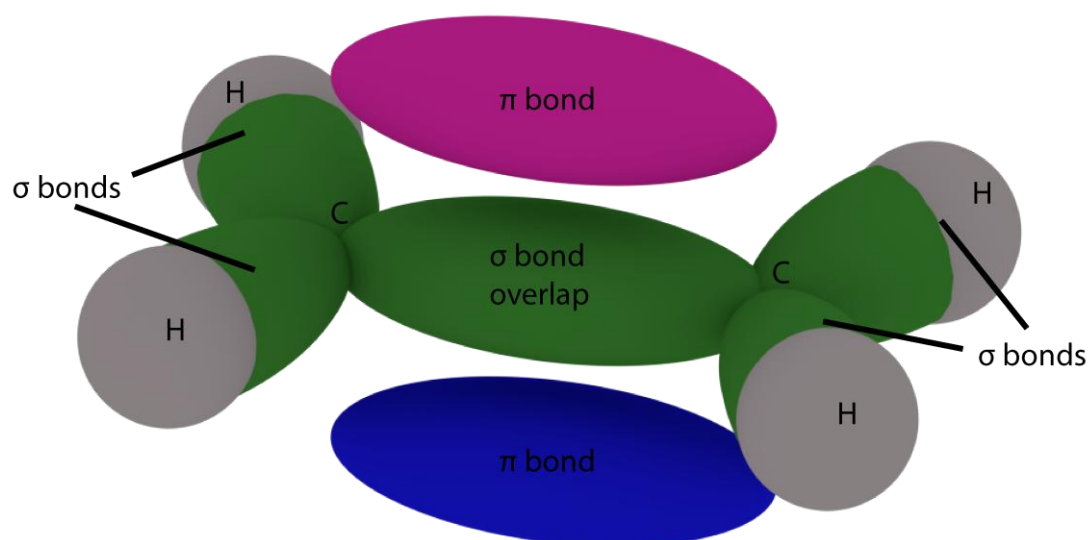


Figure 2-4: Two sp^2 hybridised Carbon atoms combining with each other and four Hydrogen atoms to form Ethylene. The sp^2 orbitals overlap to form a σ bond. The p orbitals also overlap, forming a π bond.

2.4 Molecular Orbitals

When two sp^2 hybridised atoms come together as in Figure 2-4, their wavefunctions (ψ) overlap and combine into molecular orbitals. These orbitals have two different energy levels, one higher and one lower in energy than the original atomic energy levels. Figure 2-5 shows the amplitude of two atomic wavefunctions, $\psi(A)$ and $\psi(B)$. As they come together, the wavefunctions overlap to create the $\psi(A) + \psi(B)$ bonding (π) and $\psi(A) - \psi(B)$ antibonding (π^*) orbitals via constructive and destructive interference [4]. The bonding orbital has a non-zero electron density at the centre point between the nuclei whereas the antibonding orbital has zero electron density.

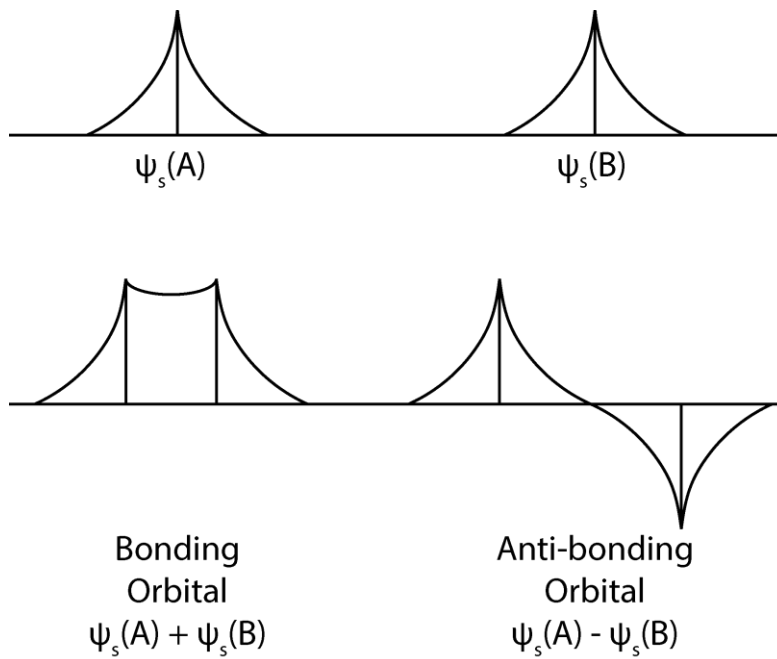


Figure 2-5: Atomic wavefunctions combining to create bonding and antibonding orbitals.

The superposition of these molecular orbitals in a solid gives rise to bands of bonding and antibonding orbitals (Figure 2-6). The highest occupied molecular orbital (HOMO) and the lowest unoccupied molecular orbital (LUMO) band act as the traditional semiconductor valence and conduction band respectively. The energy difference between the HOMO and LUMO is the energy gap (E_g).

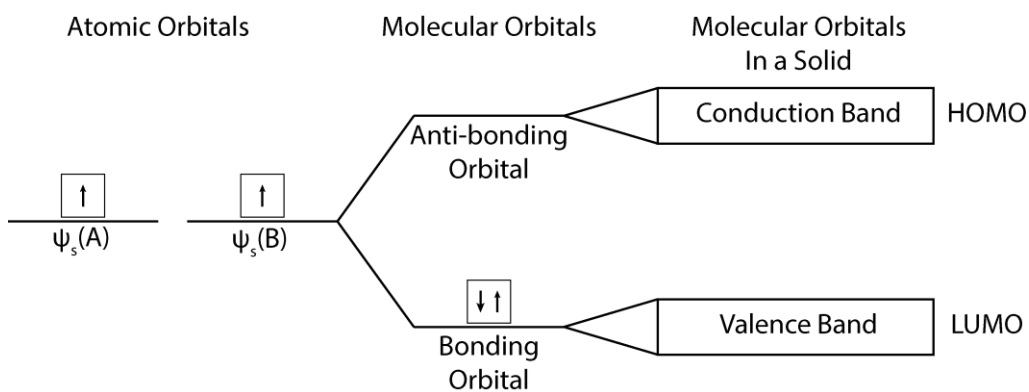


Figure 2-6: Molecular orbital band formation in solids.

2.5 Conjugated Polymers

The most favourable arrangement of the orbitals in the sp^2 hybridised Carbon atom is shown in Figure 2-3. If the sp^2 carbon atom was bound to 5 other sp^2 carbon atoms while maintaining its trigonal 60° bond angle, the result would be a hexagonal arrangement as shown in Figure 2-7. This is known as a benzene ring and it is conjugated, which means that it has alternating single and double bonds along its carbon chain. The positioning of the double bonds does not make a difference to its electronic properties therefore, and the two configurations on the left of Figure 2-7 can be expressed as a ring of delocalised electrons shown on the right. π electrons are completely delocalised along the alternating single and double bonds. Benzene is a popular aromatic hydrocarbon and is often used as a building block within a semiconducting polymer.

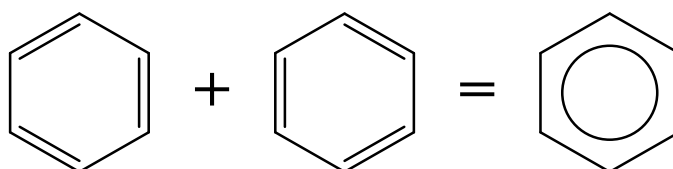


Figure 2-7: A benzene ring made up of six sp^2 carbon atoms.

Figure 2-8 shows two similar polymer chains, polyethylene and polyacetylene. Polyethylene is the combination of several of the Ethylene monomers from Figure 2-4 however it loses its double bond when it bonds with another Carbon atom. Figure 2-8b and d are drawn using a skeletal form, where the Carbon and Hydrogen atoms are hidden. This is a common way of representing organic molecules.

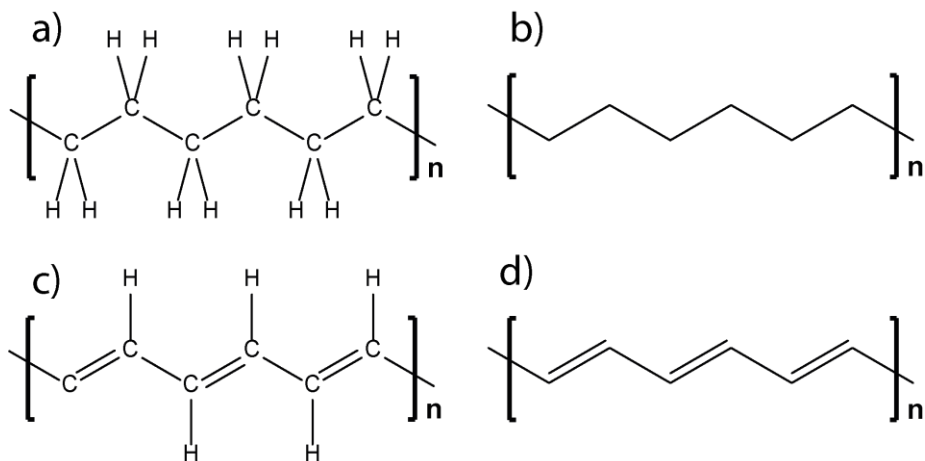


Figure 2-8: Chemical structures with and without labelled carbon and hydrogen of a-b) polyethylene and c-d) polyacetylene.

If carbon atoms were equidistant from each other, then there would be no difference between the bonding and antibonding states. The π electrons would be delocalised along the polymer chain and there would be no energy gap; the polymer would be quasi-one-dimensional metal as its band would be half filled [5]. This is however not the case, as measurements show that there is a difference in bond lengths between carbon atoms in a conjugated polymer. Figure 2-9a shows a carbon chain with equidistant atoms and equal bond lengths. Figure 2-9b demonstrates Peierls instability, wherein the polymer chain distorts and double bonds become shorter, while single bonds become longer. In the case of polyacetylene, Yannoni and Clarke measured the double and single bond lengths as 1.36Å and 1.44Å respectively [6].

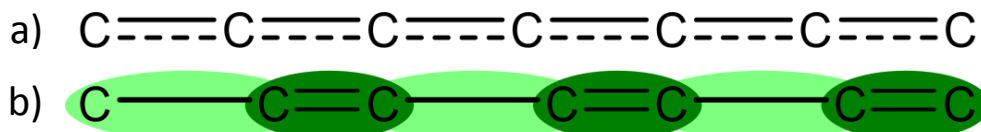


Figure 2-9: Alternating bond lengths creating regions of varying electron density along the polymer chain.

After this bond length alteration, the bonding state becomes more energetically stable than the antibonding state. The half filled band becomes two bands: a fully occupied valence band and an empty conduction band, analogous to a traditional semiconductor material. This separation into two bands is what affords a polymer

its semiconducting behaviour. Unlike polyethylene, polyacetylene therefore demonstrates semiconducting properties due to its conjugated backbone [3].

2.6 Device Photophysics

2.6.1 Exciton Generation

Figure 2-10 shows the singlet ground and excited states in an energy level diagram based on the Frank-Condon principle. These singlet states contain several quantised vibrational modes (n) which form a ladder of states. If the ground and excited state are labelled as S_0 and S_1 respectively, then these vibrational modes can be labelled as $S_{0,n}$ and $S_{1,n}$. A ground state electronic transition occurs when a photon is absorbed by an electron in the S_0 state with energy equal to or greater than the energy gap. As this photoexcitation transition occurs on a shorter timescale than the motion of the nuclei, they can be considered stationary and the transition is depicted by a vertical line in the energy level diagram.

Should the absorbed photon have an excess of energy compared to that of the energy gap, the electron is promoted to one of the S_1 vibrational modes. The electron then quickly relaxes via a non-radiative decay process to the lowest vibrational mode of the excited singlet state ($S_{1,0}$). This occurs over timescales of ~ 0.1 ps.

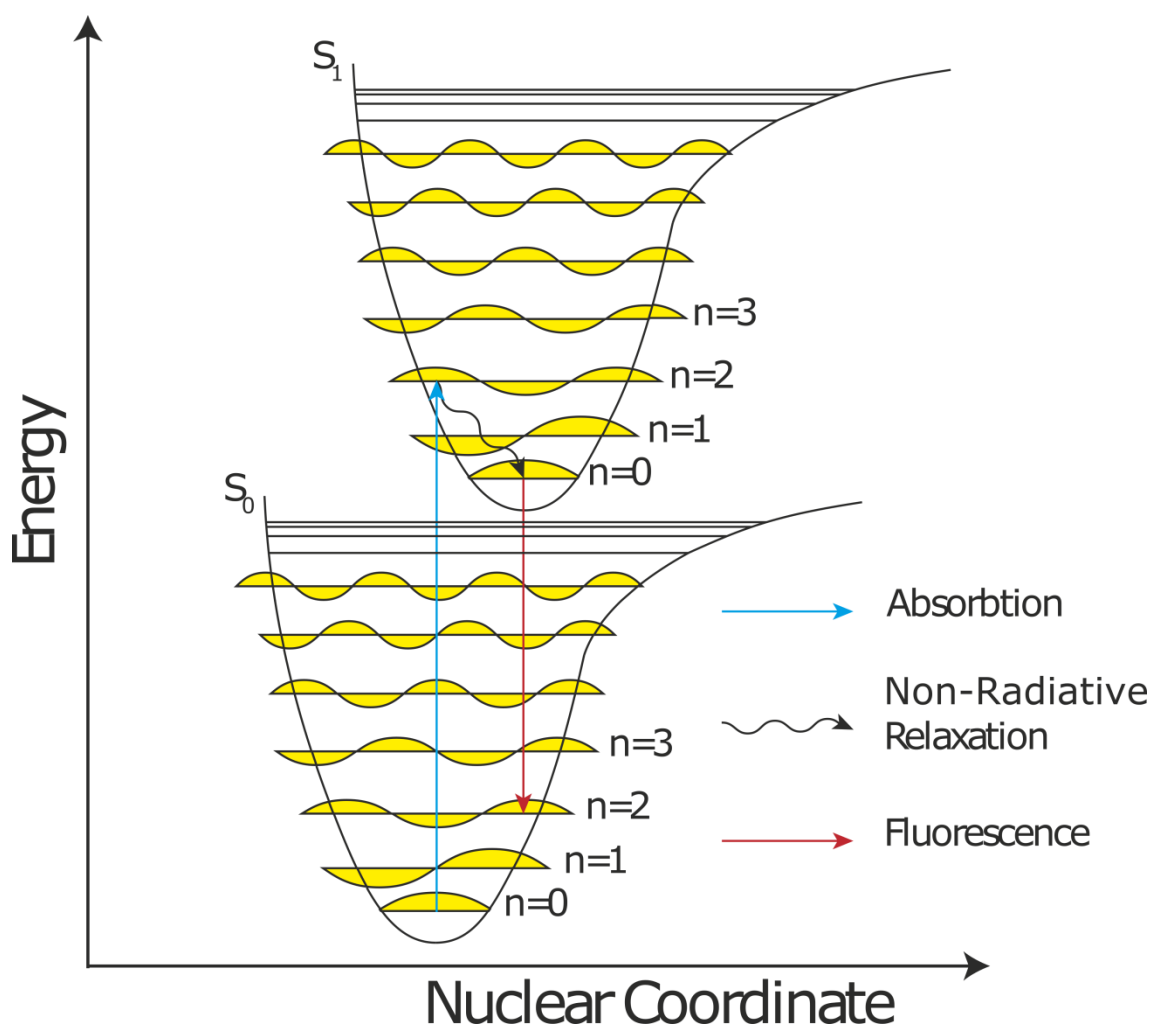


Figure 2-10: A Frank-Condon Diagram showing the processes that occur during photoexcitation.

The promotion of an electron to an excited state leaves a “hole” in the ground state. This “hole” can be considered as a particle having a charge equal and opposite to that of the electron. The electron-hole pair is coulombically bound with a neutral net charge and is termed an exciton. If no external factor acts upon the exciton, it will recombine as the electron decays radiatively to one of the S_0 vibrational states in a process called fluorescence. This decay occurs on the timescale of 100 to 1000 ps, a much longer period than that of the vibrational relaxation [7]. This difference in timescales means that the decay to one of the S_0 states will occur from the $S_{1,0}$ state, regardless of the initial photon energy. Transfer between singlet states can occur if the wavefunctions of vibrational modes overlap. An example of this is shown using the $S_{1,0}$ and $S_{0,2}$ states in Figure 2-10. In this case,

the higher the energy of the ground state vibrational mode ($S_{0,2}$), the lower the energy of the photon emitted during fluorescence.

The transition can be expressed in terms of the electron wavefunction. As discussed earlier in section 2.2, electrons can have a spin of $\pm \frac{1}{2}$. Electron wavefunctions may combine with other electrons or holes to produce a total spin (S) of 0 ($+\frac{1}{2} - \frac{1}{2}$) or 1 ($+\frac{1}{2} + \frac{1}{2}$). The wavefunction of the ground state S_0 is given by

$$\Psi_{S_0} = (|\uparrow\downarrow\rangle) \quad \text{Equation 2.5}$$

and has a total spin of $S = 0$. The wavefunction Ψ of the excited singlet state also has a total spin of $S = 0$ and is asymmetric under particle exchange. It can be expressed as

$$\Psi_{S_1} = \frac{1}{\sqrt{2}}(|\uparrow\downarrow\rangle - |\downarrow\uparrow\rangle) \quad \text{Equation 2.6}$$

The $S = 1$ case can be achieved by three symmetric wavefunction configurations called triplet states; these are listed in Equation 2.7.

$$\Psi_{S_1} = \frac{1}{\sqrt{2}}(|\uparrow\downarrow\rangle + |\downarrow\uparrow\rangle), \quad \Psi_{S_1} = (|\uparrow\uparrow\rangle), \quad \Psi_{S_1} = (|\downarrow\downarrow\rangle) \quad \text{Equation 2.7}$$

The probability for specific transitions to occur depends on the symmetry of the wavefunction. The Pauli Exclusion Principle states that two particles must have a total wavefunction that is asymmetric under particle exchange. For an optical transition, the change in S (ΔS) must equal 0 and the change in angular momentum (ΔL) must be non-zero. The angular momentum of the photon provides this change in angular momentum. The transition from S_0 to S_1 in Figure 2-10 satisfies this condition for instance, as the states have angular momentums of 0 and 1. Fluorescence is then possible from the S_1 to S_0 states as a photon is emitted, again providing a change in angular momentum.

For a S_1 to T_1 transition to occur, there would need to be a change in total spin as all of the triplet states have a total spin of 1. This spin-forbidden transition can occur

via spin-orbit coupling, which is an interaction between the spin of an electron and its orbital angular momentum. This interaction allows the S_0 to T_1 transition to occur, as long as the spin of an electron ‘flips’ and the total spin becomes 1. Relaxation via emission of a photon from the T_1 state to the ground state can occur in a process called phosphorescence, however this happens on much longer timescales (μs) than singlet fluorescence (ns) [8]. Triplet states therefore have a longer lifetime than singlet states.

A phonon is a quantised mode of vibrational energy created by oscillations in a lattice. Unlike in inorganic materials, electron-phonon interactions in organic semiconductors are comparable in strength to electronic interactions [9]. The electron interaction with a phonon can be considered a quasi-particle called an electron-polaron. When an electron enters the excited state in a conjugated polymer, the surrounding molecular structure undergoes a relaxation. The relaxation in surrounding bonds acts to lower the energy of the system, and the LUMO level is reduced. The presence of a hole in the HOMO level also causes a deformation in the polymer chain, creating a hole-polaron and reducing the depth of the HOMO energy. This brings the electron and hole closer together, thus increasing their coulombic attraction.

2.6.2 Exciton Diffusion

The Coulombic attraction between the electron and hole is given by

$$V = \frac{e^2}{4\pi\epsilon_r\epsilon_0 r} \quad \text{Equation 2.8}$$

where e is the charge of an electron ϵ_r is the dielectric constant of the medium, ϵ_0 is the permittivity of free space and r is the distance between the charges. Organic photovoltaic materials have comparatively small dielectric constant ($\epsilon_r \approx 2-4$) when compared to a more traditional silicon semiconductor ($\epsilon_r \approx 12$) [7]. The resultant increase in coulombic attraction means that charges are not affectively screened and maintain a binding energy that is much larger than $k_B T$. The exciton cannot

therefore be dissociated by thermal means alone. This bound pair is known as a Frenkel exciton. In order to prevent the charges recombining, the exciton needs to travel to an interface with a favourable energy for charge dissociation. The exciton can 'hop' between the localised states along a polymer chain, or from one chain to another within a material domain. Equation 2.9 gives the length travelled (L_D) by an exciton before recombination occurs. This is calculated by the diffusion coefficient (D) and the photoluminescence decay lifetime (τ).

$$L_D = \sqrt{D\tau} \quad \text{Equation 2.9}$$

During this process, the electron hole pair is considered neutrally charged and therefore is not directed by the electric field within the device. If the exciton reaches an interface within this diffusion length, it can be separated into free charge carriers. In a conjugated polymer, this length is of the order of 10nm [10]. This short length scale can be addressed by tuning the morphology of the active layer materials in order to minimise the distance between exciton generation and a suitable interface. This will be discussed in more detail in section 2.8.

2.6.3 Exciton Dissociation

An exciton is dissociated if the electron and hole are separated into free charge carriers. This can occur at the interface between the conjugated polymer donor and the acceptor material, as long as it is energetically favourable to do so [11]. Figure 2-11 displays the dissociation process in stages.

An electron is excited in part a), creating a bound electron-hole pair. If the LUMO of the acceptor material is further from the vacuum level than the LUMO of the donor level, a driving force acts upon the excited electron and it can transfer to the acceptor LUMO as shown in part b). The donor and acceptor LUMO energies must be offset by an energy ΔE greater than the binding energy of the exciton ($\sim 0.3\text{eV}$) [12][13]. The HOMO of the donor material must also be further from the vacuum level than the HOMO of the acceptor material; otherwise both the electron and the hole could travel to the acceptor. In this case, only energy transfer would occur

instead of charge transfer, as the exciton pair would be travelling to the acceptor together.

The electron and hole are still spatially close at this point, and due to the low dielectric constants in the materials, the electron and hole are still bound in what is known as a geminate pair. A geminate pair is a bound electron-hole pair in which the hole was created by the same electron that it is bound to [7].

If a suitably strong electric field acts upon the pair, they can separate into free charges. If this field is not present however, the charges can recombine via transfer of the electron from the acceptor LUMO back to the donor HOMO in a process called geminate recombination.

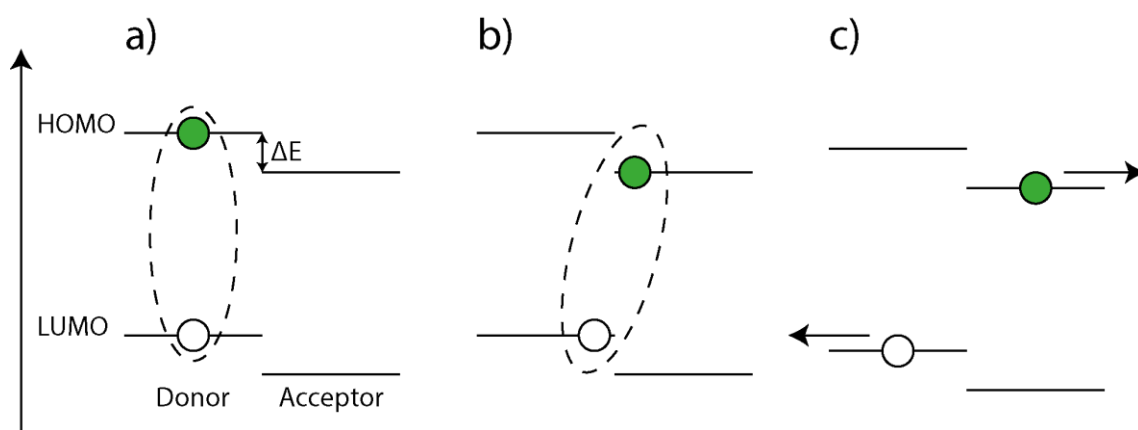


Figure 2-11: a) An excited electron is still coulombically bound with its hole in an exciton pair. b) The electron is transferred to the HOMO level of the acceptor material. The charges are still bound together c) an electric field allows the bound pair to separate in to two free charges.

2.6.4 Charge Transport

Upon dissociation into free charge carriers, the electron and hole must reach electrodes in order for the photocurrent to be successfully extracted. Free charges can still recombine with unassociated charge carriers via bimolecular recombination before they reach their respective electrodes for extraction.

As discussed in section 2.5, a conjugated polymer has localised sites of differing electron densities along its backbone. The free charge can move from one site to

another via intramolecular transport along the polymer. The charges must also move via intermolecular travel to other donor/acceptor materials if they are to reach their corresponding electrodes.

Organic semiconductors are disordered materials and there is little coupling between individual molecules. The transition of a charge from one localised state to another is therefore described as ‘hopping’ instead of a band like charge transport. Charges must hop between polymer segments and also between separate polymer molecules. This hopping process is dependent on the temperature and the presence of an electric field.

We can estimate the energetic distribution of the sites $g(E)$ of charge transport via a Gaussian distribution of disordered states [14].

$$g(E) = \frac{1}{\sqrt{2\pi}\sigma} \exp\left(-\frac{E^2}{2\sigma^2}\right) \quad \text{Equation 2.10}$$

The disorder parameter σ characterises the width of the density of states and increases with system disorder.

If there is no electric field present, the charges can diffuse towards lower energy states. The hopping rate v_{ij} between the occupied site i and the unoccupied site j can be described by the Miller-Abrahams equation [15]:

$$v_{ij} = v_0 \exp\left(-2\gamma\alpha \frac{r_{ij}}{a}\right) \begin{cases} \exp\left(-\frac{E_j - E_i}{kT}\right) & \text{if } E_j > E_i \\ 1 & \text{if } E_j < E_i \end{cases} \quad \text{Equation 2.11}$$

The factor v_0 is the attempt to escape frequency. The jump distance between sites r_{ij} is normalised by the inter-state distance a . γ is the coupling matrix element between sites and E_i and E_j are the energies at site i and j respectively. When site i is at a higher energy than site j , charge transport between the sites is energetically

favourable. If the charge carrier hops to a site that is lower in energy than all of its surrounding sites, it can become trapped.

An electric field can be introduced either externally or via the difference in electrode work function in fully fabricated solar cell. When an electric field is applied, the density of states is tilted and the activation energy for charge transport is lowered.

2.6.5 Charge Extraction

Upon reaching the appropriate electrode, free charges must transfer from the donor to the anode and the acceptor to the cathode. The morphology of the film can aid or hinder this process. For instance, if there is a domain of donor material between the acceptor and the cathode, the free electrons can be lost in the acceptor via bimolecular recombination.

Figure 2-12a) depicts two metal materials in vacuum-level aligned and Fermi-level aligned configurations. A metal-metal contact occurs at the cathode of the OPV devices in this thesis, in the form of a calcium/aluminium interface. When the materials come in to contact, electrons from the metal with the shallower Fermi level flow in to the metal with the deeper level. This flow of electrons aligns the Fermi levels of the two materials.

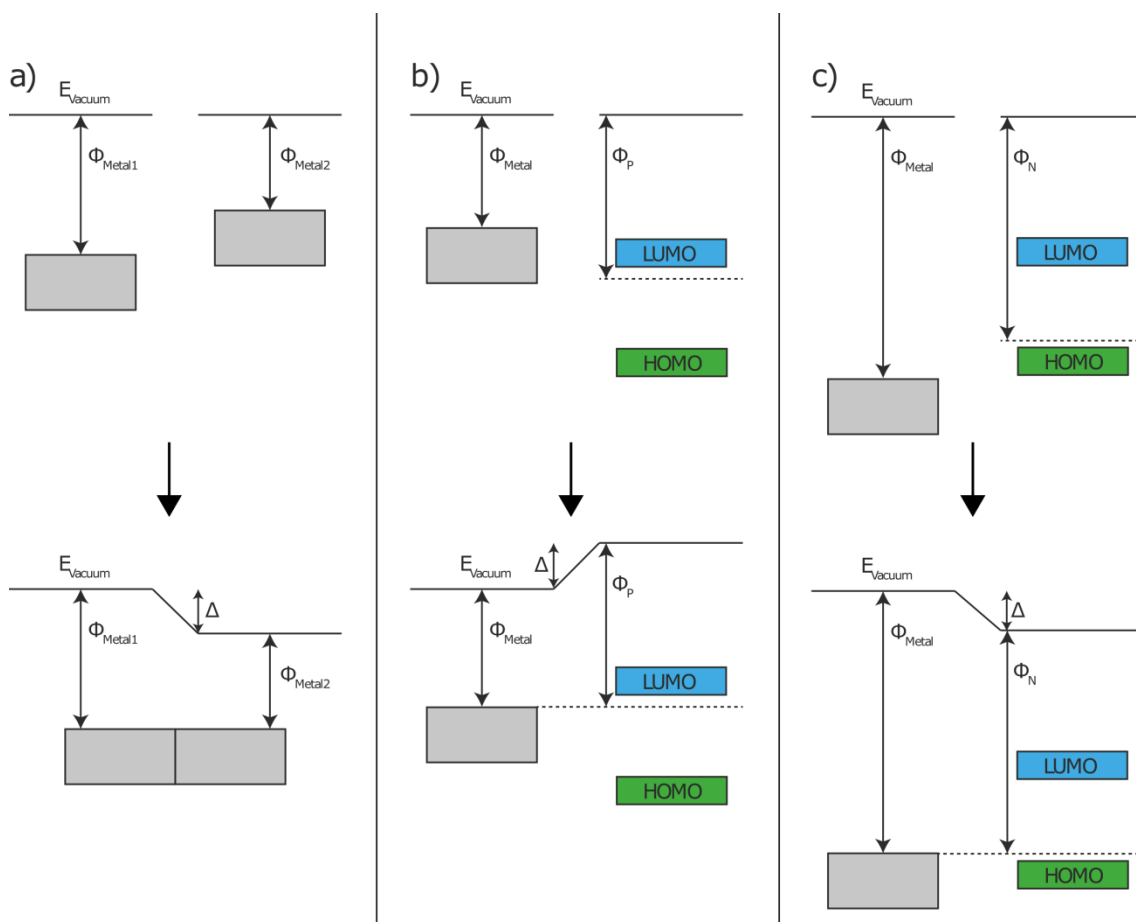


Figure 2-12: Energy level alignment via electron transfer between interfaces of work function Φ , showing the energy difference Δ between vacuum alignment and fermi level alignment. a) a metal/metal interface, b) a metal/organic interface when $\Phi_{Metal} < \Phi_P$ and c) a metal/organic interface when $\Phi_{Metal} > \Phi_N$.

In the case of a metal/organic contact shown in Figure 2-12b, the metal work functions (Φ_{Metal}) ideally align with the HOMO or LUMO of the organic materials as described by Equation 2.12 and Equation 2.13.

$$\phi_{anode} \leq HOMO_{donor} \quad \text{Equation 2.12}$$

$$\phi_{cathode} \geq LUMO_{acceptor} \quad \text{Equation 2.13}$$

This would create an ohmic contact between the two materials. In reality however, work functions and molecular orbitals are rarely so closely aligned.

The transfer of charges across the metal/organic interface can be described by the integer charge-transfer model. This model assumes that metal/organic interfaces

are passivated by oxides or residual hydrocarbons, which block the formation of interface dipoles. Electron transfer can still occur via tunnelling through this passivating layer however, as long as the layer is thin enough [16]. An integer amount of electrons must tunnel into charged states on the polymer, one at a time. The energy of the negative integer charge-transfer state (Φ_p) is the energy gained when an electron is added to the polymer. This energy includes the polaronic contribution discussed earlier in this section and lies below the LUMO level of the polymer. Conversely, the energy of the positive integer charge-transfer state (Φ_n) is the energy required to remove an electron from the polymer and must include the polaronic contribution that the transition creates. Charge transfer over the metal/organic interface can occur when the metal work function is greater (smaller) than the formation energy of positively (negatively) charged states within the organic layer.

Figure 2-12b shows a metal/organic contact in which Φ_{Metal} lies above the LUMO of the organic material. As the materials come in to contact, electrons will flow from the metal to the organic LUMO. The metal becomes increasingly positively charged and the polymers at the interface become increasingly negatively charged due to electron transfer. This creates a dipole at the interface and the vacuum level is shifted downwards. This process continues until Φ_{Metal} aligns with Φ_p and equilibrium is reached. Φ_p is now equal to the sum of the potential energy at the interface (Δ) and Φ_{Metal} . The inverse of this process is shown in Figure 2-12c, wherein electrons flow from the organic HOMO to the metal upon contact. Φ_{Metal} at equilibrium is now equal to the sum of Δ and Φ_n . As long as the work function of the cathode (anode) is shallower (deeper) than the LUMO (HOMO) of the organic layer, charge transfer can occur upon contact. If Φ_{Metal} lies between Φ_p and Φ_n however, then electrons will not flow in either direction and the interface will remain vacuum aligned.

2.7 Device Characterisation

The principle metrics for device characteristics are achieved by analysing a current-voltage (J-V) curve. This is obtained by illuminating the device under simulated solar radiation while applying a voltage sweep. Exciton generation, diffusion, disassociation and extraction will occur within a working device. The power conversion efficiency (PCE) of the device is an indication of the success of these processes.

Figure 2-13 shows a typical J-V curve obtained from an organic photovoltaic device under illumination. Current density is a preferential metric to current as it takes in to account the area being illuminated and thus allows for comparison between devices of different architectures and size.

An effective solar cell should be able to generate a high current even when a large bias is applied, therefore increasing its output power output given by

$$P = IV \quad \text{Equation 2.14}$$

The open circuit voltage (V_{oc}) is the applied voltage at which the generated current is zero ($J = 0 \text{ mAcm}^{-2}$). V_{oc} is determined by the difference between work functions of the anode materials and difference between the HOMO of the donor and the LUMO of the acceptor [17][18]. The larger the energy gap, the greater the applied bias that can be applied before current generation is prevented. The acceptor LUMO must therefore be deep enough compared to the donor LUMO so as to overcome the binding energy discussed in 2.6.3, but not so deep as to reduce the open circuit voltage of the cell[19][20]. For an organic polymer to be an effective solar cell material, it must also absorb photons of a suitable wavelength within the solar spectrum. This requires energy gap engineering in order to tune the absorption of the polymer system. Structures can also be added to the polymer in order to engineer its electronic and physical properties. HOMO and LUMO energies

can be tuned by addition of electron-rich ‘donor’ units such as thiophene and electron-poor ‘acceptor’ units such as benzothiadiazole [21].

The short circuit current (J_{sc}) is the measured current when there is no applied bias ($V=0$ V), i.e. the current generated using the in-built electric field of the cell. The narrower a polymer band gap, the more light can be absorbed and the more charges generated. A smaller band gap also lowers the V_{oc} however; therefore an efficient solar cell will strike a balance between these two factors.

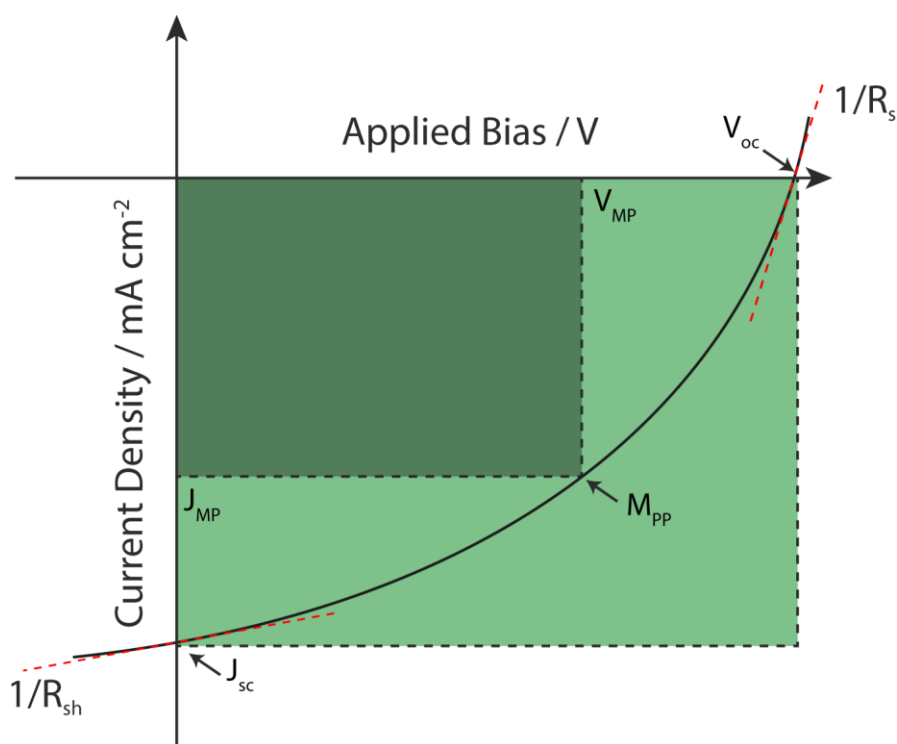


Figure 2-13: An example of a current-voltage curve, showing key values and features used in characterising a photovoltaic device. J_{sc} is the short circuit current density, V_{oc} is the open circuit voltage, J_{MP} and V_{MP} are current density and voltage respectively at the maximum power point M_{pp} . R_s is series resistance and R_{sh} is shunt resistance. The dotted red lines indicate the gradient of the slope at the two axes.

The current-voltage relationship in a simple solar cell can be expressed via the diode equation

$$J = J_{rev} \left[\exp \left(\frac{eV}{kT} \right) - 1 \right] \quad \text{Equation 2.15}$$

where J_{rev} is the reverse saturation (dark) current, e is the electron charge, k is the Boltzmann's constant and T is the absolute temperature [22]. In real device operation, there are losses via resistances in the cell. Series resistance (R_s) depends upon bulk transport, interface charge transfer and contact charge transport. It can be calculated from the inverse of the gradient at open circuit voltage (typical values are 1-10 $\Omega \text{ cm}^2$) [23]. Shunt resistance (R_{sh}) depends upon leakage and shorts through the device and can be calculated from the inverse of the gradient at short circuit current density. Shunt resistance is typically between 1000 - 10000 $\Omega \text{ cm}^2$, with some high-performing cells reaching 0.1 $\text{M}\Omega \text{ cm}^2$ [24][25]. An ideal solar cell will have a large shunt resistance, low series resistance and diode characteristics capable of withstanding high voltages. Total current density for a real solar cell is composed of three contributions: the diode current, the shunt current and the short circuit current density. Taking these factors into account, Equation 2.15 becomes

$$J = J_{rev} \left[\exp \left[\frac{e(V - JR_s)}{kT} \right] - 1 \right] + \frac{V - JR_s}{R_{sh}} - J_{sc} \quad \text{Equation 2.16}$$

Figure 2-14 shows a circuit representation of the solar cell described by Equation 2.16. A large shunt resistance prevents current leakage across the device and a low series resistance reduces the current losses within the device.

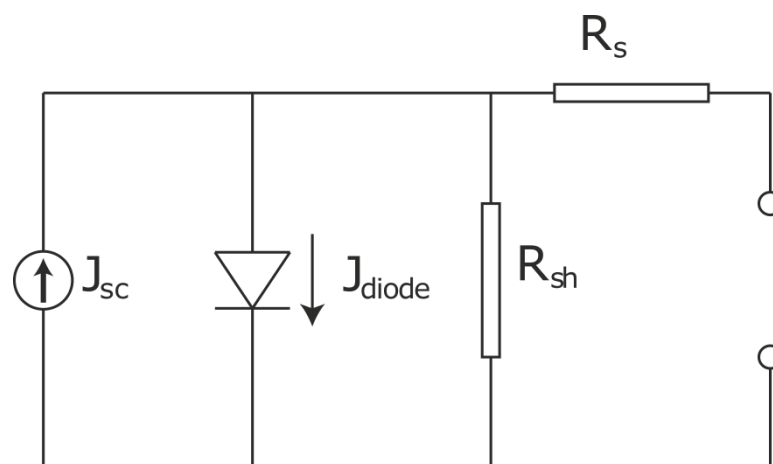


Figure 2-14: An equivalent circuit for a solar cell. J_{sc} is short circuit current density, R_s is series resistance, R_{sh} is shunt resistance and J_{diode} is the diode current.

The maximum power point (M_{pp}) is the location on the J-V curve at which the most power is being generated. The fill factor (FF) is a measure of the ability to extract photocurrent as the voltage is increased. It is given by the ratio of the maximum possible power generation (smaller box in Figure 2-13) to the power that would have been generated if there was no reduction in current with increased voltage (larger box).

$$FF = \frac{J_{MP}V_{MP}}{J_{sc}V_{oc}} \quad \text{Equation 2.17}$$

The fill factor is affected by both series and shunt resistance in the cell, as a can be seen in Figure 2-13. The power conversion efficiency (PCE) is the ratio of input power to output power and can be calculated as:

$$PCE = \frac{P_{out}}{P_{in}} = \frac{J_{MP}V_{MP}}{P_{in}} = \frac{J_{sc}V_{oc}FF}{P_{in}} \quad \text{Equation 2.18}$$

An efficient device will therefore have a deep J_{sc} , a high V_{oc} and a square shaped curve giving a high FF.

2.8 Device Architecture

2.8.1 Early Devices

The initial organic solar cells were made using a single junction between two electrodes of differing work function. This produced an electric field within the device to direct charge extraction. In 1973 Ghosh et al. used a tetracene active layer with aluminium and gold for the electrodes [26]. The efficiencies of these devices were very low however, only achieving <1% PCE.

As the exciton lifetimes in organic polymers are so low, the charges need to arrive at an interface suitable for separation within a short period of time. This requires a short travel distance (~10nm in polymer films). An active layer of 10nm is not thick

enough to absorb the amount of light required for efficient photocurrent generation. There is also no internal force present to separate the bound excitons before they reach an electrode.

2.8.2 Donor and Acceptor Bilayers

To work around this problem and aid dissociation in organic materials, a donor and acceptor system was introduced. An electron rich donor material is combined with an effective electron transport acceptor material at a lower energy level to aid charge extraction. The majority of the electrons are generated in the donor polymer and travel to an interface with the acceptor material. The high electron mobility of this acceptor material allows for a thicker active layer and thus increased light absorption. The bilayer also aided photocurrent generation by separating the bound excitons before they reached an interface.

In 1986, Tang et al. made a donor acceptor photovoltaic system based using bilayers of thermally evaporated copper phthalocyanine (CuPc) and a perylenetetracarboxylic derivative (PV) [27]. There was a large increase in efficiency from the single junction system, with devices achieving ~1% PCE. Even with this step up in efficiency, the films maintained a relatively small charge transfer interface, as they were deposited sequentially creating two vertically separate domains. As with the original single junction devices, only excitons generated near an interface could be dissociated.

Tang's devices also used indium tin oxide as a transparent electrode due to its excellent conduction at high transmittance. This layer is still the most commonly used within organic photovoltaic research. Replacements are being sought however due to its inflexibility and the scarcity of indium [28].

2.8.3 Bulk Heterojunction

In 1995, Gao et al. blended the semiconducting donor polymer MEH-PPV with a fullerene acceptor to create a bicontinuous network donor and acceptor

heterojunctions. This resulted in a large increase in external quantum efficiency and device efficiencies of 2.9% [29]. The preferred morphology of a donor acceptor system provides short distances from an area of exciton generation to an interface at which it can dissociate, while maintaining a film thick enough for maximum light absorption. A large interfacial area between the donor and acceptor increases the number of excitons dissociated, as more of them reach an interface after absorption. A bicontinuous interpenetrating network of donor and acceptor material throughout the film therefore greatly improves photocurrent extraction.

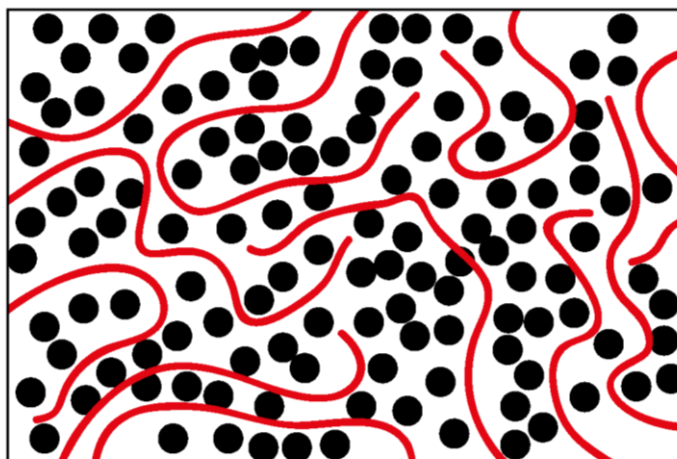


Figure 2-15: A schematic representation of polymer chains surrounded by PCBM domains.

2.8.4 Fullerenes

To achieve a bicontinuous network, the acceptor material needs to be mixed within the donor polymer solution. The most common acceptor materials are derivatives of fullerene. The original fullerene, C_{60} , was synthesised by Kroto et al. in [30]. It has a spherical geometry comprised of 60 carbon atoms connected via sp^2 hybridised orbitals. Photoinduced electron transfer from a conducting polymer to C_{60} was found to occur efficiently, on a timescale of ~ 45 fs [31]. $PC_{60}BM$ is a fullerene that has been functionalised with a solubilising side chain which allows it to dissolve at higher concentrations [32]. A more recently developed fullerene derivative is

PC₇₀BM, which has greater absorption of light in the visible region compared to PC₆₀BM [33].

2.9 Donor Polymers

2.9.1 PCDTBT

For several years, regioregular poly(3-hexylthiophene) (P3HT) was the most popular donor material within the field of organic photovoltaic's due to its simple synthesis and high power conversion efficiencies relative to its time [34]. P3HT has a relatively large band gap of ~1.9eV [35]. This prevents it from harvesting light of longer wavelengths of the solar spectrum, reducing its overall PCE. Carbazole copolymers were developed as alternative donor materials, having deep HOMO levels to protect against oxidation and tunable band gaps due to the presence of electron donating and accepting units within the polymer chain [36]. One such carbazole polymer is poly[[9-(1-octylnonyl)-9H-carbazole-2,7-diyl]-2,5-thiophenediyl-2,1,3-benzothiadiazole-4,7-diyl-2,5-thiophenediyl] (PCDTBT). PCDTBT has a low band gap of 1.2 eV, meaning that it can absorb a large part of the solar spectrum compared with larger band gap polymers such as P3HT. After optimisation of solvent blends and combining PCDTBT with PC⁷⁰BM, an external quantum efficiency of nearly 100% was achieved by Heeger [37]. The maximum performance was further increased by controlling the morphology of the blend by way of a DMSO additive, with efficiencies of over 7% reported [38].

2.10 Interlayers

While the bulk heterojunction aids in dissociation of excitons and the transport of free charges to the electrodes, they must still be extracted at the organic-metal interface. Interlayers aid this process by providing energy levels more closely matched to the HOMOs and LUMOs of the donor and acceptor materials respectively.

2.10.1 PEDOT:PSS

One of the interlayers used in this thesis is poly(3,4-ethylenedioxythiophene):poly(styrenesulfonate)(PEDOT:PSS), a combination of PEDOT and PSS as shown in Figure 2-16. PEDOT:PSS is a widely used hole transport layer in the organic photovoltaic field due to its high hole mobility and its aqueous solubility [28].

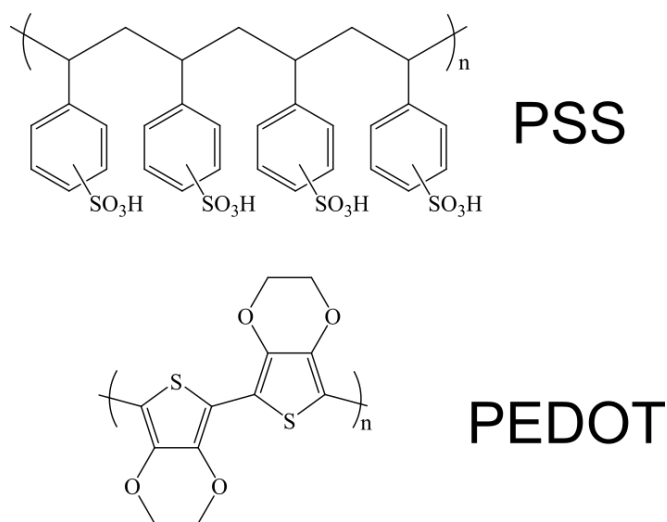


Figure 2-16: The polymers PEDOT and PSS. Together they make the interlayer material PEDOT:PSS.

PEDOT is a conjugated polymer that has a positive charge in its oxidised state. PSS is a polymer with a deprotonated sulfonyl group and has a negative charge. Its high stability and high conductivity at high transparency make it an excellent interlayer. Unfortunately it is insoluble in common solvents [39]. PSS acts to balance the PEDOT charge and increases its aqueous solubility.

2.10.2 Vanadium Oxide

Elements with partially filled d orbitals are called transition metals. As the d orbital can contain up to ten electrons, there are nine transition metals for every shell. Transition metal oxides are formed when the 2p orbitals of oxygen atoms are completely filled by the d orbital electrons of the transition metal atoms. In the case of Vanadium pentoxide (V₂O₅), the now-empty 3d orbitals act as a conduction band

(LUMO) and the filled O 2p orbitals act as a valence band (HOMO). Vanadium oxide has been chosen as a hole transport interlayer in some organic photovoltaic devices [40][41] due to its high work function (~5.5eV).

2.11 Large Scale Deposition Methods

This section will explore the current state of the field in terms of scaling up organic photovoltaic's. There are several important factors when judging the 'best' fabricated devices including device size, cell stability and lifetime, power conversion efficiency, pixel yield and performance variation. Much of the literature has focused on 'hero' devices, wherein OPV performance is increased in laboratory conditions, typically on device sizes of 1-10 mm² in area. While these increases in material performance are very important for the field to progress, the route from laboratory to large scale production must be taken into account. If a very efficient material degrades rapidly when inside a solar panel, it will not be suitable for use in large scale manufacture despite its high initial performance.

2.12 Roll To Roll Deposition Techniques

There are many techniques suitable for the scaling up of organic photovoltaic's from a laboratory technology to mass production. For a deposition method to be effective on a large scale, it must be a rapid process and maintain accurate reproducibility. Some of the scalable processes most commonly used to deposit OPV materials are discussed in this section.

Flexible substrates are desirable for rapid manufacturing as sheets can be passed through printing equipment without the need for the large longitudinal footprint that rigid substrates would require.

2.12.1 Ultrasonic Spray Coating

Spray coating is a technology designed to quickly coat large areas with high uniformity. The spray coating setup employed for the majority of depositions in this

work is shown in Figure 2-17. The solution of interest is fed through a tube at a controlled pressure onto a tip which vibrates at an ultrasonic frequency. This causes it to break up into uniformly sized droplets. After atomisation, droplets are allowed to fall under their own gravity. A nitrogen flow widens and planarises the spray into a uniform mist, allowing even coating of a substrate below the spray head. A Prism 300 spray coater was used in this work which has a tip frequency of $\sim 35\text{KHz}$.

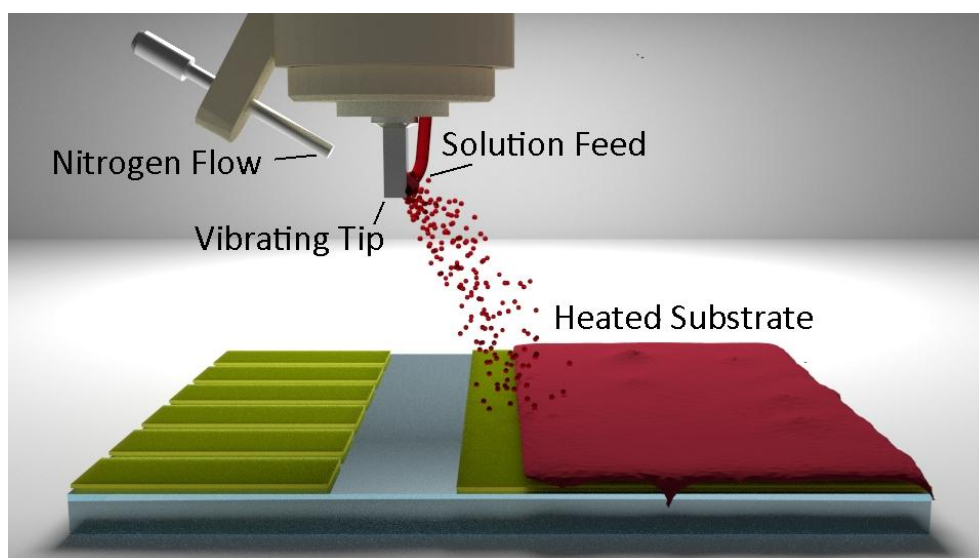


Figure 2-17: Schematic of the ultrasonic spray coater.

Traditional aerosol spray coating uses a nozzle, and solution flow rate is controlled by increasing pressure. Droplet size, flow rate and droplet kinetic energy are all altered with an increase in pressure when solution passes through a nozzle. As ultrasonic spray coating breaks up the solution using a tip, the droplet size and kinetic energy can be kept constant regardless of flow rate. Droplet speed can be reduced to gravitational acceleration and a high flow rate can be achieved without high droplet kinetic energy and a potentially disruptive jet of carrier gas. The spray head is mounted on a computerised gantry which allows for a high precision and reproducibility. Substrates are also placed on a hotplate which allows for control over drying time. There is a large parameter space when producing a film using the ultrasonic spray coater. Solvent choice must take into account solubility of material, boiling point, surface tension, viscosity and vapour pressure. In an ideal case, a

uniform wet film is formed via merging of droplets before evenly drying. Film thickness can be controlled via spray height, lateral spray speed, solution flow rate and solution concentration. For example, a similar thickness can be obtained using a low concentration and a high flow rate or a high concentration and low flow rate. Drying time will be changed as a result, and the final films will have different morphologies. Optimising a spray recipe must take into account the amount of solution deposited in an area, solution flow properties, drying time of that solution and amount of material remaining once the solvent has evaporated. Table Chapter 2-2-2 shows a literature review of spray-cast OPV materials, pixel areas and device performance.

Spray Technique	PCE (%)	Pixel Area (mm ²)	Sprayed HTL	Sprayed Photoactive Layer (PAL)	Citation
Airbrush	2.83	16.4	-	P3HT:PC ₆₁ BM	Vak 2007[42]
Airbrush	2.8	3.4	-	P3HT:PC ₆₁ BM	Giroto 2009[43]
Airbrush	2.7	20	PEDOT:PSS	P3HT:PC ₆₁ BM	Hoth 2009[44]
Ultrasonic	3.5	-	PEDOT:PSS	P3HT:PC ₆₁ BM	Steirer 2009[45]
Airbrush	2.17	4.66	PEDOT:PSS	P3HT:PC ₆₁ BM	Na 2010[46]
Airbrush	3.4	4.75	-	P3HT:PC ₆₁ BM	Yu 2010[47]
Ultrasonic	3.75	3	PEDOT:PSS	P3HT:PC ₆₁ BM	Giroto 2011[48]
Airbrush	5.8	15	-	P1: PC ₆₁ BM*	Nie 2012[49]
Ultrasonic	4.3	4.5	-	PCDTBT:PC ₇₁ BM	Wang 2013[50]
Airbrush	4.1	-	-	P3HT:PC ₆₁ BM	Tait 2013[51]
Airbrush	4.2	10		P3HT:PC ₆₁ BM	Vak 2015[52]
Ultrasonic	3.7	165	PEDOT:PSS	PCDTBT:PC₇₁BM	This Thesis

Table Chapter 2-2-2: A literature review of spray-cast OPV materials, including pixel areas and device performance.

Much progress has been made using spray coating as a deposition technique. There is still a disparity between devices with high efficiencies and those with large device areas however.

2.12.2 Doctor Blading

Doctor blading (or knife coating) is a one dimensional printing technique which has been used to coat photoactive layers such as P3HT [53]. A schematic of a doctor blade can be seen in Figure 2-17. Ink is fed onto a substrate which passes under a sharp blade held at a fixed height above the substrate surface. The height of the blade determines the amount of material that can pass under it and thus the final film thickness. This is a simple technique and therefore does not allow for high control over the film wetting area or uniformity [54].

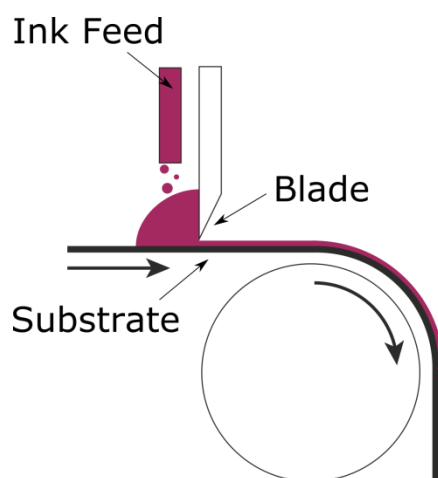


Figure 2-18: A simplified schematic of a doctor blading system.

Both spray coating and doctor blading lack lateral precision during the deposition process, therefore two dimensional patterns are difficult to achieve via the deposition itself. This can be overcome via patterned masks or laser patterning/ablation after film deposition [55].

2.12.3 Slot Die

Slot die coating uses a similar concept to doctor blading, in which the solution is fed from an ink reservoir onto a surface through a slot. Unlike doctor blading however, the width of the wet film can be controlled by the width of the slot. Film thickness can be controlled by solution pressure and substrate speed.

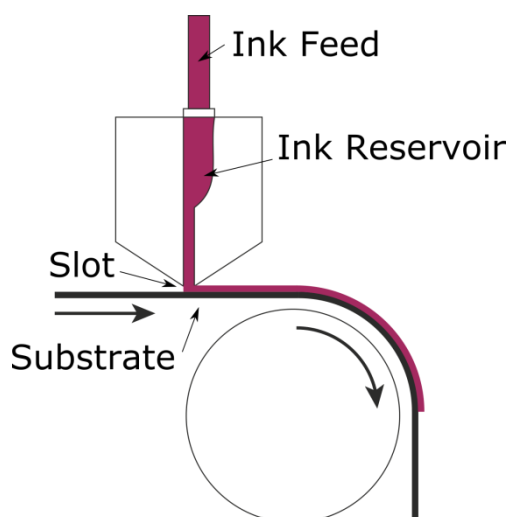


Figure 2-19: A simplified schematic of a slot die coating system.

This offers an advantage over doctor blading and spray coating, as the film can be patterned in to thin strips during deposition due to the slot having a finite width. These strips can then be connected in series to produce multiple, long solar cells on one substrate [56].

2.12.4 Screen Printing

A schematic of screen printing is displayed in Figure 2-20. A screen of woven material is fastened to a frame and put under tension. A squeegee presses down on the taut screen, forcing an ink through holes onto the surface below. The holes in the screen determine where the ink will be, allowing for two dimensional patterning of a surface. This deposition has been used to pattern smooth photoactive layers with thicknesses as low as 40 -60 nm in OPV devices [57][58]. Ink formulations used for screen printing must have a high viscosity to prevent solution flowing to areas outside the designated pattern. Modules of 132 cm² have been fabricated using screen printing on flexible substrates for several layers in a device stack, however device performance was poor [59]. Screen printing can also be used to pattern solution processable electrode materials such as silver paste into current collecting grids [60].

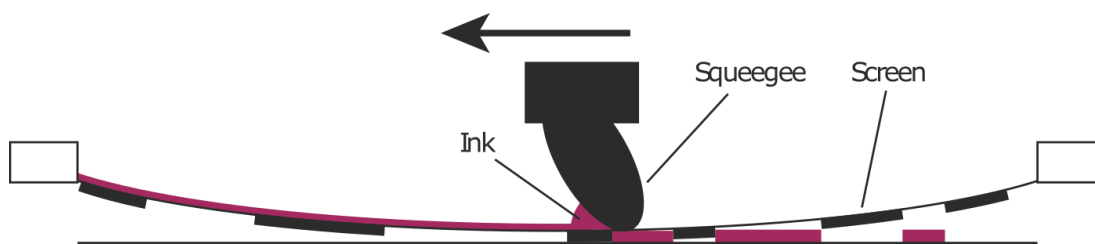


Figure 2-20: A simplified schematic of a screen printing system.

2.12.5 Gravure Printing

Gravure printing has been well established as printing technique capable of depositing organic films. It has been used to coat both PEDOT:PSS hole transport layers [61] and photoactive layers [62] for OPV devices. Figure 2-21 shows a schematic of a gravure printing system. A patterned roller is passed through a bath, where it collects ink on its surface in a thick layer. A doctor blade is used to limit the film thickness to within grooves on the pattern roller surface. These patterns are then transferred to a flexible substrate as it is pressed onto the pattern roller by an impression roller.

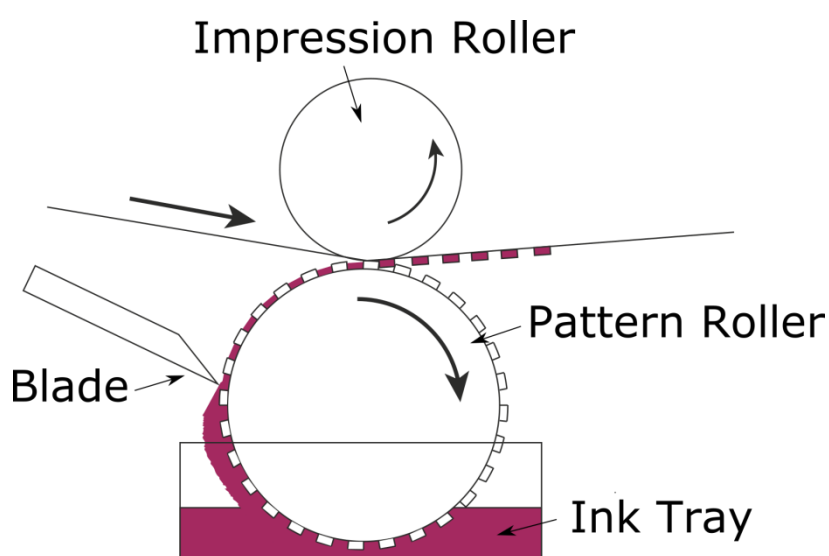


Figure 2-21: A simplified schematic of a gravure printing system.

2.12.6 Spray Coating in This Thesis

While there are multiple coating and printing techniques available for use with organic photovoltaic materials, spray coating offers fast, large-area deposition while maintaining the ability to produce films on both nanometre and micrometre scales. The large parameter space between deposition settings and solution recipes allows for the deposition of many different materials. The more numerous the approaches to the challenges of OPV roll to roll processing, the faster they can be overcome.

As shown in Table Chapter 2-2-2, ultrasonic spray coating of OPVs has so far resulted in high efficiencies or large areas, yet few publications report of both simultaneously. This thesis attempts to bridge the gap between these two metrics and comment on the viability of ultrasonic spray coating for use in the fabrication of OPVs.

2.13 Wetting

In order to achieve uniform, continuous polymer films over a large area, the wetting properties of an ink must be controlled. This can be done in a number of ways, some of which will be discussed in this section.

2.13.1 Contact Angle

When a liquid droplet is deposited on to a solid, it spreads out over its surface as the free energy of the system is minimised. The droplet will stop spreading when an equilibrium is reached between the surface tensions of the solid, liquid and gas interfaces. Figure 2-22 shows a representation of a droplet on the surface of a solid, surrounded by air. The contact angle (Θ_E) is determined by the balance of interfacial tensions at the solid/liquid (γ_{SL}), the solid/air (γ_{SA}) and the liquid/air (γ) boundaries and given by Equation 2.19. It is a quantitative measurement used to indicate how well a given liquid wets when dropped upon a given solid.

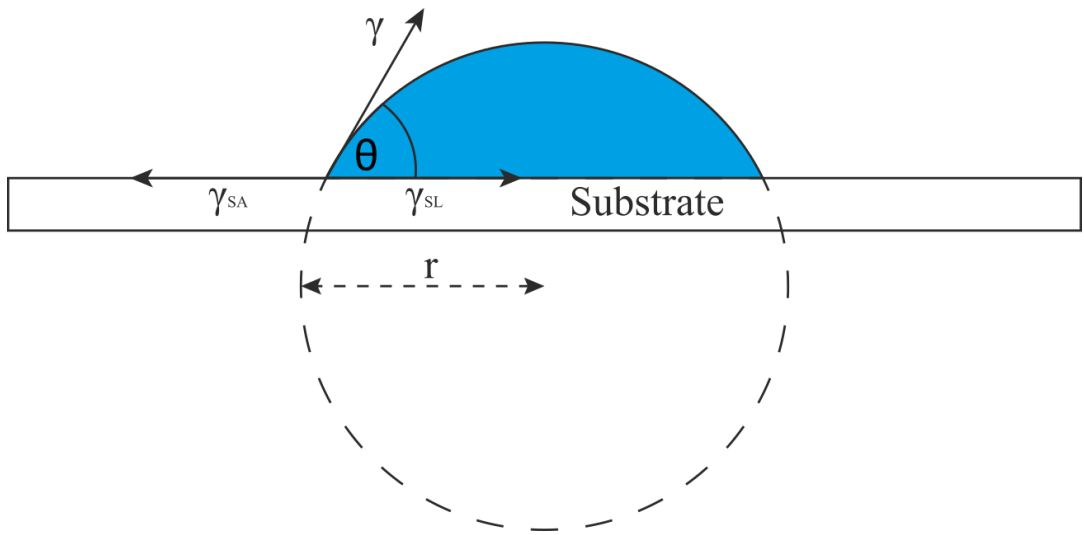


Figure 2-22: A droplet on a substrate, showing interfacial forces and contact angle.

$$\cos(\theta_E) = \frac{(\gamma_{SA} - \gamma_{SL})}{\gamma} \qquad \text{Equation 2.19}$$

2.13.2 Spreading Parameter

Two possible scenarios can occur when a droplet lands on a surface: partial wetting or total wetting. Partial wetting occurs when the droplet forms a blob (Figure 2-23a-b) and total wetting occurs when contact angle is very small and the droplet spreads (Figure 2-23c). When a liquid partially wets the surface, it can either be mostly-wetting, wherein the contact angle is below 90° (Figure 2-23b), or mostly non-wetting if the angle is above 90° (Figure 2-23a).

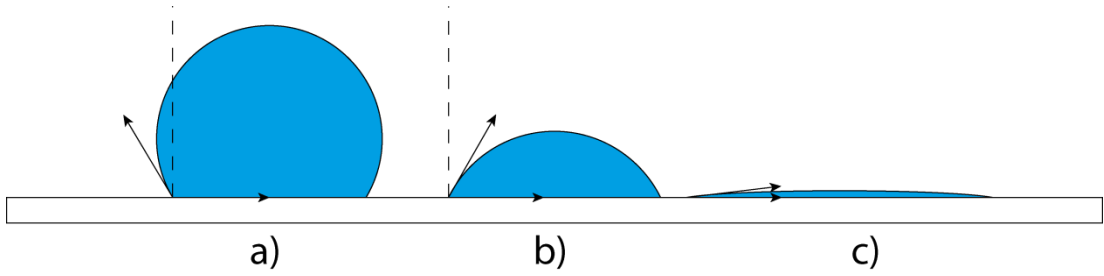


Figure 2-23: Wetting scenarios including a) mostly non-wetting, b) mostly wetting and c) total wetting.

Using Equation 2.19, a spreading parameter can be determined as an indication of how well a droplet will spread over a surface. The parameter S is the difference in

energy between a bare solid surface (γ_{SA}) and a surface covered with a liquid film ($\gamma_{SL} + \gamma$) [63].

$$S = \gamma_{SA} - (\gamma_{SL} + \gamma) \quad \text{Equation 2.20}$$

If $S > 0$ then the energy of the bare solid surface is greater and the droplet covers the surface. If $S < 0$, partial wetting occurs. Inserting Equation 2.19 into Equation 2.20 gives

$$S = \gamma (\cos(\theta_E) - 1) \quad \text{Equation 2.21}$$

If θ_E is $\pi/2$ or greater, the liquid will not wet to the surface.

2.14 References

- [1] W. Heisenberg, "Über den anschaulichen Inhalt der quantentheoretischen Kinematik und Mechanik," *Zeitschrift für Phys.*, vol. 43, no. 3–4, pp. 172–198, Mar. 1927.
- [2] H. D. Young and R. A. Freedman, *University Physics*, 12th ed. Pearson Addison-Wesley, 2008.
- [3] D. Klein, *Organic Chemistry*, 2nd ed. Wiley, 2012.
- [4] P. Atkins and J. de Paula, *Physical Chemistry*, 10th ed. Atkins & de Paula, 2014.
- [5] a O. Patil, a J. Heeger, and F. Wudl, "Optical properties of conducting polymers," *Chem. Rev.*, vol. 88, no. 1, pp. 183–200, 1988.
- [6] C. S. Yannoni and T. C. Clarke, "Molecular geometry of cis- and trans-polyacetylene by nutation NMR spectroscopy," *Phys. Rev. Lett.*, vol. 51, no. 13, pp. 1191–1193, 1983.
- [7] T. M. Clarke and J. R. Durrant, "Charge Photogeneration in Organic Solar Cells," *Chem. Rev.*, vol. 110, no. 11, pp. 6736–6767, Nov. 2010.
- [8] J.-L. Brédas, J. E. Norton, J. Cornil, and V. Coropceanu, "Molecular Understanding of Organic Solar Cells: The Challenges," *Acc. Chem. Res.*, vol. 42, no. 11, pp. 1691–1699, Nov. 2009.
- [9] V. Coropceanu, J. Cornil, D. A. da Silva Filho, Y. Olivier, R. Silbey, and J.-L. Brédas, "Charge Transport in Organic Semiconductors," *Chem. Rev.*, vol. 107, no. 4, pp. 926–952, Apr. 2007.
- [10] S. R. Scully and M. D. McGehee, "Effects of optical interference and energy transfer on exciton diffusion length measurements in organic semiconductors," *J. Appl. Phys.*, vol. 100, no. 3, p. 034907, 2006.
- [11] B. C. Thompson and J. M. J. Fréchet, "Polymer–Fullerene Composite Solar Cells," *Angew. Chemie Int. Ed.*, vol. 47, no. 1, pp. 58–77, Jan. 2008.
- [12] M. C. Scharber, D. Mühlbacher, M. Koppe, P. Denk, C. Waldauf, A. J. Heeger, and C. J. Brabec, "Design rules for donors in bulk-heterojunction solar cells - Towards 10 % energy-conversion efficiency," *Adv. Mater.*, vol. 18, no. 6, pp. 789–794, 2006.

- [13] J.-L. Brédas, D. Beljonne, V. Coropceanu, and J. Cornil, "Charge-Transfer and Energy-Transfer Processes in π -Conjugated Oligomers and Polymers: A Molecular Picture," *Chem. Rev.*, vol. 104, no. 11, pp. 4971–5004, Nov. 2004.
- [14] D. Hertel and H. Bässler, "Photoconduction in Amorphous Organic Solids," *ChemPhysChem*, vol. 9, no. 5, pp. 666–688, Apr. 2008.
- [15] A. Miller and E. Abrahams, "Impurity conduction at low concentrations," *Phys. Rev.*, vol. 120, no. 3, pp. 745–755, 1960.
- [16] S. Braun, W. R. Salaneck, and M. Fahlman, "Energy-Level Alignment at Organic/Metal and Organic/Organic Interfaces," *Adv. Mater.*, vol. 21, no. 14–15, pp. 1450–1472, Apr. 2009.
- [17] D. Rauh, A. Wagenpfahl, C. Deibel, and V. Dyakonov, "Relation of open circuit voltage to charge carrier density in organic bulk heterojunction solar cells," *Appl. Phys. Lett.*, vol. 98, no. 13, 2011.
- [18] V. D. Mihailetschi, P. W. M. Blom, J. C. Hummelen, and M. T. Rispens, "Cathode dependence of the open-circuit voltage of polymer:fullerene bulk heterojunction solar cells," *J. Appl. Phys.*, vol. 94, no. 10, pp. 6849–6854, 2003.
- [19] C. J. Brabec, A. Cravino, D. Meissner, N. Serdar Sariciftci, T. Fromherz, M. T. Rispens, L. Sanchez, and J. C. Hummelen, "Origin of the open circuit voltage of plastic solar cells," *Adv. Functional Mater.*, vol. 11, no. 5, pp. 374–380, 2001.
- [20] A. Gadisa, M. Svensson, M. R. Andersson, and O. Inganäs, "Correlation between oxidation potential and open-circuit voltage of composite solar cells based on blends of polythiophenes/ fullerene derivative," *Appl. Phys. Lett.*, vol. 84, no. 9, p. 1609, 2004.
- [21] Z. Zhang and J. Wang, "Structures and properties of conjugated Donor–Acceptor copolymers for solar cell applications," *Journal of Materials Chemistry*, vol. 22, no. 10, p. 4178, 2012.
- [22] C. J. Brabec, V. Dyakonov, J. Parisi, and N. S. Sariciftci, Eds., *Organic Photovoltaics*. Berlin, Heidelberg: Springer Berlin Heidelberg, 2003.
- [23] B. Qi and J. Wang, "Fill factor in organic solar cells," *Phys. Chem. Chem. Phys. PCCP*, vol. 15, no. 23, pp. 8972–82, 2013.
- [24] M. S. Kim, B. G. Kim, and J. Kim, "Effective variables to control the fill factor of organic photovoltaic cells," *ACS Appl. Mater. Interfaces*, vol. 1, no. 6, pp. 1264–1269, 2009.

- [25] T. Stubhan, T. Ameri, M. Salinas, J. Krantz, F. MacHui, M. Halik, and C. J. Brabec, "High shunt resistance in polymer solar cells comprising a MoO₃ hole extraction layer processed from nanoparticle suspension," *Appl. Phys. Lett.*, vol. 98, no. 25, pp. 98–101, 2011.
- [26] A. K. Ghosh, "Rectification, space-charge-limited current, photovoltaic and photoconductive properties of Al/tetracene/Au sandwich cell," *J. Appl. Phys.*, vol. 44, no. 6, p. 2781, 1973.
- [27] C. W. Tang, "Two-layer organic photovoltaic cell," *Appl. Phys. Lett.*, vol. 48, no. 2, p. 183, 1986.
- [28] D. Angmo and F. C. Krebs, "Flexible ITO-free polymer solar cells," *J. Appl. Polym. Sci.*, vol. 129, no. 1, pp. 1–14, Jul. 2013.
- [29] G. Yu, J. Gao, J. C. Hummelen, F. Wudl, and A. J. Heeger, "Polymer Photovoltaic Cells: Enhanced Efficiencies via a Network of Internal Donor-Acceptor Heterojunctions," *Science*, vol. 270, no. 5243, pp. 1789–1791, 1995.
- [30] H. W. Kroto, J. R. Heath, S. C. O'Brien, R. F. Curl, and R. E. Smalley, "C₆₀: Buckminsterfullerene," *Nature*, vol. 318, no. 6042, pp. 162–163, Nov. 1985.
- [31] C. J. Brabec, G. Zerza, G. Cerullo, S. De Silvestri, S. Luzzati, J. C. Hummelen, and S. Sariciftci, "Tracing photoinduced electron transfer process in conjugated polymer/fullerene bulk heterojunctions in real time," *Chem. Phys. Lett.*, vol. 340, no. 3–4, pp. 232–236, Jun. 2001.
- [32] J. C. Hummelen, B. W. Knight, F. LePeq, F. Wudl, J. Yao, and C. L. Wilkins, "Preparation and Characterization of Fulleroid and Methanofullerene Derivatives," *J. Org. Chem.*, vol. 60, no. 3, pp. 532–538, Feb. 1995.
- [33] M. M. Wienk, J. M. Kroon, W. J. H. Verhees, J. Knol, J. C. Hummelen, P. A. van Hal, and R. A. J. Janssen, "Efficient Methano[70]fullerene/MDMO-PPV Bulk Heterojunction Photovoltaic Cells," *Angew. Chemie Int. Ed.*, vol. 42, no. 29, pp. 3371–3375, Jul. 2003.
- [34] G. Li, V. Shrotriya, J. Huang, Y. Yao, T. Moriarty, K. Emery, and Y. Yang, "High-efficiency solution processable polymer photovoltaic cells by self-organization of polymer blends," *Nat. Mater.*, vol. 4, no. 11, pp. 864–868, Nov. 2005.
- [35] B. Kim, H. R. Yeom, M. H. Yun, J. Y. Kim, and C. Yang, "A Selenophene Analogue of PCDTBT: Selective Fine-Tuning of LUMO to Lower of the Bandgap for Efficient Polymer Solar Cells," *Macromolecules*, vol. 45, no. 21, pp. 8658–8664, Nov. 2012.

- [36] N. Blouin, A. Michaud, and M. Leclerc, "A Low-Bandgap Poly(2,7-Carbazole) Derivative for Use in High-Performance Solar Cells," *Adv. Mater.*, vol. 19, no. 17, pp. 2295–2300, Sep. 2007.
- [37] S. H. Park, A. Roy, S. Beaupré, S. Cho, N. Coates, J. S. Moon, D. Moses, M. Leclerc, K. Lee, and A. J. Heeger, "Bulk heterojunction solar cells with internal quantum efficiency approaching 100%," *Nat. Photonics*, vol. 3, no. 5, pp. 297–302, 2009.
- [38] T.-Y. Chu, S. Alem, S.-W. Tsang, S.-C. Tse, S. Wakim, J. Lu, G. Dennler, D. Waller, R. Gaudiana, and Y. Tao, "Morphology control in polycarbazole based bulk heterojunction solar cells and its impact on device performance," *Appl. Phys. Lett.*, vol. 98, no. 25, p. 253301, 2011.
- [39] P. A. Levermore, L. Chen, X. Wang, R. Das, and D. D. C. Bradley, "Fabrication of Highly Conductive Poly(3,4-ethylenedioxythiophene) Films by Vapor Phase Polymerization and Their Application in Efficient Organic Light-Emitting Diodes," *Adv. Mater.*, vol. 19, no. 17, pp. 2379–2385, Sep. 2007.
- [40] Y.-M. Chang and J.-M. Ding, "High efficiency inverted polymer solar cells with the sol-gel derived vanadium oxide interlayer," *Thin Solid Films*, vol. 520, no. 16, pp. 5400–5404, Jun. 2012.
- [41] G. Terán-Escobar, J. Pampel, J. M. Caicedo, and M. Lira-Cantú, "Low-temperature, solution-processed, layered V2O5 hydrate as the hole-transport layer for stable organic solar cells," *Energy Environ. Sci.*, vol. 6, no. 10, p. 3088, Sep. 2013.
- [42] D. J. Vak, D. J. Vak, S. S. Kim, S. S. Kim, J. Jo, J. Jo, S. H. Oh, S. H. Oh, S. I. Na, S. I. Na, J. W. Kim, J. W. Kim, D. Y. Kim, and D. Y. Kim, "Fabrication of organic bulk heterojunction solar cells by a spray deposition method for low-cost power generation," *Appl. Phys. Lett.*, vol. 91, no. 8, p. -, 2007.
- [43] C. Girotto, B. P. Rand, J. Genoe, and P. Heremans, "Exploring spray coating as a deposition technique for the fabrication of solution-processed solar cells," *Sol. Energy Mater. Sol. Cells*, vol. 93, no. 4, pp. 454–458, Apr. 2009.
- [44] C. N. Hoth, R. Steim, P. Schilinsky, S. a. Choulis, S. F. Tedde, O. Hayden, and C. J. Brabec, "Topographical and morphological aspects of spray coated organic photovoltaics," *Org. Electron. physics, Mater. Appl.*, vol. 10, no. 4, pp. 587–593, Jul. 2009.
- [45] K. X. Steirer, J. J. Berry, M. O. Reese, M. F. a. M. van Hest, A. Miedaner, M. W. Liberatore, R. T. Collins, and D. S. Ginley, "Ultrasonically sprayed and inkjet printed thin film electrodes for organic solar cells," *Thin Solid Films*, vol. 517, no. 8, pp. 2781–2786, Feb. 2009.

- [46] S.-I. Na, B.-K. Yu, S.-S. Kim, D. Vak, T.-S. Kim, J.-S. Yeo, and D.-Y. Kim, "Fully spray-coated ITO-free organic solar cells for low-cost power generation," *Sol. Energy Mater. Sol. Cells*, vol. 94, no. 8, pp. 1333–1337, Aug. 2010.
- [47] B. K. Yu, D. Vak, J. Jo, S. I. Na, S. S. Kim, M. K. Kim, and D. Y. Kim, "Factors to be considered in bulk heterojunction polymer solar cells fabricated by the spray process," *IEEE J. Sel. Top. Quantum Electron.*, vol. 16, no. 6, pp. 1838–1846, 2010.
- [48] C. Girotto, D. Moia, B. P. Rand, and P. Heremans, "High-Performance Organic Solar Cells with Spray-Coated Hole-Transport and Active Layers," *Adv. Funct. Mater.*, vol. 21, no. 1, pp. 64–72, Jan. 2011.
- [49] W. Nie, R. C. Coffin, J. Liu, Y. Li, E. D. Peterson, C. M. MacNeill, R. E. Nofhle, and D. L. Carroll, "High efficiency organic solar cells with spray coated active layers comprised of a low band gap conjugated polymer," *Appl. Phys. Lett.*, vol. 100, no. 8, p. 083301, 2012.
- [50] T. Wang, N. W. Scarratt, H. Yi, A. D. F. Dunbar, A. J. Pearson, D. C. Watters, T. S. Glen, A. C. Brook, J. Kingsley, A. R. Buckley, M. W. a Skoda, A. M. Donald, R. a L. Jones, A. Iraqi, and D. G. Lidzey, "Fabricating high performance, donor-acceptor copolymer solar cells by spray-coating in air," *Adv. Energy Mater.*, vol. 3, no. 4, pp. 505–512, Apr. 2013.
- [51] J. G. Tait, B. P. Rand, and P. Heremans, "Concurrently pumped ultrasonic spray coating for donor:acceptor and thickness optimization of organic solar cells," *Org. Electron.*, vol. 14, no. 3, pp. 1002–1008, Mar. 2013.
- [52] D. Vak, J. van Embden, W. W. H. Wong, and S. Watkins, "Optically monitored spray coating system for the controlled deposition of the photoactive layer in organic solar cells," *Appl. Phys. Lett.*, vol. 106, no. 3, p. 033302, Jan. 2015.
- [53] P. Schilinsky, C. Waldauf, and C. J. Brabec, "Performance Analysis of Printed Bulk Heterojunction Solar Cells," *Adv. Funct. Mater.*, vol. 16, no. 13, pp. 1669–1672, Sep. 2006.
- [54] R. Søndergaard, M. Hösel, D. Angmo, T. T. Larsen-Olsen, and F. C. Krebs, "Roll-to-roll fabrication of polymer solar cells," *Mater. Today*, vol. 15, no. 1–2, pp. 36–49, Jan. 2012.
- [55] G. Dennler, C. Lungenschmied, H. Neugebauer, N. S. Sariciftci, and a. Labouret, "Flexible, conjugated polymer-fullerene-based bulk-heterojunction solar cells: Basics, encapsulation, and integration," *J. Mater. Res.*, vol. 20, no. 12, pp. 3224–3233, 2005.

- [56] F. C. Krebs, J. Fyenbo, and M. Jørgensen, "Product integration of compact roll-to-roll processed polymer solar cell modules: methods and manufacture using flexographic printing, slot-die coating and rotary screen printing," *J. Mater. Chem.*, vol. 20, no. 41, p. 8994, 2010.
- [57] S. E. Shaheen, R. Radspinner, N. Peyghambarian, and G. E. Jabbour, "Fabrication of bulk heterojunction plastic solar cells by screen printing," *Appl. Phys. Lett.*, vol. 79, no. 18, p. 2996, 2001.
- [58] B. Zhang and H. Chae, "Screen-Printed Polymer:Fullerene Bulk-Heterojunction Solar Cells," *Jpn. J. Appl. Phys.*, vol. 48, p. 20208, 2009.
- [59] F. C. Krebs, M. Jørgensen, K. Norrman, O. Hagemann, J. Alstrup, T. D. Nielsen, J. Fyenbo, K. Larsen, and J. Kristensen, "A complete process for production of flexible large area polymer solar cells entirely using screen printing—First public demonstration," *Sol. Energy Mater. Sol. Cells*, vol. 93, no. 4, pp. 422–441, Apr. 2009.
- [60] Y. Galagan, J.-E. J.M. Rubingh, R. Andriessen, C.-C. Fan, P. W.M. Blom, S. C. Veenstra, and J. M. Kroon, "ITO-free flexible organic solar cells with printed current collecting grids," *Sol. Energy Mater. Sol. Cells*, vol. 95, no. 5, pp. 1339–1343, May 2011.
- [61] C.-K. Cho, W.-J. Hwang, K. Eun, S.-H. Choa, S.-I. Na, and H.-K. Kim, "Mechanical flexibility of transparent PEDOT:PSS electrodes prepared by gravure printing for flexible organic solar cells," *Sol. Energy Mater. Sol. Cells*, vol. 95, no. 12, pp. 3269–3275, Dec. 2011.
- [62] P. Kopola, T. Aernouts, R. Sliz, S. Guillerez, M. Ylikunnari, D. Cheyns, M. Välimäki, M. Tuomikoski, J. Hast, G. Jabbour, R. Myllylä, and A. Maaninen, "Gravure printed flexible organic photovoltaic modules," *Sol. Energy Mater. Sol. Cells*, vol. 95, no. 5, pp. 1344–1347, May 2011.
- [63] M. Daoud and C. E. Williams, Eds., *Soft Matter Physics*. Berlin, Heidelberg: Springer Berlin Heidelberg, 1999.

Chapter 3 Device Fabrication and Characterisation

3.1 Spin Coating

Spin coating is the most common deposition technique for solution processed organic photovoltaic devices [1]. It allows reproducible smooth films to be created with fine control over thickness. Substrates are placed in a recessed chuck or held in place using a vacuum. The chuck is then spun at a chosen rotational velocity and solution is deposited on to the spinning substrate via a micropipette. The solution is spread over the substrate by the centrifugal force of the spinning substrate. Solution drying time is dependent on the solvent boiling point and spin speed which both influence the resultant film thickness. A fast drying solvent will result in a thicker film, as less solvent has a chance to leave the substrate before it can evaporate and deposit its solute. With a higher boiling point solvent, more solvent leaves the substrate before evaporating, therefore films are thinner. The relationship between final film thickness τ is given by:

$$\tau \propto \frac{cv}{\sqrt{\omega}} \quad \text{Equation 3.1}$$

where c is the solution concentration, v is the solution viscosity and ω is the spin speed [2]. When the same solution is used, c and v are constant and thicknesses at differing spin speed can be calculated after a single thickness measurement using:

$$\tau_2 = \frac{\tau_1 \sqrt{\omega_1}}{\sqrt{\omega_2}} \quad \text{Equation 3.2}$$

where τ_1 is the measured thickness given by spin speed ω_1 . The evaporation speed also effects film uniformity. The concentration of the film changes during solvent evaporation and thus effects viscosity. The longer the film takes to dry, the less rapidly viscosity changes and the more uniform it will be. The downside of a long drying film is that more solvent is wasted by leaving the substrate. A trade-off is therefore required between a less wasteful fast drying film, and a more wasteful yet

more uniform film. Regardless of spin speed, much of the solution used in spin coating is lost during the process. Spin coating over a large area is also problematic, as the thickness of the film changes as the solution moves further from its centre.

3.2 Solution Preparation

Glass vials were blown with a dry nitrogen gun to remove any large dust particles. The vials were then partially filled with isopropyl alcohol, shaken and dried using the gun. Materials were weighed out on scales and then transferred to a nitrogen glove box. Solvent was added at the desired concentration and the solutions were left to dissolve on a hotplate. For the PCDTBT:PCBM donor:acceptor system, the PCDTBT was dissolved first and then added to the PCBM powder to obtain a weight ratio of 1:4. For spin-coating solutions, a total concentration of $25\text{mg}\cdot\text{ml}^{-1}$ was used and $8\text{mg}\cdot\text{ml}^{-1}$ was typically used for spray-coating solutions. For PEDOT:PSS preparation, stock solution was filtered through a $0.45\mu\text{m}$ polyvinylidene difluoride PVDF filter into a pre-cleaned glass vial. For spray-coating solution, this was then combined with IPA and Ethyl Glycol at a solution ratio of 1:8:1.

3.3 Spin Coating and Spray Coating Comparison

During spray coating, the solution is deposited on top of a substrate and no external force acts to remove it. This means that apart from solvent flowing over edges, the solution that lands on a substrate will stay there until the solvent has evaporated. The polymer within that solution will remain and thus determines the thickness of the dry film. In the case of spin coating, some of the solution is forced off the edge of the substrate before the film has dried, due to centrifugal force. This means that not all of the deposited polymer will remain after the film has dried. Solution concentration must therefore be increased when spin coating compared to spray coating, in order to achieve similar final film thicknesses. The differences in solution flow and drying kinetics may lead to differences in film morphology of the final film, as shear forces acting on the spin cast film are not present in the thermally

evaporated spray cast film. This difference in drying must be taken into account when making comparisons between solar cells fabricated using the two techniques.

3.4 Vacuum Evaporation

A calcium/aluminium cathode is used in all the devices described in this thesis. This is produced via thermal evaporation inside a vacuum chamber containing several sources to allow for successive materials to be evaporated without opening the chamber to atmosphere. The evaporation chamber is located inside a nitrogen glovebox that allows subsequent encapsulation without exposing the evaporated layers to air. Substrates are secured in a patterned stainless steel shadow mask and loaded in to the chamber. The chamber is pumped down to a pressure of 10^{-7} mbar to remove any gases that could interfere with the path of the evaporated materials. A material is heated inside a resistive tungsten coil until it begins to evaporate. A shutter prevents the material reaching the substrates until a desired evaporation rate is achieved. Deposition rate and therefore thickness is obtained by a quartz crystal inside the chamber which is calibrated depending on source position.

3.5 Device Fabrication

There were several stages in fabrication process. They are detailed below and shown schematically in Figure 3-1.

3.5.1 Substrate Preparation

ITO substrates were cleaned via sonication for five minutes successively in sodium hydroxide, Hellmanex, hot deionised water and IPA with a dunk rinse in hot DI water between the sodium hydroxide and Hellmanex stages. The substrates were then dried using a nitrogen jet and placed on a hot plate for 10 minutes.

3.5.2 PEDOT:PSS

PEDOT:PSS layers were deposited via spin coating or spray coating. Substrate edges were required for electrical contacts and were therefore wiped clean using a cotton

bud dipped in DI water, as illustrated in Figure 3-1b. Substrates were then placed on a hotplate at 120°C to bake off any excess water. For spin coating, a spin speed of 5000rpm was used to achieve a film of ~30nm in thickness. The PEDOT:PSS spray coating deposition is described in detail in Chapter 6. After deposition, substrates were wiped at the edges and annealed for a further 10 minutes.

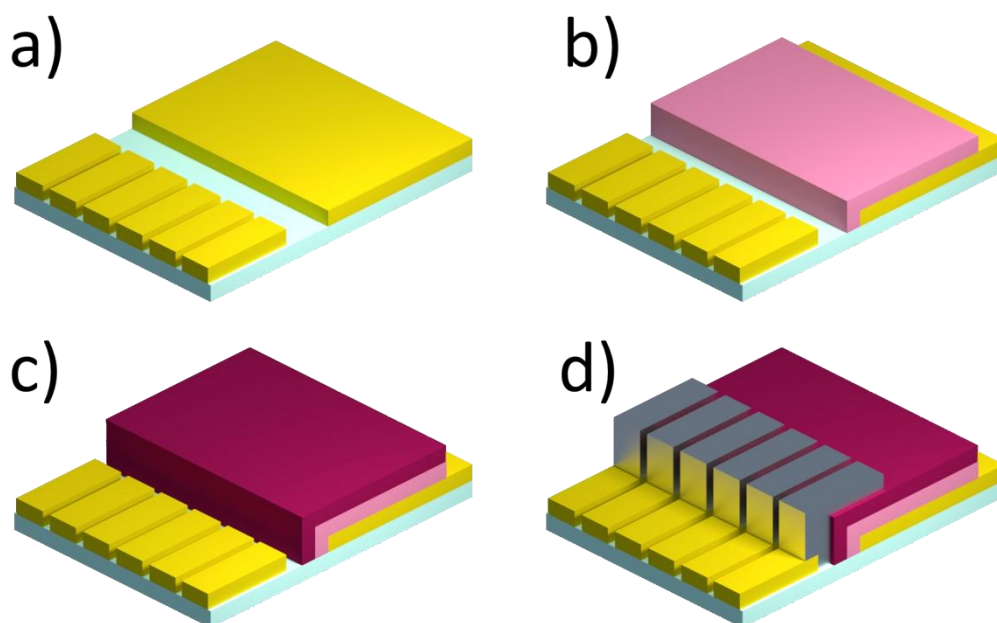


Figure 3-1: Deposition stages in the fabrication of an OPV device. A pre-patterned ITO substrate (a) is first coated (spin or spray) with a hole transport layer (b), then a photoactive layer (c) and finally a Ca/Al cathode is evaporated on top (d).

3.5.3 Photoactive Layer

The donor:acceptor photoactive layers were spin or spray coated from solution. As with the hole transport layers, substrates were cleaned at the edges using whichever solvent they were spin cast from to clean the electrical contact of the device as shown in Figure 3-1ac. Detailed deposition parameters are given in the experimental chapters of this thesis.

3.5.4 Cathode Layer

After the photoactive layer deposition, substrates were transferred to a vacuum evaporation chamber within a Nitrogen glovebox. Calcium was deposited at a rate between 0.1 and $0.4\text{\AA}\cdot\text{s}^{-1}$ to create a 5nm thick film and Aluminium at a rate of $1.5\text{\AA}\cdot\text{s}^{-1}$ to produce a film of 100nm. A shadow mask allowed pixel areas to be defined, such as the six pixel design shown in Figure 3-1d. The cathode connected the top of the photoactive layer with the ITO contacts at the edge of the substrate.

3.5.5 Encapsulation

Once all of the device layers had been deposited, a glass slide was secured to the substrate with a UV curable epoxy resin. This sandwiched the device layers and heavily reduced the amount of water and air that they would be exposed to when removed from the glovebox environment.

3.6 Solar Spectrum Simulator

One of the main goals of solar cell research is to produce devices that efficiently harvest sunlight. It is therefore important to find the efficiency of such devices under illumination of a simulated solar spectrum and intensity. Device characterisation was performed using a Newport 92251A-1000 solar simulator with a power output of $100\text{mW}/\text{cm}^2$ and an AM1.5 spectrum. A certified NREL silicon reference cell was used to calibrate the system. The illuminated area was defined using a shadow mask in order to negate edge effects when testing devices [3]. A Keithley 237 sourcemeter was used to perform a voltage sweep from -1V to 1V and measure the resultant current response from a solar cell while under illumination.

3.7 Light Beam Induced Current Mapping

While testing devices under a solar simulator provides characteristics of the whole cell, it provides no information about variation in current generation over the film surface. Light beam induced current mapping (LBIC) allows characterisation of lateral variations in current generation over the device area. A schematic of the current

mapping system used in this thesis can be seen in Figure 3-2. A laser of wavelength 405nm was focused down through an objective lens to a spot size of $<5\mu\text{m}$. Two Thorlabs LTS300 translation stages were attached together perpendicularly to create an XY stage and positioned underneath the objective lens. A beam chopper was positioned in the path of the beam and connected to a lock in amplifier to recover the signal. A device holder with electrical contacts was fastened to the movable platform on top of the stages and connected to the lock in amplifier.

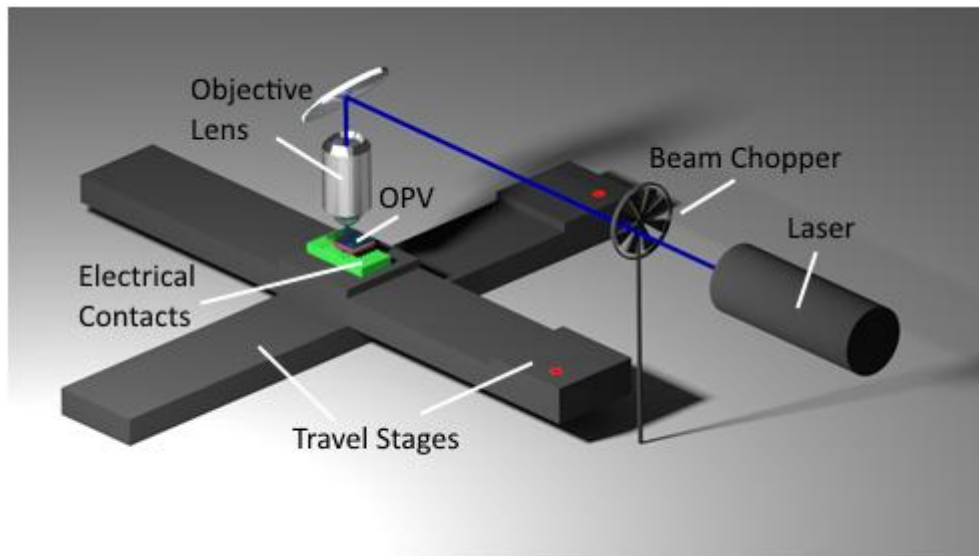


Figure 3-2: A schematic of a light beam induced current mapping system.

The stage was operated via USB connection to a computer and the lock in amplifier was controlled via a GPIB connection. A custom program to operate the system was written using the LabVIEW programming language. The program operated the lock in amplifier, moved the stage and stored measured current. The stage moved in a raster pattern, with step sizes determined by the user. Step sizes ranged from $1\mu\text{m}$ to $100\mu\text{m}$, depending on the desired resolution, area and time constraints of the measurement. Measurements required a settle time to ensure accurate readings after each step. Figure 3-3a) shows an LBIC map taken with a time delay of $<1\text{s}$ between measurements. This creates artificial 'streaks' as the scan reaches the edge of a pixel. The arrows indicate the scan direction. The lock in amplifier did not have enough time to measure the change in current as the laser spot moves off (red arrow) or on to (black arrow) the edge of a pixel. Figure 3-3b shows line profiles of

two arrows from 3a. To eliminate this effect, a pause of ~ 1 second was introduced between each measurement. Measuring a 165mm^2 pixel using a step size of $1\mu\text{m}$ would require 165000000 data points, taking over five years with a 1 second pause. Large scale measurements were therefore performed using a higher step size and provided a lower resolution.

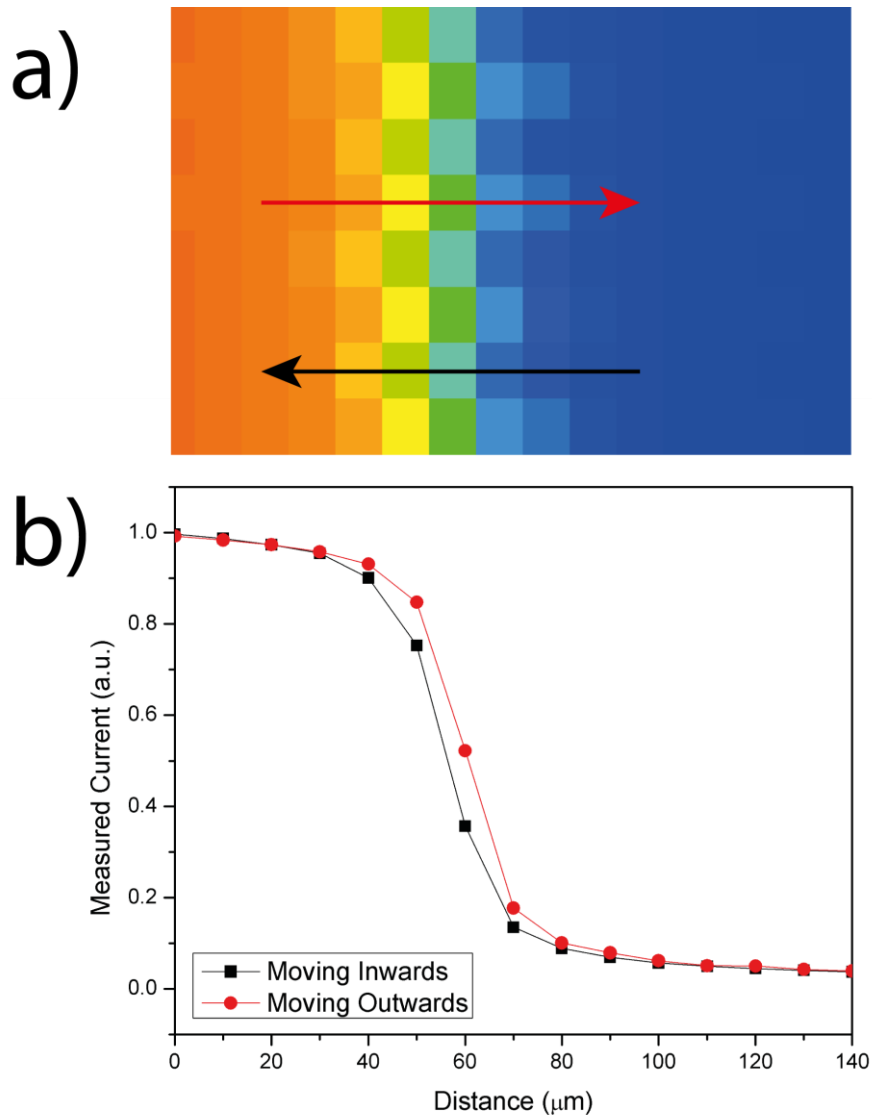


Figure 3-3: A section of a scan performed using a short settle time, resulting in artificial 'streaks' dependent on scan direction. Stage step size was $10\mu\text{m}$.

To focus the beam, line profiles were taken by scanning from one pixel to another, via the 'dead' area between pixels. The smaller the spot size incident on the device, the larger this gap between pixels will appear in the measurement. The transition to

generating current will also be more abrupt with a smaller spot size, represented by a steep slope in a line profile. Figure 3-4 shows line profiles taken at various lens to substrate distances. The $n + 150\mu\text{m}$ line shows the largest gap between pixels and a steep slope, indicating a well-focused beam. It also shows a lower generated current when incident on a pixel, indicating that the laser spot size is reduced compared to the other lens distances.

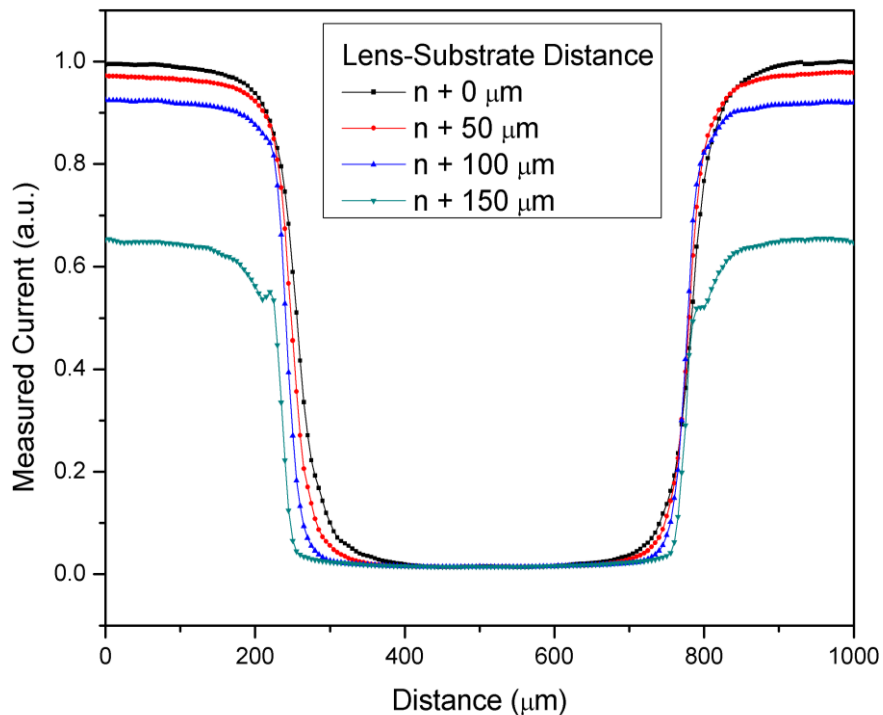


Figure 3-4: Line profiles taken at various lens-substrate distances during the focussing process. The gap between two device pixels allows the user to determine when the spot size is smallest.

3.8 Atomic Force Microscopy

Atomic force microscopy (AFM) provides small scale characterisation of a film surface. A schematic of an AFM is shown in Figure 3-5. A cantilever with a nanometre scale tip is scanned across the surface of a film. The tip is deflected by the surface of the film, and the measurement of this deflection gives information on the surface structure. To measure the deflection, a laser is reflected off the cantilever and into a quadrant photodiode. The position of the resultant laser spot

on the photodiode changes with tip deflection. The film to be investigated is placed on a piezoelectric X,Y stage beneath the probe and moves in two dimensions relative to the tip.

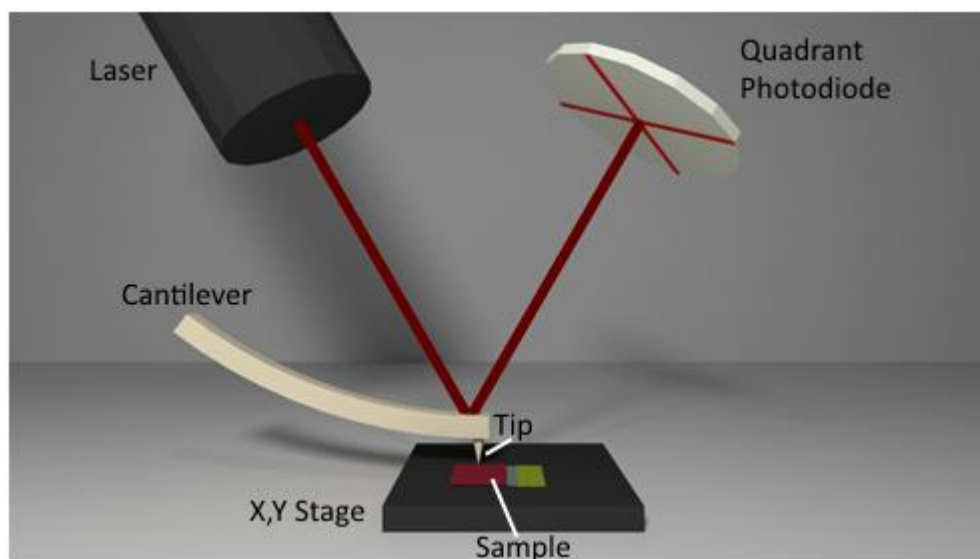


Figure 3-5: Simplified schematic of an atomic force microscope. A laser is reflected off a cantilever and into a photodiode, allowing the AFM to measure variation in surface height as the cantilever moves up and down.

The AFM can be operated in contact mode, non-contact mode and tapping mode. Contact mode drags the tip along the surface, measuring the height of the film directly from the deflection of the tip. Non-contact mode oscillates the tip at a low amplitude and measures height via the change in amplitude and frequency of the tip when it is at the surface. Tapping mode oscillates the tip at a large amplitude, repeatedly coming into contact with the surface. Tapping mode reduces the shear forces which would scratch the delicate films, therefore it is the mode used in this work. In tapping mode, height is given by the oscillation of the amplitude of the cantilever, while phase is determined by the difference in oscillation of the cantilever relative to the driving signal.

3.9 Contact Angle and Surface Tension

Contact angle measurements were conducted using a Theta optical tensiometer. The desired sample is prepared and placed on an adjustable stage. A CCD camera

capable of high speed photography is aligned with the stage and focused on the substrate. The solution to be investigated is held in a syringe above the substrate and close to the surface. The camera is set to take hundreds of images at 16ms intervals. Once the camera begins recording, a droplet of solution is released from the syringe and lands on substrate below.

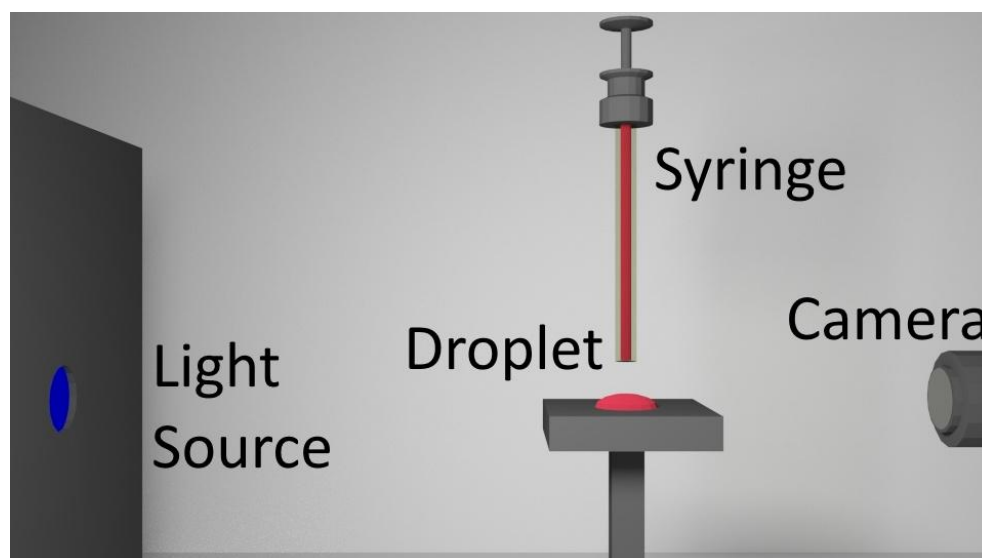


Figure 3-6: Simplified schematic of an optical tensiometer. A light source illuminates a droplet upon a stage and a camera captures an image.

Figure 3-6 shows a typical image taken using a tensiometer. This example shows a droplet of a PEDOT:PSS solution upon an ITO substrate. The user inputs the location of a horizontal substrate baseline and image processing software fits an ellipse to the droplet, extending it below the level of the substrate. The software then uses this information to calculate the left and right contact angles Θ of the droplet in each recorded frame. For surface tension measurements, a droplet is held at the point of dropping while an image is recorded. Surface tension is calculated via fitting a curve to the droplet silhouette.

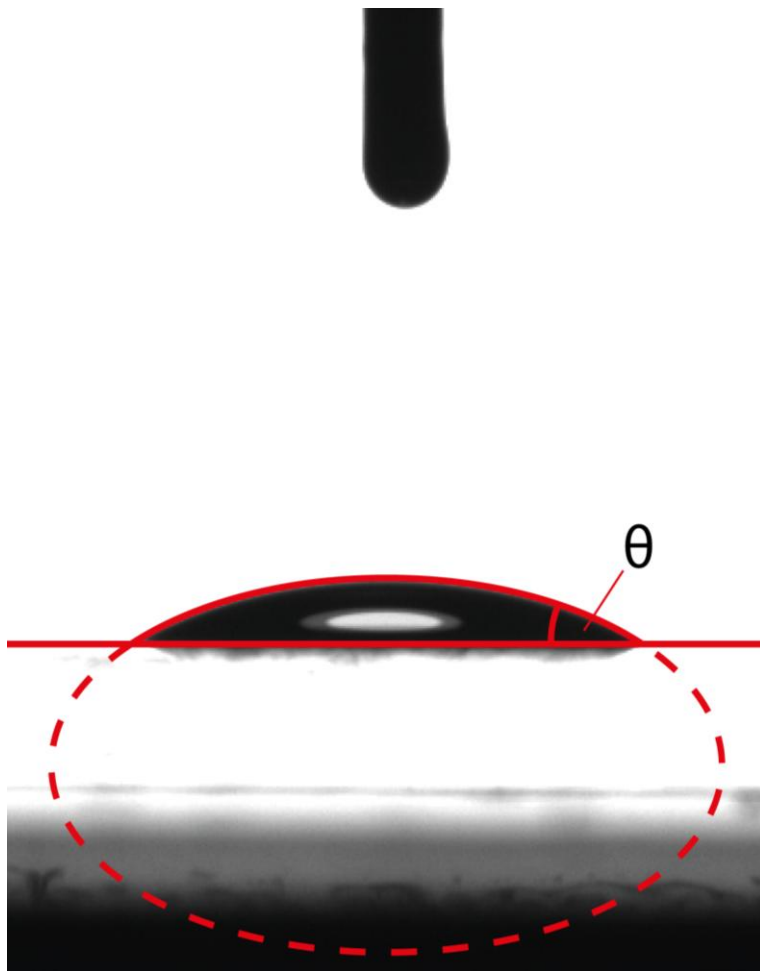


Figure 3-7: An image of a droplet on a substrate captured using an optical tensiometer. Image processing software is used to calculate the contact angle Θ .

3.10 Optical Absorption

UV-vis absorption was measured using a Horiba Fluoromax-4 spectrometer as shown in Figure 3-8. A xenon light source is focused on to the entrance slit of a monochromator using an elliptical mirror. Slit width controls the intensity of light allowed to enter the monochromator section. A second mirror then collimates light onto a blazing diffraction. Diffracted light is then reflected by a third mirror through a second slit. The angle that the diffraction grating makes with the incoming light determines the wavelength of light directed through this slit. Slit width can therefore be used to tune the wavelength resolution of the incoming light, as a narrower beam allows fewer wavelengths of diffracted light through it. Light is then reflected through a beam splitter on to a sample. The split beam enters a reference

detector which measures the light intensity incident on the sample. A second detector sits behind the sample, and measures the transmitted light.

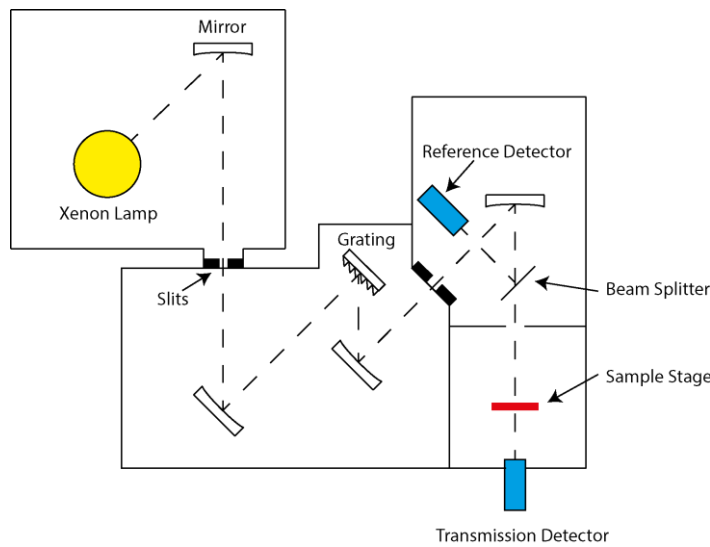


Figure 3-8: A simplified schematic of a UV-vis spectrometer.

The transmittance is calculated using the equation

$$Transmittance(\lambda) = \frac{I_t(\lambda)}{I_0(\lambda)} \quad \text{Equation 3.3}$$

where I_0 and I_t are intensities of the light incident on the sample and transmitted light respectively. To measure the transmittance of a deposited film, the transmittance of the substrate must also be measured as a reference, so as to account for its absorption when measuring both layers at once. The contribution to the transmittance of the sample film alone can then be determined.

3.11 Optical Ellipsometry

Ellipsometry measures changes in the polarisation of light as it reflects off a sample. These changes are caused by the optical properties and thickness of the materials that the light passes through while being reflected. If the optical properties of a film can be modelled, then the film thickness can be determined. Figure 3-9 shows a simplified schematic of an optical ellipsometer. Light is passed through a monochromator and polarised before reflecting off the sample under investigation.

The light then enters an analyser which determines the change in polarisation between the emitted light and the incoming light. Software is used to construct a model of the sample being studied. The model must take into account the thicknesses, refractive indices and extinction coefficients of the reflective substrate and the layer of interest. This information is well established for the Silicon wafers used in this work, therefore the difference between the measured data and the estimated fit is primarily due to the deposited film.

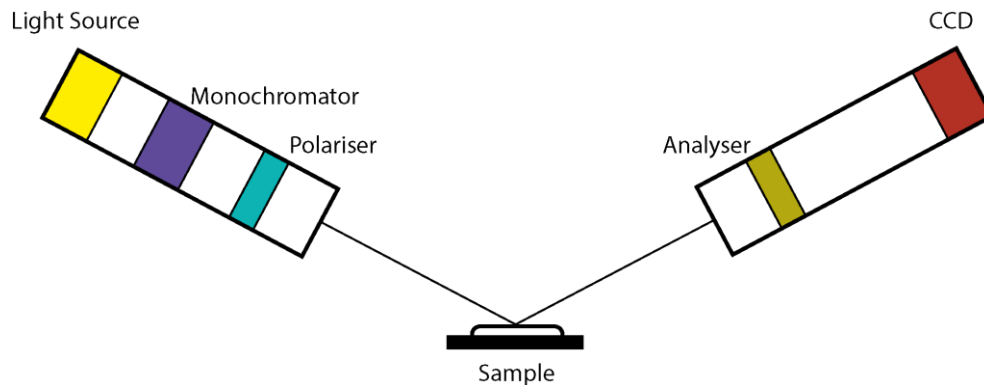


Figure 3-9: A simplified schematic of an optical ellipsometer. Polarised light is reflected off a sample and into and into an analyser to determine its change in polarisation due to passing through the sample layers.

3.12 References

- [1] K. Norrman, A. Ghanbari-Siahkali, and N. B. Larsen, "6 Studies of spin-coated polymer films," *Annu. Reports Sect. "C" (Physical Chem.*, vol. 101, p. 174, Oct. 2005.
- [2] A. G. Emslie, F. T. Bonner, and L. G. Peck, "Flow of a viscous liquid on a rotating disk," *J. Appl. Phys.*, vol. 29, no. 5, pp. 858–862, 1958.
- [3] A. Cravino, P. Schilinsky, and C. J. Brabec, "Characterization of organic solar cells: The importance of device layout," *Adv. Funct. Mater.*, vol. 17, no. 18, pp. 3906–3910, 2007.

Chapter 4 Spray Coating and Scale Up of PCDTBT:PC₇₀BM As a Photoactive Material

4.1 Introduction

At the present time, most prototype organic photovoltaic (OPV) devices are fabricated via spin-coating on to relatively small substrates. While spin-coating is a powerful tool for controllable and accurate material deposition, it is a relatively slow process and not easily scalable. In order for the technology to progress into a commercial manufacturing, the fabrication of devices must be demonstrated via scalable deposition techniques. Many such scalable techniques have already been used in the fabrication of OPVs. There has been progress in printing using techniques such as gravure [1], slot die [2], inkjet [3] and screen printing [4]. These have all demonstrated compatibility with OPV layers.

One of these roll-to-roll compatible techniques currently gaining increased attention is ultrasonic spray coating. This technique can be used to rapidly deposit a variety of materials from a range of inks with varying physical properties. There are many types of spray coating, with airbrush being the most common in the literature. This technique has notably been used to deposit the popular donor:acceptor combination P3HT:PCBM [5]–[8]. Ultrasonic spray coating has also been demonstrated as an effective deposition technique. Girotto et al. achieved a PCE of 3.75% by ultrasonic spray coating a P3HT:PC₆₀BM blend. Table 4-1 shows the results of a literature review into spray cast photoactive layers in OPV devices. Several reports have achieved spray cast device performances comparable to those of spin cast devices.

Spray Technique	PCE (%)	Pixel Area (mm ²)	Sprayed Photoactive Layer Materials	Rms Roughness (nm)	Citation
Airbrush	2.83	16.4	P3HT:PC ₆₁ BM	52	Vak 2007[8]
Airbrush	2.8	3.4	P3HT:PC ₆₁ BM	12.91	Giroto 2009[9]
Airbrush	2.7	20	P3HT:PC ₆₁ BM	24.1	Hoth 2009[10]
Ultrasonic	3.5	-	P3HT:PC ₆₁ BM	4	Steirer 2009[11]
Airbrush	2.17	4.66	P3HT:PC ₆₁ BM	-	Na 2010[12]
Airbrush	3.4	4.75	P3HT:PC ₆₁ BM	13	Yu 2010[13]
Ultrasonic	3.75	3	P3HT:PC ₆₁ BM	1.1	Giroto 2011[14]
Airbrush	5.8	15	P1: PC ₆₁ BM*	1.29	Nie 2012[15]
Ultrasonic	4.3	4.5	PCDTBT:PC ₇₁ BM	15	Wang 2013[16]
Airbrush	4.1	-	P3HT:PC ₆₁ BM	11.3	Tait 2013[17]
Airbrush	4.2	10	P3HT:PC ₆₁ BM	50	Vak 2015[18]

Table 4-1: A literature review of OPV photoactive layers deposited via spray coating. *poly[4,8-bis(1-pentylhexyloxy)benzo[1,2-b:4,5-b']dithiophene-2,6-diyl-alt-2,1,3-benzoxadiazole-4,7-diyl.

Most pixel sizes have been < 5 mm² however; therefore the true scalability of the proposed techniques has not been fully demonstrated. There is as yet no standardised way of demonstrating the scalability of deposition techniques, which leads to some reports lacking key information such as pixel size and film surface roughness. Device active areas are often given with no indication of the number of individual pixels that area encompasses, or even device geometries. These are important factors, as device architectures with many small pixels do not represent the scalability of a technique in the same way that a large single pixel of the same area would.

4.2 Chapter Summary

An ultrasonic spray coating process is optimised for the deposition of PCDTBT:PC₇₀BM photoactive layers. Ink formulation and deposition parameters are explored including: solvent blend, spray speed, solution concentration, deposition temperature, layer thickness and spray height. An optimised deposition process is used to fabricate devices on both small-area and large-area device architectures,

and the effect of scale-up on performance is discussed. Film uniformity is characterised via atomic force microscopy, profilometry and light beam induced current mapping.

4.2.1 Device Preparation

The vertical device architecture used in this chapter is displayed in Figure 4-1a. The materials and thicknesses of the materials in the stack are as follows: ITO/PEDOT:PSS (30 nm)/PCDTBT:PC₇₀BM/Ca (5 nm)/Al (100 nm). The thickness of the PCDTBT:PC₇₀BM layer will vary throughout the chapter. Device preparation and fabrication is discussed in Chapter 3. Three device architectures are used in this chapter, shown in Figure 4-1(b), (c) and (d). The six pixel substrate shown in (b) is used for the optimisation stages of this chapter, with the larger area 36 pixel (c) and single pixel (d) employed during scale up in section 4.7.

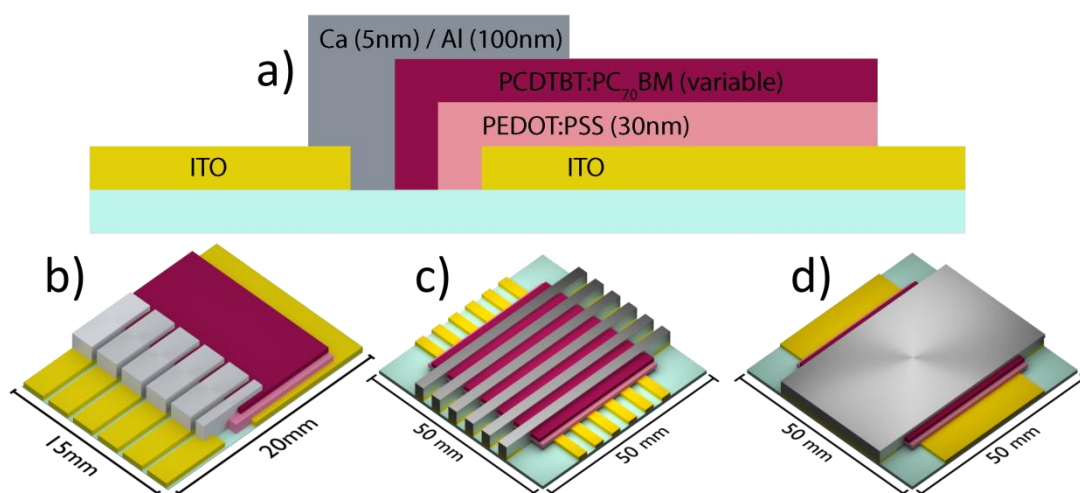


Figure 4-1: Schematics showing a) vertical device structure and device architectures for b) a small 6 pixel substrate, c) large 36 pixel substrate and d) a large single pixel substrate.

This range of substrate architectures are designed to investigate the scale up potential of the ultrasonic spray coating technique. The small 6 pixel substrate (b) is used for initial ink optimisation and material characterisation. The large 36 pixel (c) architecture has similar pixel sizes to the small 6, as displayed in Table 4-2. It is therefore a useful tool for exploring the effect of spray coating over larger

substrates, without needing to account for the potential detrimental effect of an increase in pixel size. The large single pixel (d) represents the final stage of the scale up investigation process; investigating the effects of a substantial increase in pixel size.

Architecture Name	Substrate Dimensions mm x mm	Pixel Dimensions mm x mm	Pixel Area mm ²	Pixels Per Substrate
Small 6	20 x 15	2 x 2	4	6
Large 36	50 x 50	2.54 x 2.54	6.45	36
Large Single	50 x 50	30 x 30	900	1

Table 4-2: Substrate dimensions, pixel number and pixel areas for the device architectures used in this chapter.

The donor:acceptor ratio for the PCDTBT:PC₇₀BM system has been extensively studied in the literature and a weight ratio of 1:4 has been shown to be an effective donor:acceptor ratio [19]. The PCDTBT used in this chapter had a Mw of 26.5 kDa and was synthesised by Hunan Yi according to a previously reported method [20]. PC₇₀BM was purchased from Ossila Ltd. and used as received.

4.3 Deposition Parameters

4.3.1 Spray Speed

Spray speed can be used to control the volume of solution deposited upon a substrate during the spray coating process. It is one of several parameters that can be tuned during the optimisation of a material deposition. Dry film thickness has a large dependence on volume deposited; the more material in solution, the more will remain once the carrier solvent has evaporated. A PCDTBT:PC₇₀BM solution of concentration 8 mg ml⁻¹ was spray cast on to ITO substrates held at a temperature of 40°C. Deposition spray speed was varied and images of the resultant films were scanned using an Epson Perfection V370 scanner; they are displayed in Figure 4-2. Film thicknesses were measured using a Dektak stylus profilometer. In addition to the film thickness, spray speed also has a clear effect on the quality of the dry film.

Speeds below 80 mm s^{-1} result in a drying edge enclosing a smooth film. Films cast as speeds above 140 mm s^{-1} are not continuous and uniform.

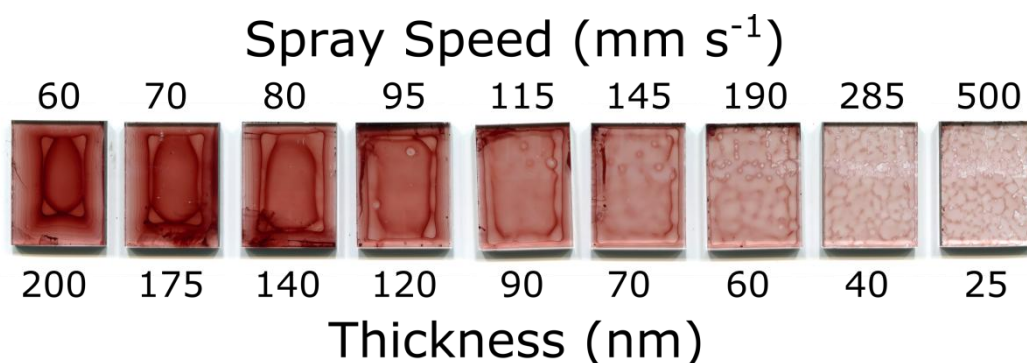


Figure 4-2: Scanned images of PCDTBT:PC₇₀BM films deposited at varying spray speeds. All films were deposited on to substrates held at 40°C.

Thickness as a function of spray speed is displayed in Figure 4-3. The relationship between spray speed and film thickness appears to follow an inverse function described by the equation:

$$\tau = \frac{A}{\text{spray speed}} \quad \text{Equation 4.1}$$

where τ is film thickness and A is constant that depends on several factors involved with the spray coating process which will be discussed in this chapter. The value of A in Figure 4-3 is $11790 \text{ nm mm s}^{-1}$, or $11790 \mu\text{m}^2 \text{ s}^{-1}$.

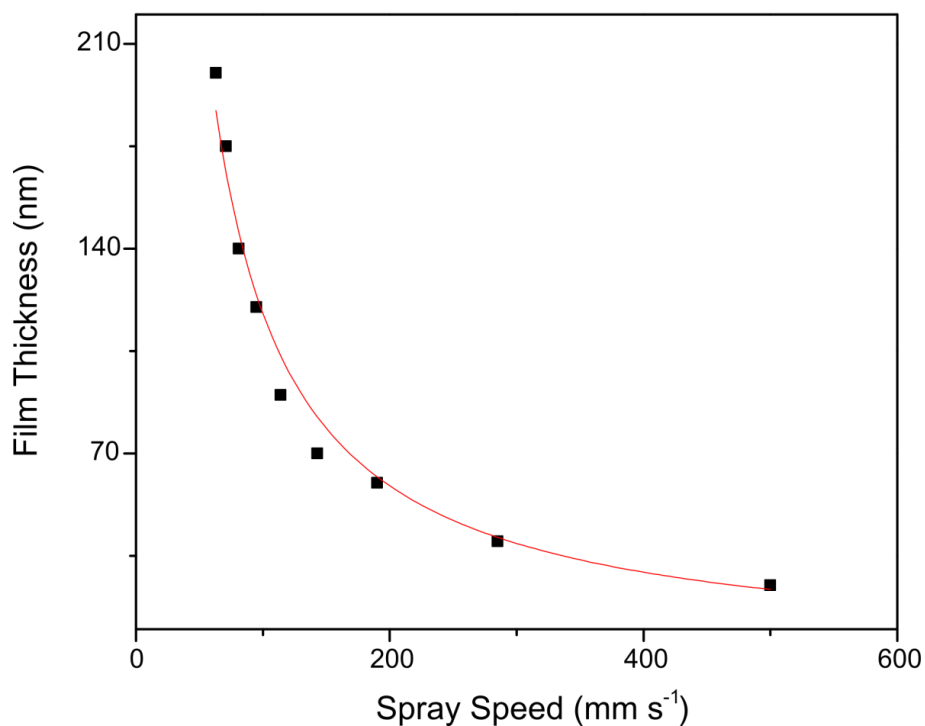


Figure 4-3: A plot of PCDTBT:PC₇₀BM film thickness as a function of spray speed. Substrate temperature was 40°C, solution concentration was 8 mg ml⁻¹ and the spray head to substrate distance was 35 mm.

Spray speed not only affects final film thickness, but also the quality of the film once it has dried. An increase in solution volume leads to an increase in drying time, and this can have a large effect on the morphology of the film. Figure 4-4 shows the three left-most films of Figure 4-2, each spray cast at low speeds. Drying times of > 50 s result in large drying edge that slowly ingresses to the centre of the substrate causing a 'picture framing' effect. The longer the drying time, the larger the drying edge and the smaller the smooth central film region. On smaller substrates with a width of 15 mm, this has a large impact on the pixelated regions that run across the substrate centre.

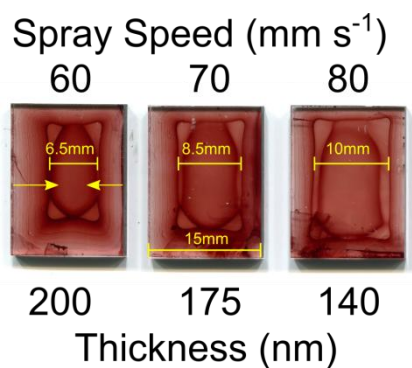


Figure 4-4: PCDTBT:PCBM films deposited via spray coating at lower spray speeds. Increased drying time causes an inward-moving drying edge. All films were deposited on to substrates held at 40°C.

The spray coating recipe must therefore be optimised so that the desired final film thickness can be achieved with a fast drying time, so as to minimise the drying edge ingress. This can be achieved by reducing the volume of solution deposited per substrate. Conversely, if too little solution is deposited then drying times are too fast and spray cast films will not properly form, as displayed in Figure 4-5. These films all had drying times of less than 14 seconds. This fast drying time creates 'coffee rings', wherein droplets dry before merging. This has been seen in other spray coating studies and is a common phenomenon in spray cast films [21][22]. They are characterised by regions of no coverage and giraffe patterns of thicker material. It is therefore clear that the drying time of the deposited material is crucial in the optimisation of a recipe.

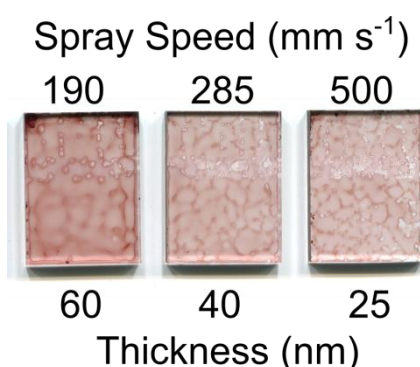


Figure 4-5: PCDTBT:PC₇₀BM films deposited via spray coating at higher spray speeds. Fast drying times prevent the film from coalescing before the bulk of the film is dried. All films were deposited on to substrates held at 40°C.

The two cases illustrated here indicate that there are definite limits to the solution volume that can be deposited. When droplets reach the substrate, they begin to spread and merge with each other; this must be allowed to occur before the solvent evaporates. If the drying time is too long however, a drying ring will spread into the film and cause a large reduction in film uniformity. There appears to be a 'sweet spot' between the two examples above, in which a uniform film can form before drying with a minimal edge ring. Figure 4-6 displays three examples of such films.

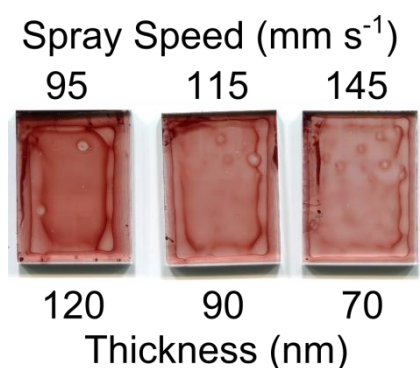


Figure 4-6: PCDTBT:PCBM films deposited via spray coating at medium speeds. Solution droplets have time to merge, yet dry fast enough to minimise drying ring ingress. All films were deposited on to substrates held at 40°C.

As described in Equation 4.1, there is a significant relationship between spray speeds and final film thickness. The spray speed boundaries imposed by drying time coupled with this relationship define a limited range of thicknesses achievable for a given solution. The preferred thickness of a PCDTBT:PC70BM layer is established in the literature to be 50 – 70 nm [23][16]. If this thickness range lies outside the uniform film boundaries, efficient devices cannot be fabricated. This problem could perhaps be avoided by changing device architecture so that device pixels are all situated inside the drying rings, where the film remains uniform. The standard architecture for large scale production is long thin pixel strips running along a substrate. If the entire width of the substrate was coated simultaneously, perhaps only the edges would suffer from these effects and the pixels themselves would remain untouched.

4.3.2 Deposition Temperature

One way of shifting the solution volume boundaries is to change the temperature of the substrate on to which the solution is deposited. This alters the drying time of a given solution volume, thus reducing the drying ring of high volume depositions. Films deposited at various temperatures are displayed in Figure 4-7.

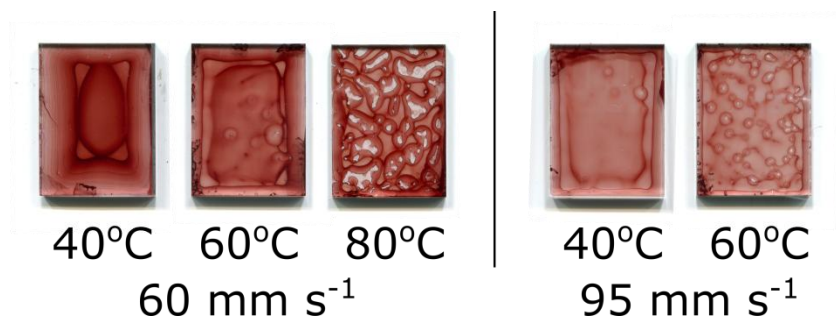


Figure 4-7: PCDTBT:PCBM films spray cast on to substrates of various temperature. Depositions are shown for two spray speeds.

The drying rings of a solution deposited at a spray speed of 60 mm s^{-1} can be dramatically reduced by increasing the temperature to 60°C as shown on the left of the image. If the temperature is increased to 80°C however, the solvent evaporates very quickly and droplets cannot merge into a uniform film. Solution volumes that resulted in uniform films when deposited at 40°C evaporate too quickly when deposited at 60°C , as shown on the right of the image.

4.4 Materials

4.4.1 Solvent Choice

Solvent choice plays an important role when spray coating organic solar cells. The surface tension of the solution determines how well it will spread when a droplet lands on a substrate surface. The lower the surface tension, the larger the spread and the better the solution will wet the surface. Figure 4-8 shows a drop of PCDTBT:PC₇₀BM in a CB solution landing on a spin-cast PEDOT:PSS substrate. The

droplet flattens quickly, spreading over the surface in less than a second. The initial contact angle is also small due to the low (4 mg ml^{-1}) concentration of the solution.

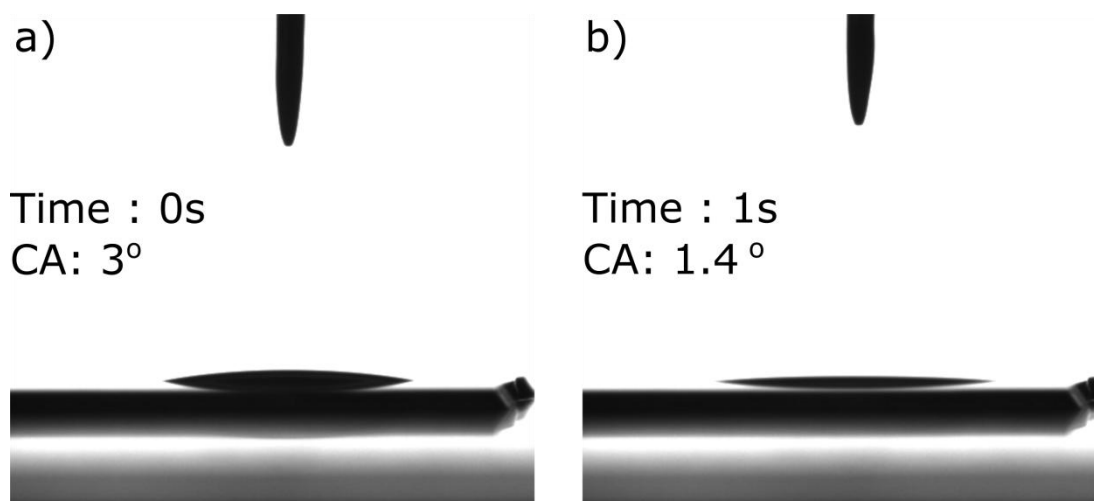


Figure 4-8: A droplet of PCDTBT:PC₇₀BM in CB spreading after contact with a PEDOT:PSS substrate.

Solvent choice can also affect the morphology of the dried film, particularly when depositing a donor:acceptor polymer system. Some solvent blends have been shown to encourage vertical stratification within the film, enabling regions favourable for charge transport. For example, a PCBM-rich area near the cathode can increase electron extraction in a PCDTBT:PC₇₀BM blend [24].

Three solvents were chosen for initial solution testing: chloroform (CF), chlorobenzene (CB) and dichlorobenzene (DCB). These solvents are extensively used in the field of organic photovoltaic's. PCDTBT:PC₇₀BM was dissolved in solvent blend of various ratios. An optical tensiometer was used to measure the surface tension of the blends and their contact angle upon PEDOT:PSS films. The results are displayed in Table 4-3. All of the blends have surface tensions of $\sim 30 \text{ mN m}^{-1}$ and relatively low contact angles when dropped onto PEDOT:PSS. The solutions should wet well when spray coating, as low surface tensions and contact angles allows droplets to spread over the film and merge before drying.

Solvent	Contact Angle (°)	Surface Tension (mN m ⁻¹)
CB	3.5	29
DCB	1.2	31.3
DCB:CB (1:1)	1.8	30.8
DCB:CF (7:3)	1.8	31.5
DCB:CF (6:4)	1.8	29.8
DCB:CF (5:5)	1.2	31
DCB:CF (4:6)	2.6	29.8
DCB:CF (3:7)	2.9	31.5

Table 4-3: Surface tension and contact angle of PCDTBT:PC70BM solutions with various blend ratios. Droplets were measured on substrates of PEDOT:PSS at room temperature.

While CB had the highest contact angle, this is still relatively low and indicates good wetting over the substrate surface.

The various DCB:CF solution blends detailed above were spray cast on top of PEDOT:PSS substrates held at a temperature of 50°C. The solution concentration was 4 mg ml⁻¹ and the tip to substrate distance was 35 mm. Twelve devices spread over two substrates were fabricated for each blend ratio.

Due to the challenges associated with spray coating materials, several devices did not function correctly. This number of 'dead' pixels may be due to several factors such as poor film formation, shorts in the film or a unwanted morphology. Because of this uncertainty, the completely dead devices do not give a useful indication of which solvent blends performed the best. Poorly performing devices will provide useful information for optimisation, however devices that don't work at all will not. There are rarely more than 50% completely dead pixels over two substrates, therefore the top 50% of data was chosen for analysis. The top 50% of devices are used throughout this chapter, except where stated. An obvious exception to this is when film uniformity is the object of investigation, as a more uniform film may produce fewer dead pixels, therefore the lack of working devices is a useful metric.

Figure 4-9 shows a box chart of the PCEs for the devices discussed above. Each box represents six devices and displays the minimum, maximum, mean (open square), median (horizontal line) and the interquartile range of the data.

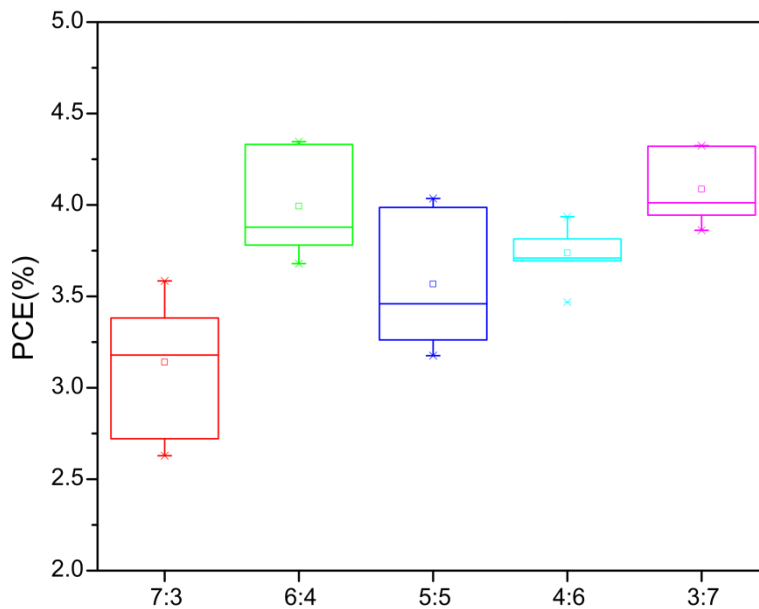


Figure 4-9: Box chart displaying the power conversion efficiencies of devices fabricated from solvent blends of DCB and CF. The layers were deposited at a temperature of 50°C, a spray height of 35 mm and a spray speed of 80 mm s⁻¹. Solution concentrations were 4 mg ml⁻¹.

There is a trend to higher PCE with increasing chloroform concentration. The 3:7 blend created the most efficient devices on average, while the 4:6 blend provided the smallest variation in performance. DCB has a higher boiling point than CF, therefore a given volume will take longer to evaporate. This slower drying process causes drying rings to form in the film similar to those shown in Figure 4-4. The blend ratios that have a higher DCB content show the largest spread in performance, which is consistent with the non-uniformity of the dry films. The performance characteristics of the devices are displayed in Table 4-4. There is an increase in short circuit current density and fill factor as the CF ratio increases.

Solvent	PCE (Average)	FF	J _{sc}	V _{oc}
	%	%	mA cm ⁻²	V
DCB:CF (3:7)	2.89 ± 0.35	37.1 ± 1.8	-9.63 ± 0.72	0.81 ± 0.02
DCB:CF (4:6)	3.67 ± 0.26	38.5 ± 1.3	-9.98 ± 0.81	0.81 ± 0.31
DCB:CF (5:5)	3.28 ± 0.33	39.0 ± 4.8	-10.68 ± 0.57	0.78 ± 0.02
DCB:CF (6:4)	3.44 ± 0.15	40.8 ± 1.3	-10.25 ± 0.14	0.82 ± 0.03
DCB:CF (7:3)	3.76 ± 0.18	43.1 ± 2.1	-10.41 ± 0.46	0.84 ± 0.01

Table 4-4: Performance characteristics of OPV devices fabricated with spray-cast PCDTBT:PCBM photoactive layers. Films were deposited from a range of solvent blends.

To investigate the impact of deposition temperature on device performance, devices were fabricated from blends of 7:3 and 3:7 at varying temperatures. Figure 4-10 shows the resultant device performance. The performance of the 7:3 blend increased with deposition temperature, whereas the 3:7 blend peaked at 50°C. The long drying time of DCB at low temperatures caused drying rings, and there is a larger spread in device performance as seen in the previous section. The decrease in drying times at higher temperatures reduced the impact of these rings, and the resultant device performance improved. The predominantly CF 3:7 blend performed worse at the highest temperature, as the films dried before the solvent could spread into a uniform film.

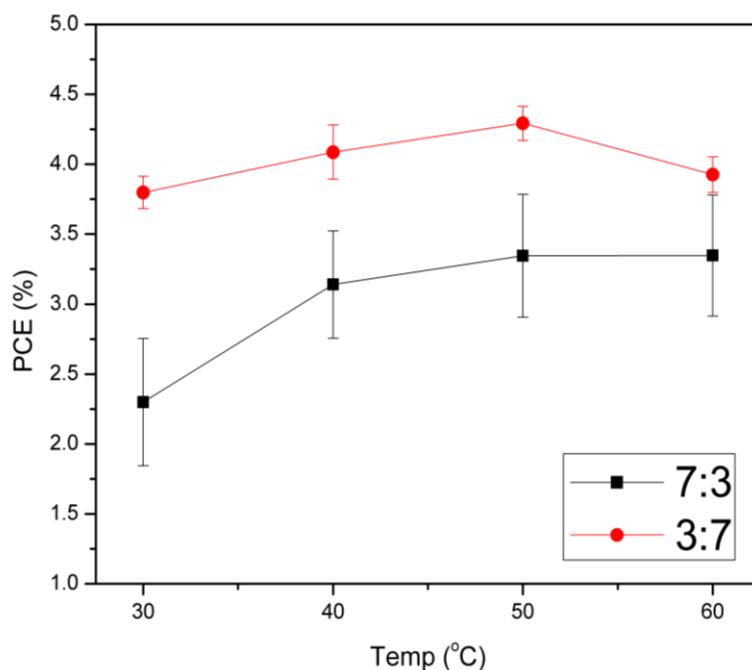


Figure 4-10: PCE as a function of deposition temperature for devices fabricated from solvent blends DCB and CF. Spray head to substrate distance was 35 mm, solution concentration was 4 mg ml⁻¹ and spray speed was 80 mms⁻¹.

Films sprayed from a solution of CF on its own did not form a good enough film for device fabrication as the solvent began to evaporate before reaching the substrate surface, resulting in an incomplete film. Along with the solvent blends, a single solvent system was also investigated using chlorobenzene (CB). Table 4-5 shows performance metrics for devices fabricated from a DCB:CF 3:7 blend and a CB single solvent system. A single solvent system appears to be more reproducible, with a lower spread in performance. The fill factor was increased significantly from 43.2 to 50.1. The increase in fill factor and consistency may both be due to increased uniformity of films produced by the CB solution.

Solvent	PCE (%)	FF (%)	J _{sc} (mA cm ⁻²)	V _{oc} (V)
CB	4.24 ± 0.06	50.08 ± 1.10	-10.14 ± 0.17	0.84 ± 0.01
DCB:CF (3:7)	3.76 ± 0.18	43.15 ± 2.17	-10.41 ± 0.46	0.84 ± 0.01

Table 4-5: OPV devices fabricated from a DCB:CF solvent blend and a CB single-solvent solution. Substrate temperature was 40°C, spray speed was 80 mm s⁻¹ and spray height was 35 mm.

Devices fabricated via film deposition from pure chlorobenzene solutions performed the best out of the various solvent blends, with power conversion efficiencies of 4.24% at a deposition temperature of 40°C. This solvent choice and deposition temperature are used for all of the PCDTBT:PC₇₀BM solution depositions in this thesis, unless otherwise stated.

The results in section 4.4.1 were published as part of an article by Tao Wang in reference [16]

4.4.2 Solution Concentration

The most obvious way to tune final film thickness for a given solution volume is to change the solution concentration, as an increase in solution concentration allows a thicker film to be deposited from a given solution volume. This is impractical when optimising the spray coating process however, as if all other parameters are kept constant then a new solution is required for every thickness. To achieve films of similar thicknesses at different concentrations, the volume of the solution must change. This therefore affects the drying kinetics of the films, and can result in poorer quality devices at the same thickness.

PCDTBT:PC₇₀BM layers were spray cast on to ITO/PEDOT:SS substrates from solutions of concentrations 4mg ml⁻¹, 8 mg ml⁻¹ and 10 mg ml⁻¹, and devices were fabricated as described in Chapter 3. Figure 4-11 shows PCE data for all three concentrations along with the standard deviation of the data. Although the films are all the same thickness, there is an increase in efficiency when films are cast from a solution concentration of 8 mg ml⁻¹. To achieve a specific thickness with the 10 mg ml⁻¹ solution, a smaller volume of solution must be deposited compared to the 8 mg ml⁻¹ or 4 mg ml⁻¹ solutions, therefore a faster spray speed is required.

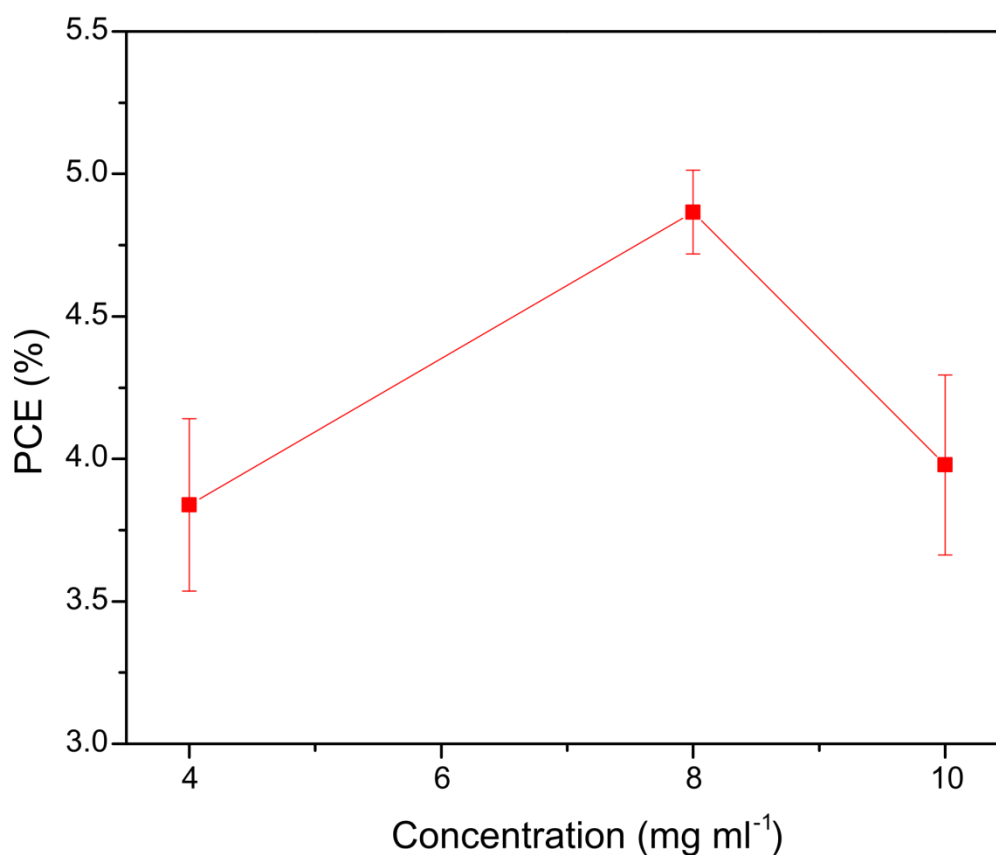


Figure 4-11: PCEs of OPV devices with spray cast PCDTBT:PC₇₀BM active layers of 60 nm thickness. Films were spray cast from three different solution concentrations: 4, 8 and 10 mg ml⁻¹. Substrate temperature was 40°C and the spray head to substrate distance was 35 mm. The spray speed varied between solutions so as to keep the final film thickness constant.

The reduction in wet film volume causes a decrease in drying time and results in films similar to those in Figure 4-5. The 8 mg ml⁻¹ solution however had time to form a uniform film before drying, resulting in a higher performance. When the concentration is at 4 mg ml⁻¹, the films take longer to dry and drying rings are more prominent.

4.4.3 Film Thickness

A concentration of 8 mg ml⁻¹ appears to allow for uniform films in a suitable thickness range for active layer deposition. The next phase in optimisation was to determine the appropriate film thickness of the PCDTBT:PC₇₀BM layer.

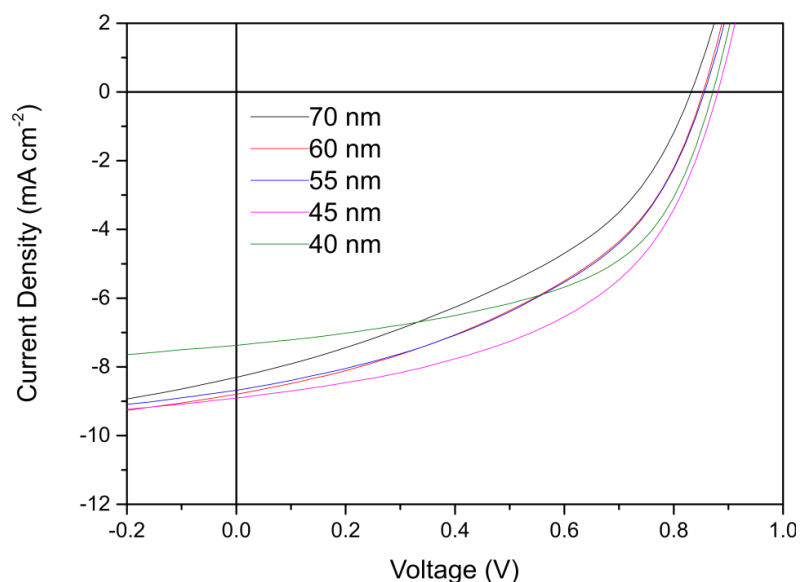


Figure 4-12: J-V characteristics of OPV devices fabricated via spray coating PCDTBT:PC₇₀BM layers at various spray speeds. Resultant film thicknesses are also displayed. Substrate temperature was 40°C, solution concentration was 8 mg ml⁻¹ and the spray head to substrate distance was 35 mm. Spray speed was varied to change final film thickness.

Figure 4-12 shows averaged J-V data for devices fabricated with different active layer thicknesses. There were six devices per thickness, the device metrics are displayed in Table 4-6. There is an increase in short circuit current as the layer thickness is reduced, which is indicative of the lower charge mobility of PCDTBT in thicker films. There could also be a contribution from the film morphology caused by a longer drying time.

Thickness (nm)	PCE (%)	FF (%)	J _{sc} (mA cm ⁻²)	V _{oc} (V)
70	2.81 ± 0.12	41.1 ± 0.84	-8.25 ± 0.26	0.83 ± 0.01
60	3.18 ± 0.26	43.6 ± 0.82	-8.54 ± 0.56	0.85 ± 0.00
55	3.32 ± 0.17	44.7 ± 1.50	-8.68 ± 0.51	0.86 ± 0.01
45	3.96 ± 0.04	50.6 ± 2.23	-8.91 ± 0.37	0.88 ± 0.01
40	3.48 ± 0.05	53.5 ± 2.40	-7.48 ± 0.32	0.87 ± 0.01

Table 4-6: Performance metrics of the devices characterised in Figure 4-12. Substrate temperature was 40°C, solution concentration was 8 mg ml⁻¹ and the spray head to substrate distance was 35 mm. Spray speed was varied to change final film thickness.

Upon reduction to a thickness of 40 nm, the short circuit current is once more reduced. This is likely due to the lower light absorption of the thinner films, reducing the photocurrent generation inside the cell. Figure 4-13 shows normalised absorption of spray cast PCDTBT:PC₇₀BM films of varying thicknesses. The peak absorption in the 40 nm films is 91% of the peak at 60 nm. This is comparable to the J_{sc} devices of the same active layer thicknesses, with the 40 nm devices obtaining 87% the J_{sc} of the 60 nm devices.

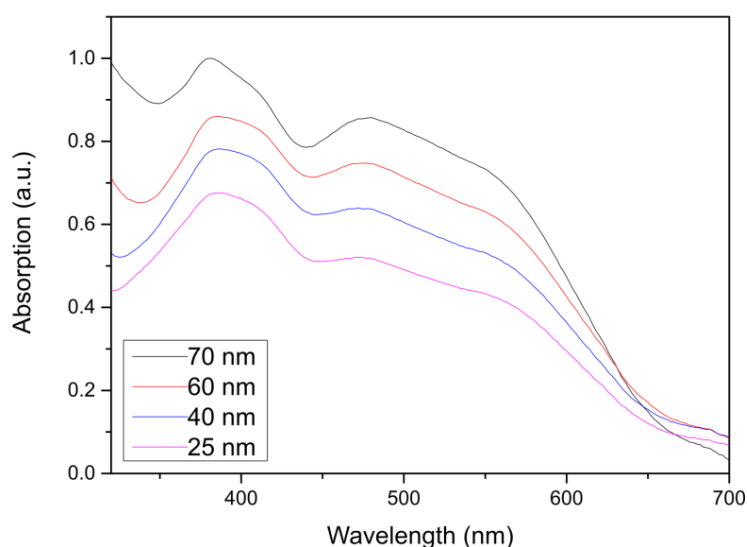


Figure 4-13: Absorption of spray cast PCDTBT:PC₇₀BM films of varying thickness. Deposition temperature was 40°C, solution concentration was 8 mg ml⁻¹, spray height was 35 mm and spray speed was 80 mm s⁻¹.

4.4.4 Spray Height

In order to deposit a film onto larger sized substrates, the height of the spray head may have to be increased in order to cover a larger area with solution. Due to the large parameter space when optimising a system for spray coating, it is useful to be able to predict a likely range of thicknesses for given set of parameters. It is therefore important to determine the change in solution volume deposited when the height of the spray head is altered.

Spray Speed (mm^{-1})	Thickness (nm)	
	Height 40 mm	Height 70 mm
53	220	110
100	90	55
150	50	30

Table 4-7: Film thickness dependence on spray head height. Deposition temperature was 40°C and solution concentration was 8 mg ml^{-1} .

The final film thicknesses in Table 4-7 appear to be inversely proportional to spray head height (i.e. doubling the height will half the film thickness). This provides an estimate for film thickness when optimising a material system for a different head heights.

4.5 Thermal Annealing

For some donor polymer systems such as P3HT:PCBM, it is well known that thermally annealing the active layer will increase device performance due to an increase in P3HT crystallinity and PCBM phase-separation [25].

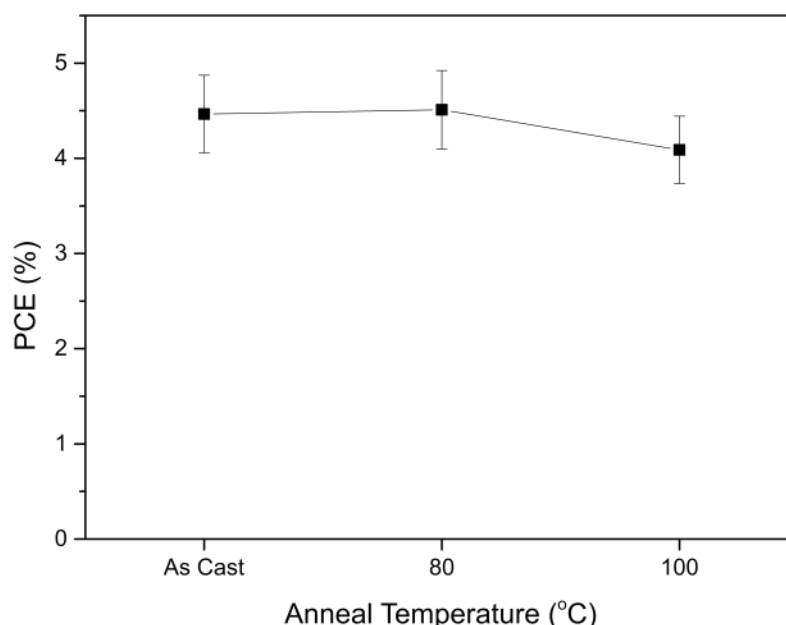


Figure 4-14: The effect of thermal annealing on device performance. Deposition temperature was 40°C , solution concentration was 8 mg ml^{-1} , spray height was 45 mm and spray speed was 150 mm s^{-1} .

Figure 4-14 shows the PCE and standard deviation of five devices as cast, after annealing at 80°C for 10 minutes and after annealing at 100°C for 10 minutes. There is no significant improvement in device performance when annealing at 80°C, and there is a slight decrease in performance at 100°C. The spread in device performance does not change dramatically during this process, indicating that the decrease in performance happened to every device. This result is in agreement with the literature, where it has been suggested that thermal annealing of a PCDTBT:PC₇₀BM system can reduce π - π stacking within the active layer, resulting in a reduction in hole mobility[26]. The PCDTBT:PC₇₀BM films in the remainder of this thesis were therefore not annealed after fabrication.

4.6 Film Uniformity

The active layer in a device stack should ideally be relatively smooth as this prevents issues when depositing an electrode material on to it. The calcium electron transport layer used in this work is only 5 nm thick, therefore a large surface roughness could prevent full surface coverage. An atomic force microscopy image of an 80 nm thick PCDTBT:PC₇₀BM layer is shown in Figure 4-15. The rms roughness over the 100 μm^2 surface area is 0.92 nm. This low roughness is comparable to the ultrasonically sprayed P3HT:PCBM layers reported by Giroto et al. wherein a rms roughness of 1.1 nm was achieved[7].

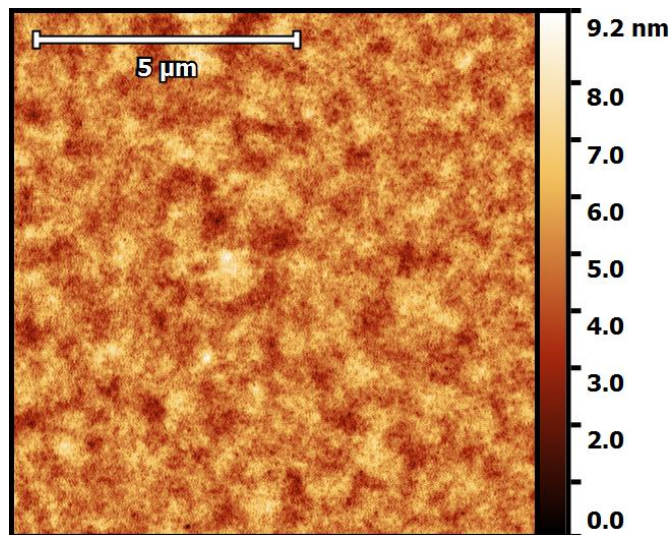


Figure 4-15: Atomic force microscopy image of a spray cast PCDTBT:PC₇₀BM film of 80 nm thickness. Rms roughness is 0.92nm over an area of 100μm².

While the AFM image demonstrates a smooth film, homogeneity of the film over larger areas is also desirable. Roll-to-roll production requires consistent performance between batches, therefore uniform photocurrent over a device is important to determine. Figure 4-16 shows a light beam induced current (LBIC) map of an OPV device fabricated with a spray cast PCDTBT:PC₇₀BM layer. The data has been normalised and the top 50% of generated current is displayed, so as to highlight the differences in current generation over the cell. There are over 18000 data points in the image, each taken during a 1 second interval. This was a time consuming experiment to complete, however the results give additional insight into how film morphology effects current generation within a cell. There is some variation in photocurrent generation over the four pixels, which appears to follow the pattern of drying edges created while the wet film was evaporating. These 'picture frame' effects have been reported previously as a result of droplets not merging properly before drying during deposition [27].

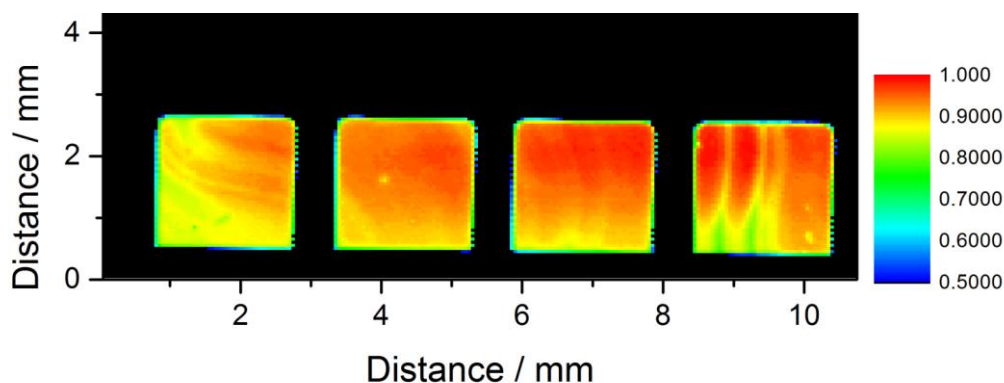


Figure 4-16: LBIC map of an OPV fabricated via spray casting a PCDTBT:PC₇₀BM photoactive layer. The scale has been normalised.

The LBIC data is displayed in the form of a histogram in Figure 4-17. Data points below 50% of the maximum signal are ignored, as they account for the ‘dead’ areas surrounding the pixels. A large part of the current generation is within 10% of the maximum value, with some outlying samples producing a reduced current.

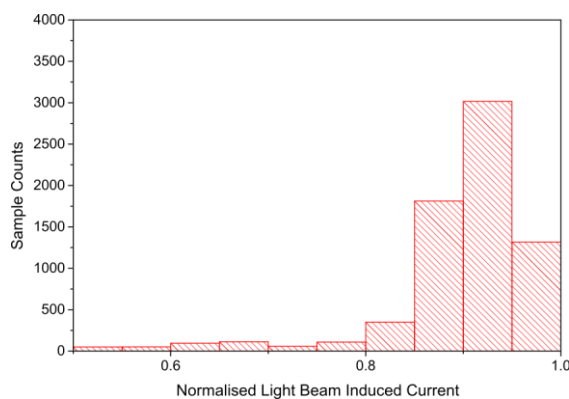


Figure 4-17: A histogram of the current map displayed in Figure 4-16.

While this is relatively uniform, a 10% variation in yield may not be suitable for large scale production. This issue could be resolved by improving overall film uniformity, or allowing for drying space at the substrate edge, with devices fabricated in the centre.

4.7 Scale Up

4.7.1 Large Area Surface Roughness

Once the PCDTBT:PCBM system had been optimised over a small scale substrate, a larger substrate design was chosen allowing film uniformity over a greater area to be investigated. A profilometer scan PCDTBT:PCBM film spray cast over an area of 40 mm x 40 mm is shown in Figure 4-18. Although the large scan has several streaks in it, the mottled PCDTBT:PCBM features can clearly be seen. The profilometer tip moved vertically with respect to the image and a line profile (inset) shows the variation in film height over a distance of 30 mm. The rms roughness over the entire 900 mm² is 30 nm, with a peak to trough distance of 18 μm.

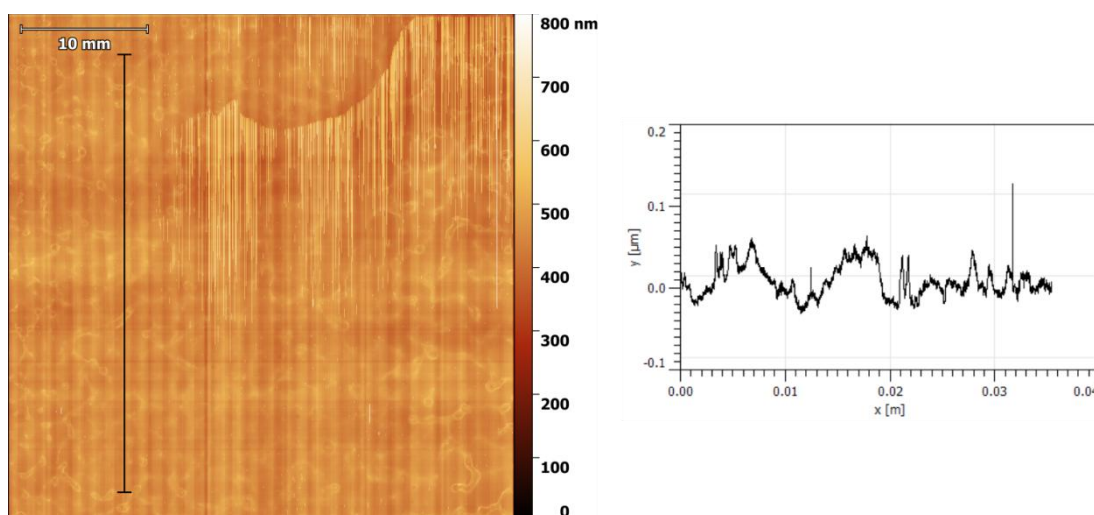


Figure 4-18: A profilometer scan of a PCDTBT:PC₇₀BM film spray cast over a large area. Rms roughness is 30 nm and over an area of 900 mm².

A smaller section of this scan was investigated further and line profiles are shown of some of the larger scale features of the film in Figure 4-19. The region with a cross section labelled as (a) has a roughness of ± 5 nm. Other regions are more textured (b) and have a 'mottled' surface with features having a vertical height of up to 40 nm. These features can be seen all over the film and are the cause of the mottled appearance of the completed device shown in Figure 4-21.

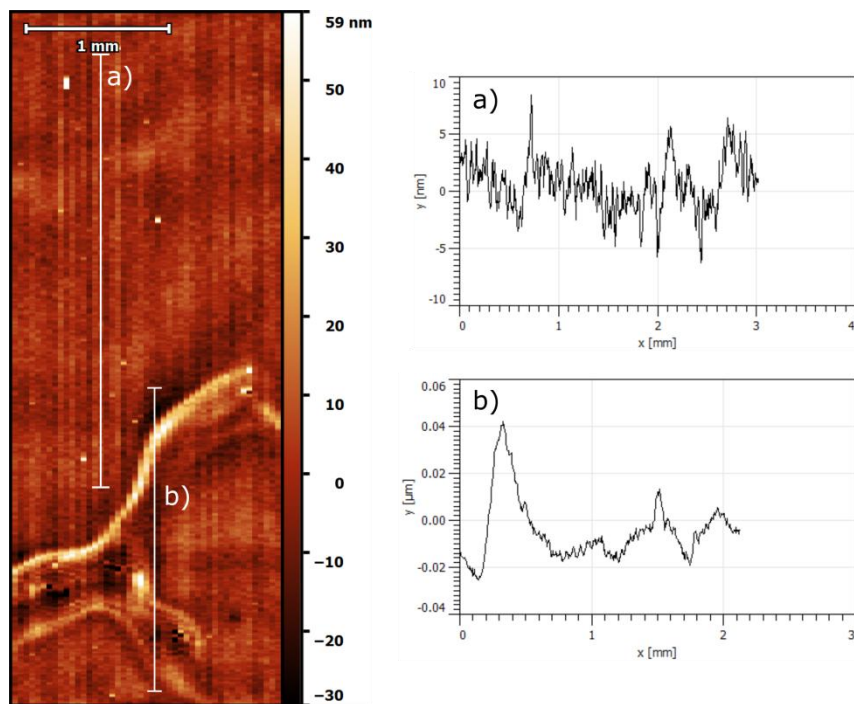


Figure 4-19: A profilometer map of a PCDTBT:PCBM film spray cast over an area of 25 cm². The map covers an area of 9mm² and has an rms roughness of 8.92 nm.

4.7.2 36 Pixel Architecture

A large device architecture with 36 individual pixels is displayed in Figure 4-1c. Pixel sizes are the same as with the smaller architecture (4mm²) in Figure 4-1b, therefore this provides an effective test of the deposition technique over a larger substrate. Devices were fabricated using the optimised recipe described earlier in this chapter and performance metrics are displayed in Figure 4-20.

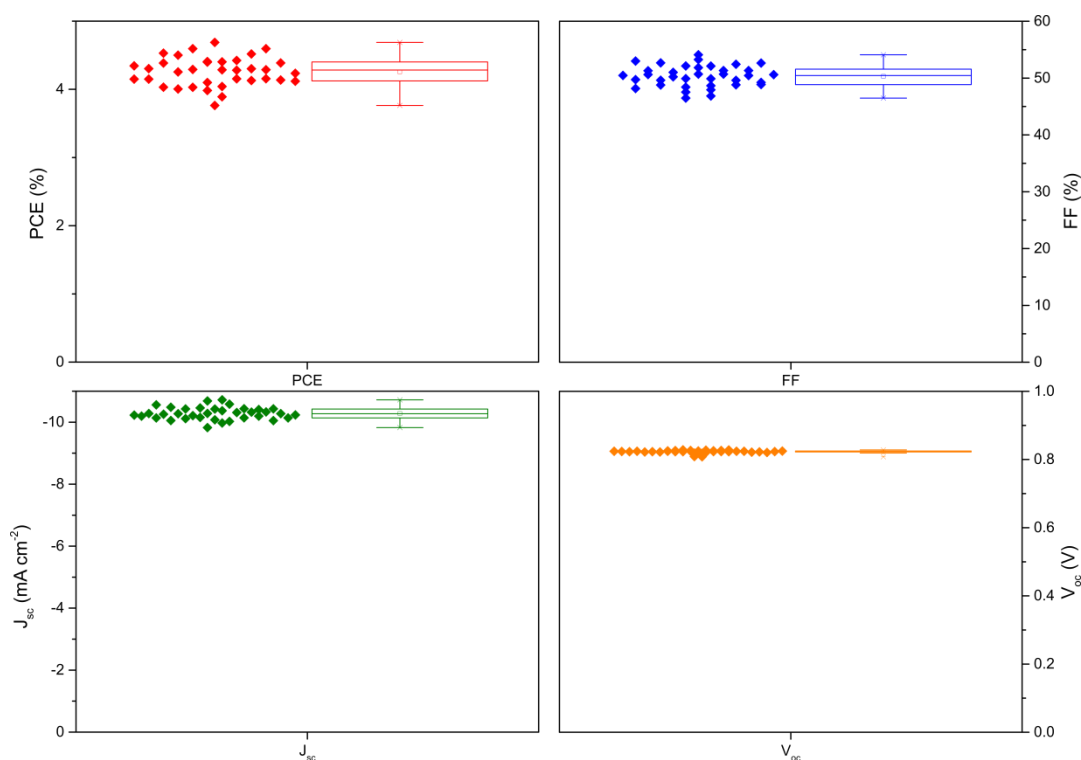


Figure 4-20: Performance metrics of a 36 pixel architecture OPV fabricated with a spray cast PCDTBT:PC₇₀BM photoactive layer. Deposition temperature was 40°C, solution concentration was 8 mg ml⁻¹.

The device has an excellent yield, with all 36 pixels achieving PCEs of over 3.5%. This high yield may be partly due to the larger gap between the substrate edges and the pixel locations, preventing the drying edge from reaching the main pixel device area. The mottling effect discussed in section 4.7.1 can be seen in a photograph of the device in Figure 4-21. This does not seem to have an impact on performance however, as the results are similar to those achieved with the small area device architecture.



Figure 4-21: A photograph displaying the small 6 pixel and large 36 pixel architectures after full fabrication.

4.7.3 Large Single Pixel

The previous section demonstrated a device with 36 individual pixels over large substrate area. The next stage in the scale up process is to increase pixel sizes themselves, with the aim of scaling up to a commercially desirable active area. For this purpose, a large single pixel cell was fabricated of area 900mm^2 using the architecture displayed in Figure 4-1c. This substrate type uses a pixel size two orders of magnitude greater in area than the architectures discussed earlier in this chapter. The current voltage characteristics of the device are shown in Figure 4-22 and performance metrics are displayed in Table 4-8.

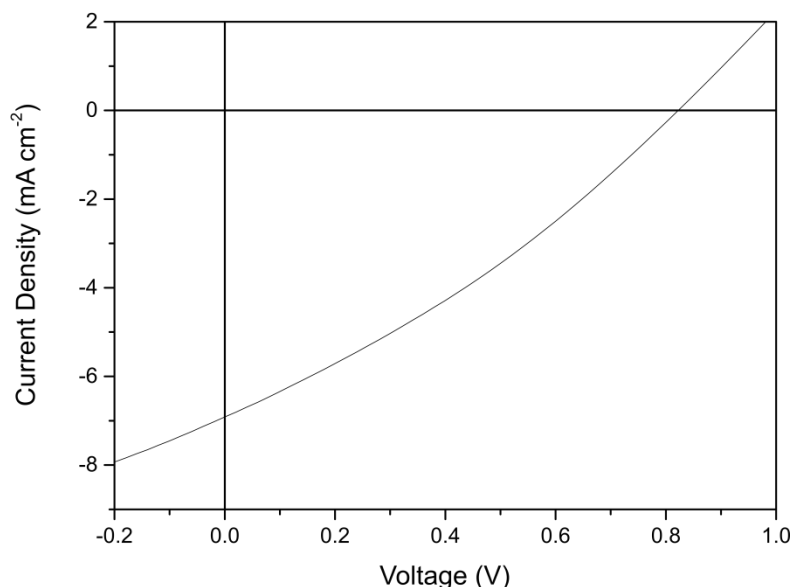


Figure 4-22: Current-voltage characteristics of a large single-pixel OPV in which the PCDTBT:PC₇₀BM active layer was spray cast. Deposition temperature was 40°C, solution concentration was 8 mg ml⁻¹.

There is a clear reduction in device performance as device area increases. V_{oc} is primarily affected by the work function of the electrodes and the difference between the donor HOMO and acceptor LUMO and is therefore independent of device area [28][29]. The V_{oc} is relatively high in this device, which it implies that the vertical morphology is consistent with the cells fabricated earlier in this chapter. A loss in fill factor is likely due to the large series resistance of the ITO anode[30]. This issue has been previously overcome via the use of metallic grids or bus-bars[31].

PCE (%)	FF (%)	J_{sc} (mA cm ⁻²)	V_{oc} (V)	R_{shunt} (Ω)	R_{series} (Ω)
1.75	30.7	-6.91	0.822	181	82.15

Table 4-8: Performance metrics of the large single pixel device characterised in Figure 4-22

4.8 Conclusion

An ultrasonic spray coating process has been optimised for the deposition of PCDTBT:PC₇₀BM active layers. The ultrasonic spray coater deposition technique was investigated and the following parameters explored: solvent blend, spray speed,

solution concentration, deposition temperature, layer thickness and spray height. An optimised process was then used to fabricate devices, with a maximum PCE of 4.79% achieved. The process was then applied to a large scale 36-pixel device, achieving a 100% yield and efficiencies above 3.5%. Finally, a 900mm² single pixel was fabricated with a PCE of 1.75% achieved. This demonstrates the feasibility of the spray coating process over a larger area. Light beam induced current maps show a variation in photocurrent generation across the cell on the same length scales of the film 'mottling'. Still more work is needed to understand the features formed during drying and their impact on performance.

4.9 References

- [1] P. Kopola, T. Aernouts, R. Sliz, S. Guillerez, M. Ylikunnari, D. Cheyngs, M. Välimäki, M. Tuomikoski, J. Hast, G. Jabbour, R. Myllylä, and A. Maaninen, "Gravure printed flexible organic photovoltaic modules," *Sol. Energy Mater. Sol. Cells*, vol. 95, no. 5, pp. 1344–1347, May 2011.
- [2] F. C. Krebs, "Polymer solar cell modules prepared using roll-to-roll methods: Knife-over-edge coating, slot-die coating and screen printing," *Sol. Energy Mater. Sol. Cells*, vol. 93, no. 4, pp. 465–475, Apr. 2009.
- [3] C. N. Hoth, S. A. Choulis, P. Schilinsky, and C. J. Brabec, "High Photovoltaic Performance of Inkjet Printed Polymer:Fullerene Blends," *Adv. Mater.*, vol. 19, no. 22, pp. 3973–3978, Nov. 2007.
- [4] F. C. Krebs, J. Alstrup, H. Spanggaard, K. Larsen, and E. Kold, "Production of large-area polymer solar cells by industrial silk screen printing, lifetime considerations and lamination with polyethyleneterephthalate," *Sol. Energy Mater. Sol. Cells*, vol. 83, no. 2–3, pp. 293–300, Jun. 2004.
- [5] G. Susanna, L. Salamandra, T. M. Brown, A. Di Carlo, F. Brunetti, and A. Reale, "Airbrush spray-coating of polymer bulk-heterojunction solar cells," *Sol. Energy Mater. Sol. Cells*, vol. 95, no. 7, pp. 1775–1778, Jul. 2011.
- [6] S.-Y. Park, Y.-J. Kang, S. Lee, D.-G. Kim, J.-K. Kim, J. H. Kim, and J.-W. Kang, "Spray-coated organic solar cells with large-area of 12.25cm²," *Sol. Energy Mater. Sol. Cells*, vol. 95, no. 3, pp. 852–855, Mar. 2011.

- [7] C. Girotto, B. P. Rand, J. Genoe, and P. Heremans, "Exploring spray coating as a deposition technique for the fabrication of solution-processed solar cells," *Sol. Energy Mater. Sol. Cells*, vol. 93, no. 4, pp. 454–458, Apr. 2009.
- [8] D. J. Vak, D. J. Vak, S. S. Kim, S. S. Kim, J. Jo, J. Jo, S. H. Oh, S. H. Oh, S. I. Na, S. I. Na, J. W. Kim, J. W. Kim, D. Y. Kim, and D. Y. Kim, "Fabrication of organic bulk heterojunction solar cells by a spray deposition method for low-cost power generation," *Appl. Phys. Lett.*, vol. 91, no. 8, p. -, 2007.
- [9] C. Girotto, B. P. Rand, J. Genoe, and P. Heremans, "Exploring spray coating as a deposition technique for the fabrication of solution-processed solar cells," *Sol. Energy Mater. Sol. Cells*, vol. 93, no. 4, pp. 454–458, Apr. 2009.
- [10] C. N. Hoth, R. Steim, P. Schilinsky, S. a. Choulis, S. F. Tedde, O. Hayden, and C. J. Brabec, "Topographical and morphological aspects of spray coated organic photovoltaics," *Org. Electron. physics, Mater. Appl.*, vol. 10, no. 4, pp. 587–593, Jul. 2009.
- [11] K. X. Steirer, J. J. Berry, M. O. Reese, M. F. a. M. van Hest, A. Miedaner, M. W. Liberatore, R. T. Collins, and D. S. Ginley, "Ultrasonically sprayed and inkjet printed thin film electrodes for organic solar cells," *Thin Solid Films*, vol. 517, no. 8, pp. 2781–2786, Feb. 2009.
- [12] S.-I. Na, B.-K. Yu, S.-S. Kim, D. Vak, T.-S. Kim, J.-S. Yeo, and D.-Y. Kim, "Fully spray-coated ITO-free organic solar cells for low-cost power generation," *Sol. Energy Mater. Sol. Cells*, vol. 94, no. 8, pp. 1333–1337, Aug. 2010.
- [13] B. K. Yu, D. Vak, J. Jo, S. I. Na, S. S. Kim, M. K. Kim, and D. Y. Kim, "Factors to be considered in bulk heterojunction polymer solar cells fabricated by the spray process," *IEEE J. Sel. Top. Quantum Electron.*, vol. 16, no. 6, pp. 1838–1846, 2010.
- [14] C. Girotto, D. Moia, B. P. Rand, and P. Heremans, "High-Performance Organic Solar Cells with Spray-Coated Hole-Transport and Active Layers," *Adv. Funct. Mater.*, vol. 21, no. 1, pp. 64–72, Jan. 2011.
- [15] W. Nie, R. C. Coffin, J. Liu, Y. Li, E. D. Peterson, C. M. MacNeill, R. E. Nofle, and D. L. Carroll, "High efficiency organic solar cells with spray coated active layers comprised of a low band gap conjugated polymer," *Appl. Phys. Lett.*, vol. 100, no. 8, p. 083301, 2012.
- [16] T. Wang, N. W. Scarratt, H. Yi, A. D. F. Dunbar, A. J. Pearson, D. C. Watters, T. S. Glen, A. C. Brook, J. Kingsley, A. R. Buckley, M. W. a Skoda, A. M. Donald, R. a L. Jones, A. Iraqi, and D. G. Lidzey, "Fabricating high performance, donor-acceptor copolymer solar cells by spray-coating in air," *Adv. Energy Mater.*, vol. 3, no. 4, pp. 505–512, Apr. 2013.

- [17] J. G. Tait, B. P. Rand, and P. Heremans, "Concurrently pumped ultrasonic spray coating for donor:acceptor and thickness optimization of organic solar cells," *Org. Electron.*, vol. 14, no. 3, pp. 1002–1008, Mar. 2013.
- [18] D. Vak, J. van Embden, W. W. H. Wong, and S. Watkins, "Optically monitored spray coating system for the controlled deposition of the photoactive layer in organic solar cells," *Appl. Phys. Lett.*, vol. 106, no. 3, p. 033302, Jan. 2015.
- [19] H. Yi, S. Al-Faifi, A. Iraqi, D. C. Watters, J. Kingsley, and D. G. Lidzey, "Carbazole and thienyl benzo[1,2,5]thiadiazole based polymers with improved open circuit voltages and processability for application in solar cells," *J. Mater. Chem.*, vol. 21, no. 35, p. 13649, 2011.
- [20] N. Blouin, A. Michaud, and M. Leclerc, "A low-bandgap poly(2,7-carbazole) derivative for use in high-performance solar cells," *Adv. Mater.*, vol. 19, no. 17, pp. 2295–2300, 2007.
- [21] K. X. Steirer, M. O. Reese, B. L. Rupert, N. Kopidakis, D. C. Olson, R. T. Collins, and D. S. Ginley, "Ultrasonic spray deposition for production of organic solar cells," *Sol. Energy Mater. Sol. Cells*, vol. 93, no. 4, pp. 447–453, Apr. 2009.
- [22] A. Reale, L. La Notte, L. Salamandra, G. Polino, G. Susanna, T. M. Brown, F. Brunetti, and a. Di Carlo, "Spray Coating for Polymer Solar Cells: An Up-to-Date Overview," *Energy Technol.*, vol. 3, pp. 385–406, 2015.
- [23] G. Namkoong, J. Kong, M. Samson, I.-W. Hwang, and K. Lee, "Active layer thickness effect on the recombination process of PCDTBT:PC71BM organic solar cells," *Org. Electron.*, vol. 14, no. 1, pp. 74–79, Jan. 2013.
- [24] P. A. Staniec, A. J. Parnell, A. D. F. Dunbar, H. Yi, A. J. Pearson, T. Wang, P. E. Hopkinson, C. Kinane, R. M. Dalgliesh, A. M. Donald, A. J. Ryan, A. Iraqi, R. A. L. Jones, and D. G. Lidzey, "The Nanoscale Morphology of a PCDTBT:PCBM Photovoltaic Blend," *Adv. Energy Mater.*, vol. 1, no. 4, pp. 499–504, Jul. 2011.
- [25] M. Campoy-Quiles, T. Ferenczi, T. Agostinelli, P. G. Etchegoin, Y. Kim, T. D. Anthopoulos, P. N. Stavrinou, D. D. C. Bradley, and J. Nelson, "Morphology evolution via self-organization and lateral and vertical diffusion in polymer:fullerene solar cell blends," *Nat. Mater.*, vol. 7, no. 2, pp. 158–164, Feb. 2008.
- [26] T. Wang, A. J. Pearson, A. D. F. Dunbar, P. A. Staniec, D. C. Watters, H. Yi, A. J. Ryan, R. A. L. Jones, A. Iraqi, and D. G. Lidzey, "Correlating Structure with Function in Thermally Annealed PCDTBT:PC70BM Photovoltaic Blends," *Adv. Funct. Mater.*, vol. 22, no. 7, pp. 1399–1408, Apr. 2012.

- [27] K. X. Steirer, M. O. Reese, B. L. Rupert, N. Kopidakis, D. C. Olson, R. T. Collins, and D. S. Ginley, "Ultrasonic spray deposition for production of organic solar cells," *Sol. Energy Mater. Sol. Cells*, vol. 93, no. 4, pp. 447–453, Apr. 2009.
- [28] V. D. Mihailetschi, P. W. M. Blom, J. C. Hummelen, and M. T. Rispen, "Cathode dependence of the open-circuit voltage of polymer:fullerene bulk heterojunction solar cells," *J. Appl. Phys.*, vol. 94, no. 10, p. 6849, 2003.
- [29] W.-I. Jeong, J. Lee, S.-Y. Park, J.-W. Kang, and J.-J. Kim, "Reduction of Collection Efficiency of Charge Carriers with Increasing Cell Size in Polymer Bulk Heterojunction Solar Cells," *Adv. Funct. Mater.*, vol. 21, no. 2, pp. 343–347, Jan. 2011.
- [30] S. Choi, W. J. Potscavage, and B. Kippelen, "Area-scaling of organic solar cells," *J. Appl. Phys.*, vol. 106, no. 5, p. 054507, 2009.
- [31] A. Armin, M. Hambsch, P. Wolfers, H. Jin, J. Li, Z. Shi, P. L. Burn, and P. Meredith, "Efficient, Large Area, and Thick Junction Polymer Solar Cells with Balanced Mobilities and Low Defect Densities," *Adv. Energy Mater.*, vol. 5, no. 3, p. n/a–n/a, Feb. 2015.

Chapter 5 Spray Coating and Scale-up of Vanadium Oxide and Molybdenum Oxide as Hole Transport Layers

The previous chapter details the spray coating of the photoactive layer in an organic photovoltaic device. The remaining spin cast layer in the device stack is the hole transport layer (HTL). In this chapter, both vanadium oxide and molybdenum oxide hole transport layers are spray cast. Films and devices are fabricated and characterised and a deposition process is optimised. Device sizes are then partially scaled up to investigate the feasibility of larger scale production.

5.1 Introduction

Vanadium oxide (V_2O_x) and molybdenum oxide (MoO_x) have previously been shown, along with other metal oxides such as WO_x , to be effective hole transport layers in organic photovoltaic devices [1][2].

In a bulk heterojunction OPV of standard architecture, the hole transport layer lies between the transparent anode (usually ITO) and the organic donor material as shown in Figure 5-1. HTL layers used in this architecture must be thick enough for their hole transport characteristics to be effective, yet thin enough to allow transmission of light through to the active layer. The balance between these properties inside the cell is important, as a reduction in hole transport or light penetration both result in reduced photocurrent generation and therefore a reduced power conversion efficiency.

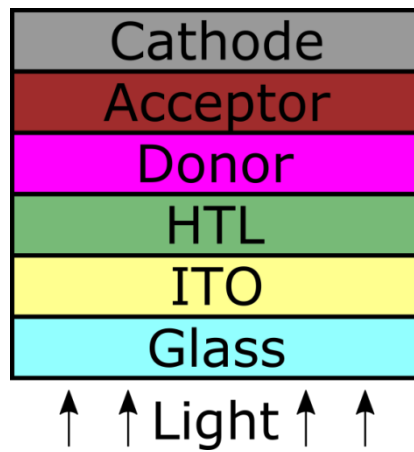


Figure 5-1: Device architecture in a standard bulk heterojunction OPV device.

The active layers used in this work are the donor material poly[9-(heptadecan-9-yl)-9H-carbazole-2,7-diyl-alt-(40,70-di-2-thienyl-20,10,30-benzothiadiazole)-5,5-diyl] (PCDTBT) and the fullerene derivative acceptor PC₇₀BM. V₂O_x and MoO_x have work functions of 5.6 eV [3] and 5.4 eV respectively, which align well with the HOMO level of a PCDTBT donor (5.35 eV) [4].

In this chapter, a solution processable form of vanadium oxide is spray cast as part of the device fabrication process. The spray coating process is optimised via deposition parameters and processing conditions. The vanadium oxide layers are then incorporated into organic photovoltaic devices and characterised.

5.2 Chapter Summary

An ultrasonic spray coating process is optimised for the deposition of solution processed metal oxide layers vanadium oxide and molybdenum oxide. Ink formulation and deposition parameters are explored, including: solvent blend ratios, spray speed, solution concentration and layer thickness. PCDTBT:PC₇₀BM deposition parameters developed in Chapter 4 are then tuned for deposition onto the spray-cast metal oxide films. An optimised deposition process is used to fabricate devices on both small-area devices and performance compared with spin cast PEDOT:PSS. Large-area device architectures are then fabricated using

optimised deposition parameters and the effect of scale-up on performance is discussed.

5.3 Device Preparation

The vertical device architecture used in this chapter is displayed in Figure 5-1a. The materials and thicknesses of the materials in the stack are as follows: ITO/HTL/PCDTBT:PC₇₀BM/Ca (5 nm)/Al (100 nm), where the hole transport layer (HTL) is either V₂O_x or MoO_x. The thickness of the HTL and PCDTBT:PC₇₀BM layers will vary throughout the chapter as they are optimised for use with one another. The photoactive layer was spray cast from a chlorobenzene solution with a concentration of 8 mg ml⁻¹ onto a substrate held at 40°C. The other stages of device fabrication are described in Chapter 3. Two device architectures are used in this chapter, shown in Figure 5-2(b) and (c). The six pixel substrate shown in (b) is used for the optimisation stages of this chapter, with the larger area 36 pixel (c) employed during scale up in sections 4.7 and 5.9. A discussion on these device architectures can be found in Chapter 4.

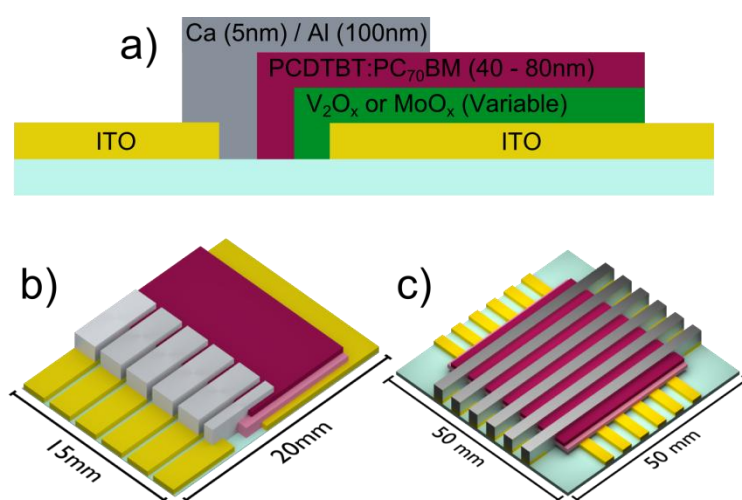


Figure 5-2: Schematics showing a) vertical device structure and device architectures for b) a small 6 pixel substrate, b) large 36 pixel substrate and d) a large single pixel substrate.

5.4 Vanadium Oxide in Solution

Vanadium oxide in its basic form is not easily solution processable using common solvents. This issue is overcome via the addition of side chains to the Oxygen atoms which increase solubility, as shown in Figure 5-3. The resultant precursor material is called vanadium oxytriisopropoxide. This material was sourced from Sigma Aldrich and used as received.

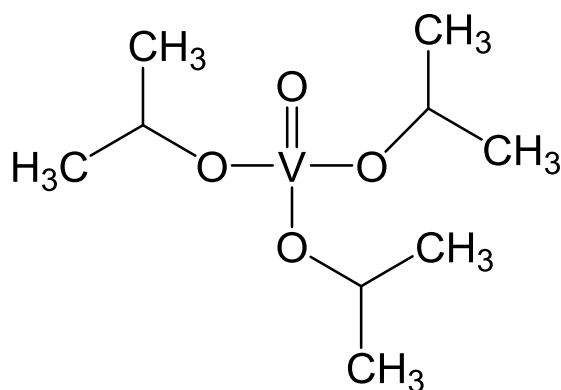
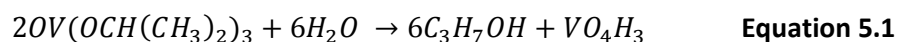


Figure 5-3: Vanadium oxytriisopropoxide

When exposed to air during the deposition, a hydrolysis reaction occurs as described by Equation 5.1 and 5.2.



The solvent used in this investigation was isopropyl alcohol (IPA) as it dissolves the vanadium oxytriisopropoxide well, is relatively non-toxic and is a common solvent used in industrial applications. IPA has excellent wetting properties when deposited on to an ITO anode: the first layer in an OPV stack.

5.5 Spray Speed and Film Thickness

To investigate the effect of spray parameters on device performance, it is important to determine final film thickness. The lateral velocity of the spray head determines the volume of solution deposited and therefore has a large impact on the thickness

of the film upon drying. vanadium films were sprayed at several speeds on to silicon substrates and film thickness was measured using an optical ellipsometer. Figure 5-4 shows the resultant data, wherein film roughness is used as thickness error. In Chapter 4, film thickness appeared to be inversely proportion to spray speed as described by the equation:

$$\tau = \frac{A}{\text{spray speed}} \quad \text{Equation 5.3}$$

where τ is film thickness and A is a constant dependent on several factors involved with the spray coating process (e.g. spray height, deposition pressure, solution concentration etc.). The value of A in the fit of Figure 5-4 is calculated to be 858 nm mm s⁻¹, or 868 $\mu\text{m}^2 \text{s}^{-1}$. This empirically derived value is used for the calculation of vanadium film thickness in this chapter.

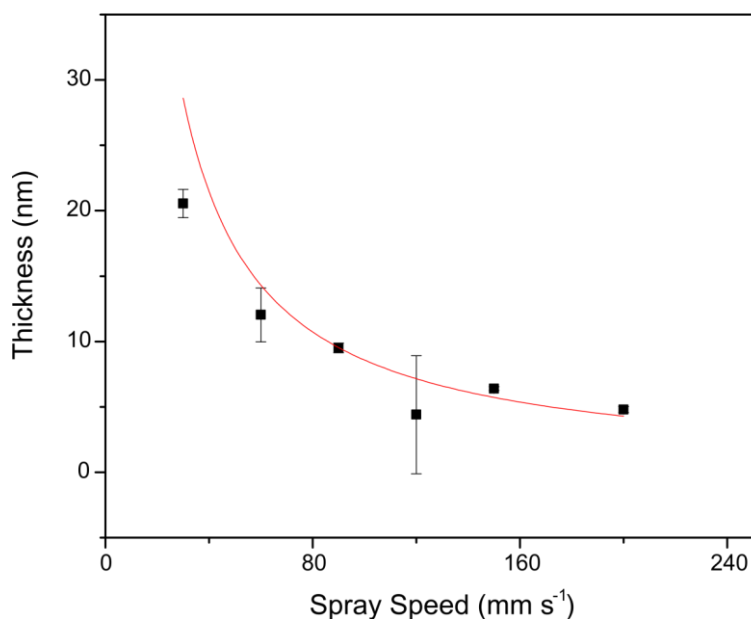


Figure 5-4: Dependence of V2Ox film thickness on lateral spray velocity. Films were spray cast at 20°C from an IPA solution of concentration 1 mg ml⁻¹ at a spray height of 35 mm.

5.5.1 Transmission of Vanadium Oxide Films

Absorption measurements were performed in order to determine the transmission of spray cast V₂O_x films. The transmission of V₂O_x films with varying thickness is shown in Figure 5-5.

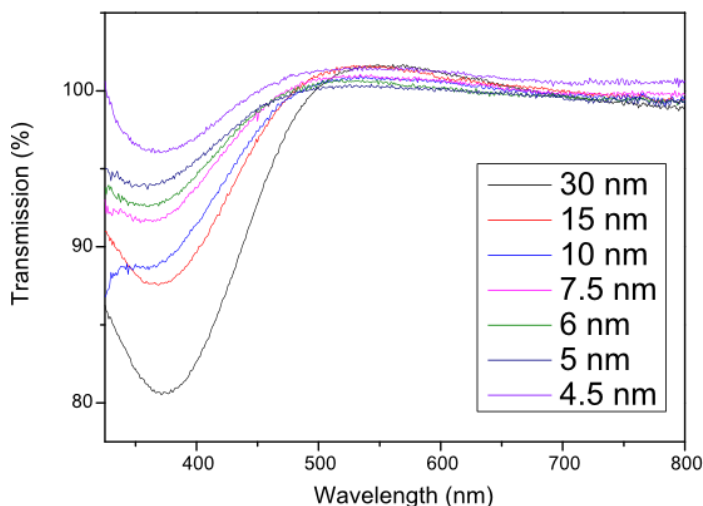


Figure 5-5: Transmission of spray cast V₂O_x films of varying thickness. Films were spray cast at 20°C from an IPA solution of concentration 1 mg ml⁻¹ at a spray height of 35 mm.

After a peak absorption at ~375 nm, film transmission increases to 100% in all film thicknesses at around 500 nm. The band gap of vanadium oxide is around 2.42 eV, equivalent to 512 nm, which agrees well with the increased transmission [5]. High transmission is a preferable characteristic of a hole transport layer, as light must pass through it to reach the active layer of the device stack. High transmission above 500 nm is also beneficial in the device architecture used in this work, as the donor material PCDTBT has a narrow band gap [6], and will therefore absorb the lower energy photons that pass through the V₂O_x layer.

5.5.2 Spray Speed

A V₂O_x layer thickness of less than 10 nm is preferable for efficient hole transport, therefore a low solution concentration is chosen for initial device fabrication [3]. Figure 5-6 shows metrics of devices fabricated using several lateral spray velocities

from a V_2O_x solution concentration of 0.25mg/ml and a deposition temperature of 20°C . This low deposition temperature is made possible by using IPA as a solvent, which has a boiling point of 82.6°C and a low surface tension of 23 mN m^{-1} [7]. This allows the solvent to quickly spread and then evaporate without causing the 'picture framing' seen in Chapter 4. There is a limit to this however, and a film of low enough volume may not achieve full coverage. Because of this effective wetting, all V_2O_x films in this chapter were deposited at 20°C .

As with the devices in Chapter 4, twelve devices were fabricated over two substrates for each data point, and the top 50% were used in the data analysis. While some of the fabricated devices perform well, there is a large inconsistency between devices, and even individual pixels. This indicates a non-uniform layer across the cell. A low solution concentration might not form a continuous layer, giving rise to such variation.

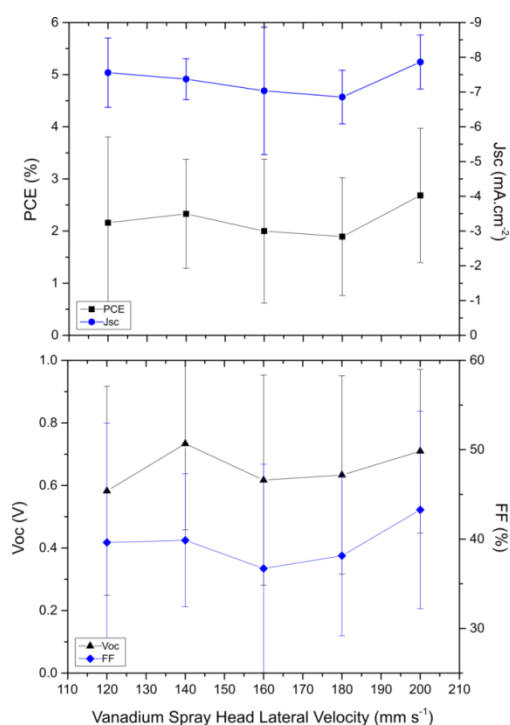


Figure 5-6: The effect of spray-head lateral velocity on device parameters for a solution with concentration 0.25mg.ml^{-1} . Films were spray cast at a spray height of 35 mm.

If the non-uniformity is due to film coverage, then increasing the film thickness may improve performance. Film thickness can be increased via solution concentration, spray speed, spray height and pressure. The latter three parameters change the volume of solvent deposited onto the substrate. This will increase the final film thickness, however drying kinetics will also be changed and final film uniformity may be affected. A more effective method for comparing film thickness performance is to increase the solution concentration. Using the same spraying parameters will not affect the solution volume and drying time, just the dry film thickness. Solution concentration is raised to 1 mg ml^{-1} in order to increase final film thickness and investigate the effect on device performance. As the solution concentration is four times greater, similar spray parameters will not provide similar final film thicknesses. The range of spray speeds was therefore increased in order to include speeds four times greater than previously. Final device metrics are shown in Figure 5-7.

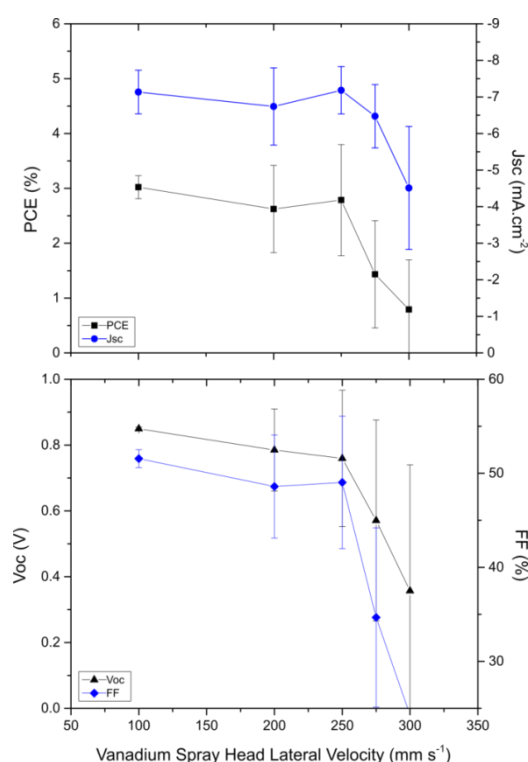


Figure 5-7: Device metrics showing the affect if lateral spray speed on device performance for solution concentration of 1 mg ml^{-1} . Films were spray cast at a spray height of 35 mm.

There is a clear drop in all four metrics as spray speeds are increased past 200 mm s⁻¹. The spread in device efficiencies is also much larger at higher spray speeds, indicating incomplete film coverage over the substrate surface. Devices with films sprayed at 100 mm s⁻¹ had a much smaller spread in performance, implying greatly increased coverage over the substrate.

5.5.3 Effect of Film Thickness on Device Performance

A second set of devices with even thicker vanadium layers were fabricated using the same deposition parameters apart from spray speed. These are shown in Figure 5-8 where they are compared with the first devices from Figure 5-7, which have been re-plotted in Figure 5-8 using film thickness as the x axis instead of spray speed.

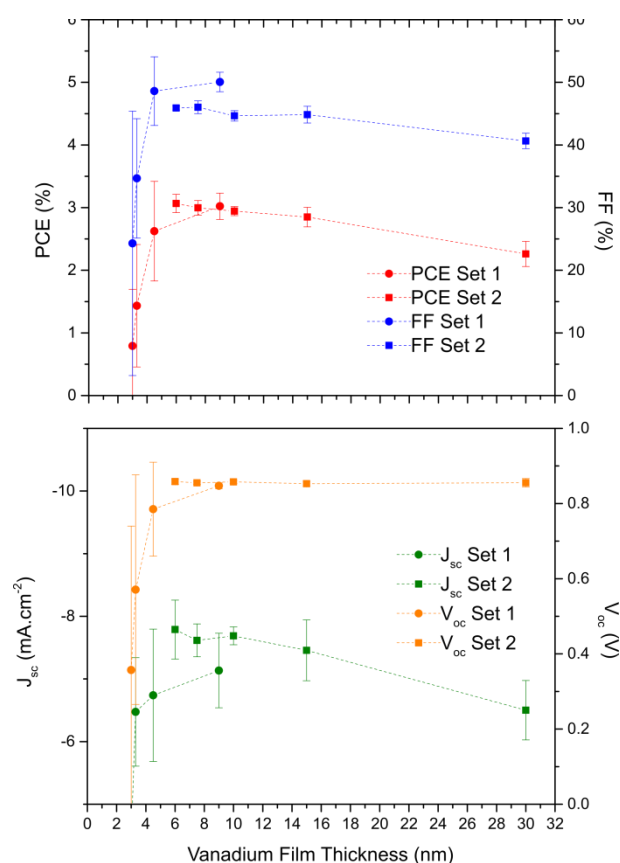


Figure 5-8: Device metrics for OPVs fabricated with spray cast V₂O_x layers of varying thickness. Solution concentration was 1 mg ml⁻¹. Films were spray cast at a spray height of 35 mm.

There is a clear increase in performance of devices fabricated with thicker V_2O_x , achieving a maximum PCE of 3.30% at a thickness of 6 nm. Thinner films than 6 nm cause a large variation between devices and all device metrics are lower. For devices with thicker V_2O_x layers, there is a decrease in average short circuit current density from 7.46 to 6.5 mA cm^{-2} between films of 6 nm and 30 nm respectively. Open circuit voltage however remains at ~ 0.88 for higher thicknesses. The reduction in device performance could therefore be attributed to poorer hole transport through the thicker V_2O_x layer leading to a decrease in holes reaching the anode and therefore a decrease in extracted current. The absorption of the 30 nm thick layer in Figure 5-5 is much greater than the thinner layers and extends over a larger range of wavelengths. The optical transmissivity of the layer could therefore also be causing a reduction in light reaching the active layer. This is in agreement with Zilberberg's findings [3], wherein J_{sc} decreased due to increased absorption as a V_2O_5 hole transport layer was increased in thickness from 10 to 45 nm.

5.6 Surface Roughness

High film uniformity is desirable as manufacturing of solar cells would require repeatable results between devices. The optimised vanadium oxide layer is very thin, therefore a rough surface could create voids in the film and reduce its performance. Furthermore the scalability of the process is dependent on repeatability, as manufacturing requires similar performance between device batches. Atomic force microscopy (AFM) was used to investigate the surface roughness of spray cast films of varying thickness. Figure 5-9 shows films of thickness a) 30 nm, b) 15 nm and c) 6 nm and an ITO substrate d).

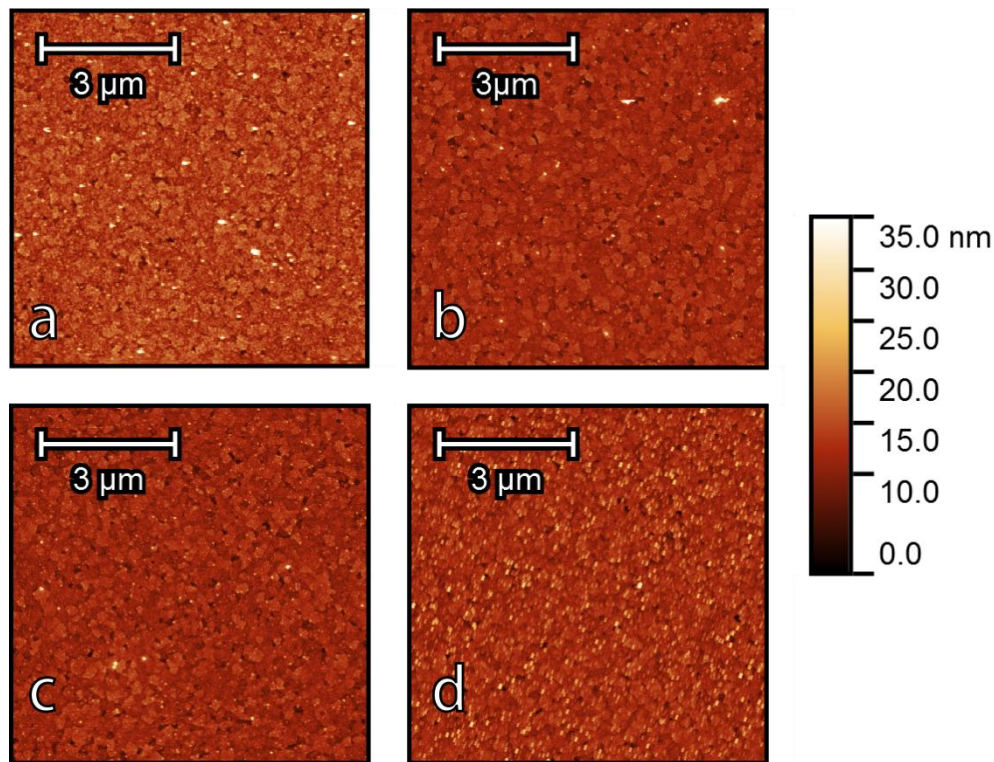


Figure 5-9: Atomic force microscopy spray cast vanadium oxide films of thickness a) 30 nm, b) 15 nm and c) 6 nm. An ITO substrate is also shown in d). Films were spray cast at 20°C from an IPA solution of concentration 1 mg ml⁻¹ at a spray height of 35 mm.

The roughness of each film is listed in Table 5-1. Even in films as thick as 30 nm, there is little variation in film thickness. Unlike PEDOT:PSS which planarises the ITO surface [8], V₂O_x appears to conform to the ITO surface topography, even at higher thicknesses. This results in a final film roughness that directly relates to the roughness of the substrate on to which it is cast.

Vanadium Oxide Film Thickness (nm)	RMS Roughness (nm)
30	2.81
16	2.05
6	2.08
ITO	2.65

Table 5-1: Roughness of vanadium oxide films at varying thickness, measured via atomic force microscopy

At thicknesses lower than 6 nm, the V₂O_x film will be unlikely to achieve full coverage, as the ITO will puncture the film in some regions. This explains the

reduction in all device characteristics shown at very low film thicknesses in Figure 5-8. Optimum film thickness is therefore determined to be ~6 nm, in agreement with literature. The optimised processing parameters are used for the investigations in the further sections of this chapter.

5.7 PCDTBT:PC70BM

5.7.1 Film Thickness

A suitable processing method for the V_2O_x must be accompanied by an effective photoactive layer. The spray speed and therefore thickness of PCDTBT:PC₇₀BM must be optimised for this system to increase the performance of spray coated devices. The V_2O_x layer was spray cast using the conditions optimised earlier in this chapter, namely a concentration of 1mg ml and a spray speed of 150 mm s⁻¹ to achieve a final film thickness of 6 nm. The effect of varying PCDTBT:PC₇₀BM film thickness on device performance is shown in Figure 5-10.

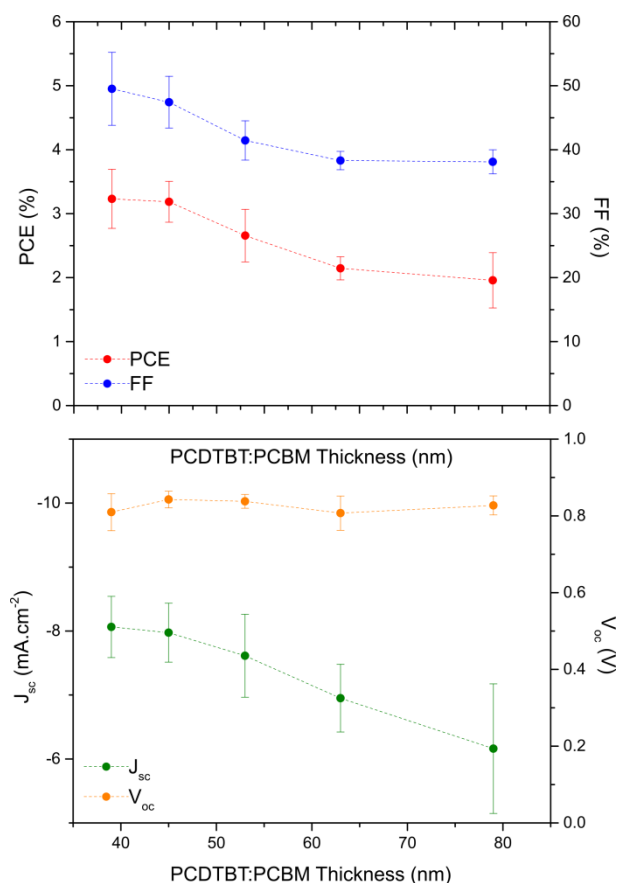


Figure 5-10: The variation in device performance with spray cast PCDTBT:PC₇₀BM layer thickness. V₂O_x films were spray cast at 20°C from an IPA solution of concentration 1 mg ml⁻¹ at a spray speed of 150 mm s⁻¹. Both V₂O_x and PCDTBT:PC₇₀BM films were spray cast at a height of 35 mm.

The short circuit current density decreases with increasing film thickness from -8.06 mA cm⁻² with a 40nm film to -6.16 mA cm⁻² at 85 nm. This result is unexpected, as J_{sc} values in Chapter 4 of above 8.5 mA cm⁻² were achieved for active layer thicknesses of between 45 and 60 nm. There is also a large loss in fill factor, indicating possible shorts in the film or increased series resistance. PCDTBT has relatively low charge mobility in thicker films therefore this could contribute to this loss is, however this does not account for such a large decrease in performance [9].

5.7.2 Comparison with PEDOT:PSS

PEDOT:PSS was used as a HTL in the previous chapter, wherein PCDTBT:PCBM was spray cast on to a spin cast PEDOT:PSS film, achieving power conversion efficiencies above 4%. In order to determine the effectiveness of the optimised spray cast V₂O_x,

a batch of devices was fabricated by spin casting PEDOT:PSS and spray casting V_2O_x . A PCDTBT:PC₇₀BM layer was then spray cast on to both types of HTL at various spray speeds. Device performance is very similar between the two architectures as shown in Figure 5-11.

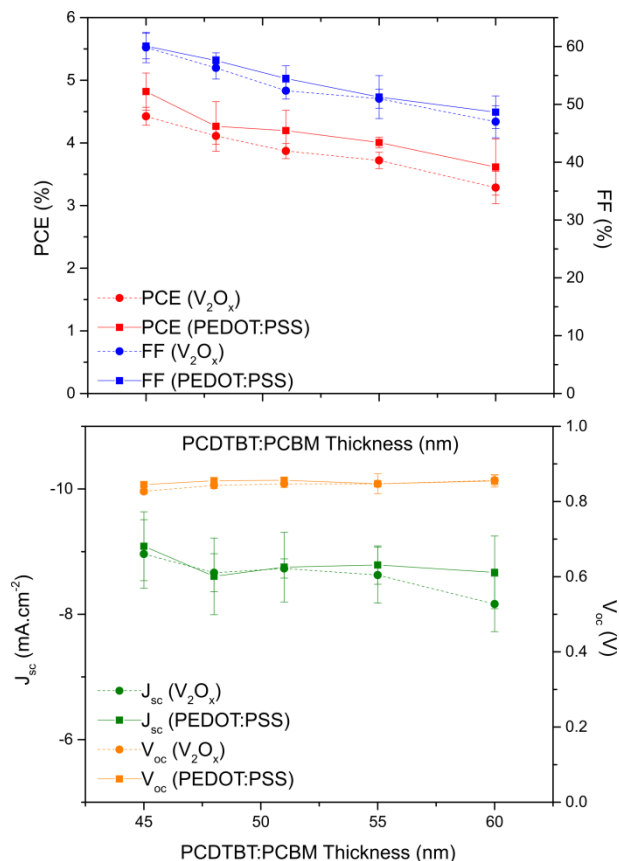


Figure 5-11: A comparison between devices fabricated with spray cast V_2O_x and spin cast PEDOT:PSS hole transport layers. A PCDTBT:PC₇₀BM photoactive layer was spray cast in both cases.

A maximum PCE of 4.58 % for the V_2O_x devices compares well with a maximum of 4.82 % for the spin cast PEDOT:PSS devices. The V_2O_x devices performed significantly better during this device run, despite using the same deposition parameters as that of Figure 5-10. Averaged J-V data for the 45 nm devices of Run 1 and Run 2 are shown in Figure Figure 5-12.

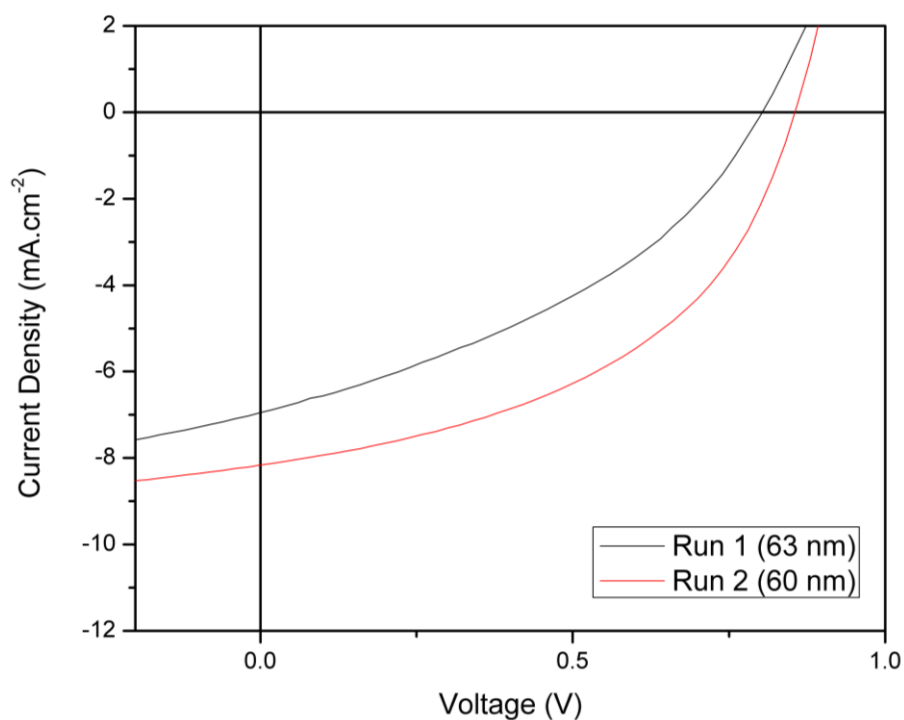


Figure 5-12: Averaged J-V data for 60 and 63 nm devices from Run 1 and Run 2 respectively.

The fill factor and J_{sc} appear to be the most significant differences between the devices, producing a loss in performance. Series and shunt resistances were calculated from the J-V data and are shown in Table 5-2. The series resistance of the Run 1 device is almost double that of the Run 2 device.

Run number	R_{Shunt} (Ω)	R_{Series} (Ω)
1	271	39.78
2	461	20.82

Table 5-2: Roughness of vanadium oxide films at varying thickness, measured via atomic force microscopy

The variation between runs when using the same deposition parameters implies an inherent uncertainty in the spray coating and device fabrication process. Factors including humidity, ambient temperature and even spray pipe cleanliness are all difficult to control with a small scale research set up. When scaling up to an industrial process, there would be more control over the manufacturing environment and thus repeatability would most likely improve.

5.8 Scale Up

To investigate the scalability of the spray coating process, a larger device was fabricated using the 36 pixels architecture shown in Figure 5-2(c). Film quality over the surface of the large ITO substrate was similar to that of the small substrates. The IPA based solution spread well and there were no visible defects in the film. The full dataset of the 36 pixels is displayed in Figure 5-13, showing a relatively high yield of 86% with five outliers. In previous sections, the optimisation of a recipe was the goal, therefore only the top 50% of devices were studied. During scale up however, consistency and yield are potentially as important as overall performance, therefore all pixels on the large device are included. The outlying pixels here are not like the poorer performing devices discussed in previous chapters, as all five outliers appear to be primarily caused by a large reduction in V_{oc} and not J_{sc} or FF. These are considered 'dead' pixels, and would normally be discounted in the lower 50% of devices.

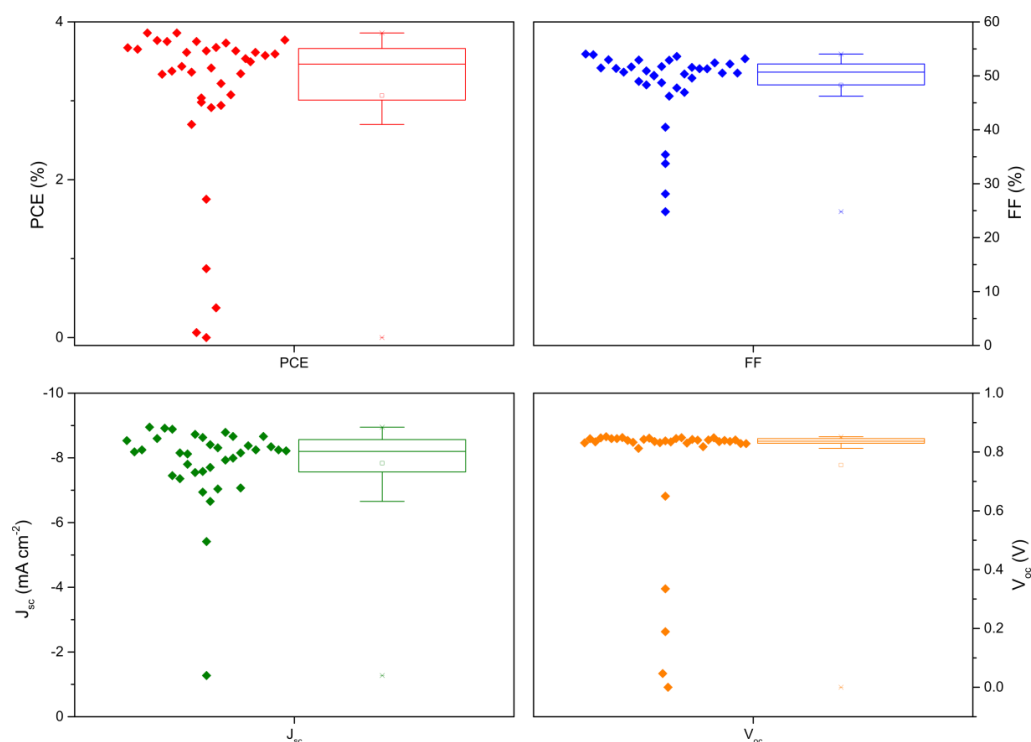


Figure 5-13: Distribution of device metrics for a 36 pixel device fabricated via spray casting of both a vanadium oxide hole transport layer and a PCDTBT:PC₇₀BM photoactive layer.

This high yield is promising as despite the run-to-run variation discussed in section 5.8, consistency of devices over a single large substrate demonstrates that the technology can be effective in these circumstances.

A manuscript is in preparation for the work on spray coating and scale up of vanadium oxide in this chapter.

5.9 Molybdenum Oxide in Solution

As is the case with vanadium oxide, the molybdenum oxide used in this work is deposited as a precursor, namely ammonium molybdate tetrahydrate. This material was sourced from Sigma Aldrich and used as received. This precursor dissolves well in DI water, which is promising for non-toxic processing. Unfortunately water has a high surface tension and spray coating the solution is not possible as it causes dewetting across a substrate. In order to reduce the surface tension of the ink and allow it to flow across the substrate surface, a new ink formulation was required. A secondary solvent must be miscible with water, have a lower surface tension to aid wetting and have a similar boiling point to water so that it does not evaporate too quickly. Acetonitrile was chosen for this purpose as it has a surface tension of 29 mN m^{-1} , which is much lower than that of water (72.8 mN m^{-1}). It has a boiling point of 82°C , slightly less than that of water[7]. The ratio of acetonitrile to water was steadily increased until the molybdenum tetrahydrate began to drop out of solution. At this point, the ratio was reduced again and a final ratio of 2:3 (DI water : Acetonitrile) was chosen. The optimisation of molybdenum oxide for the small-area device architecture was investigated in collaboration with Jonathan Griffin.

5.10 Scale up Of Spray Cast Molybdenum Oxide

Final material solution concentration was 6 mg ml^{-1} and the solution was sprayed at a speed of 60 mm s^{-1} onto ITO substrates held at a temperature of 60°C to produce a MoOx layer with a thickness of 13 nm. Upon film deposition, substrates were then annealed on a separate hot plate at 350°C to complete the decomposition of the precursor material into molybdenum oxide [10]. A PCDTBT:PCBM layer was then

spray cast on to the MoOx from a solution concentration of 4 mg ml⁻¹ at a spray speed of 80 mms⁻¹ and a height of 35 mm to produce a film thickness of 60 nm. Full devices were then fabricated as described in section 5.3. Performance characteristics are displayed in Table 5-3.

PCE (%)	Max PCE (%)	FF (%)	J _{sc} (mA cm ⁻²)	V _{oc} (V)
4.0 ± 0.3	4.4	50.9 ± 1.3	-7.37 ± 2.16	0.88 ± 0.01

Table 5-3: Performance characteristics of OPV devices fabricated via spray casting of both MoOx hole transport layers and PCDTBT:PC₇₀BM[photoactive layers.

This work was published in ref [11].

This fabrication process was repeated using the large 36 pixel architecture as shown in Figure 5-2(c). The spray height was changed to 70 mms⁻¹ and the spray speed was reduced to 40 mms⁻¹ to achieve similar film thicknesses. Performance characteristics of all 36 pixels are displayed in Figure 5-14. There is high yield of 89%, with only 4 outliers.

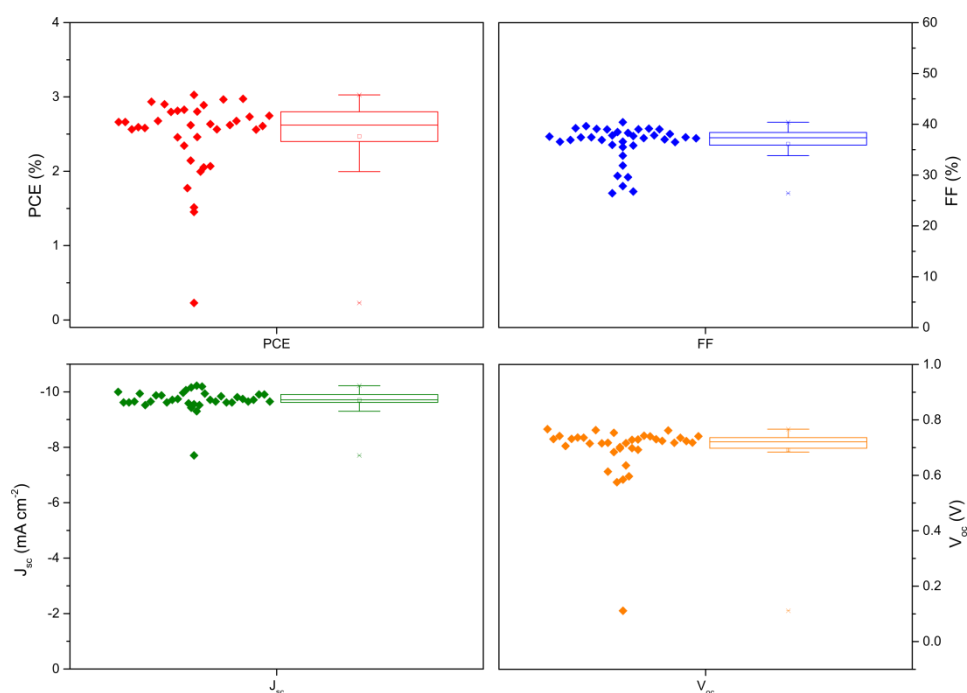


Figure 5-14: Performance characteristics of a 36 pixel device fabricated via spray casting both a molybdenum oxide and a PCDTBT:PC₇₀BM photoactive layer.

The performance of spray cast MoO_x devices is slightly poorer than the V₂O_x devices when scaled up using the 36 pixel device architecture. They both perform relatively consistently over the substrate area, however they achieve power conversion efficiencies lower than what is possible with this material system. This implies that further optimisation is required if these hole transport layers are to be a viable alternative to PEDOT:PSS during large scale fabrication.

5.11 Conclusion

A spray coating process has been optimised for the metal oxide hole transport layer vanadium oxide. Small-area devices were fabricated and performances matched those of devices with spin cast PEDOT:PSS hole transport layers of around 4.6% PCE. Film uniformity was characterised via atomic force microscopy, showing that the vanadium oxide film conforms to the surface morphology of the ITO substrate on to which it is cast. A large 36 pixel device was then fabricated, providing a high pixel yield of 86% and indicating that the film remains relatively uniform when spray-casting over a larger area. Another metal oxide layer, molybdenum oxide was also spray cast on small and large area devices. This too performed well over a larger surface area, with a high pixel yield of 89%.

5.12 References

- [1] Y.-M. Chang and J.-M. Ding, "High efficiency inverted polymer solar cells with the sol-gel derived vanadium oxide interlayer," *Thin Solid Films*, vol. 520, no. 16, pp. 5400–5404, 2012.
- [2] H. Choi, B. Kim, M. J. Ko, D.-K. Lee, H. Kim, S. H. Kim, and K. Kim, "Solution processed WO₃ layer for the replacement of PEDOT:PSS layer in organic photovoltaic cells," *Org. Electron.*, vol. 13, no. 6, pp. 959–968, Jun. 2012.
- [3] K. Zilberberg, S. Trost, H. Schmidt, and T. Riedl, "Solution Processed Vanadium Pentoxide as Charge Extraction Layer for Organic Solar Cells," *Adv. Energy Mater.*, vol. 1, no. 3, pp. 377–381, May 2011.
- [4] H. Yi, S. Al-Faifi, A. Iraqi, D. C. Watters, J. Kingsley, and D. G. Lidzey, "Carbazole and thienyl benzo[1,2,5]thiadiazole based polymers with

improved open circuit voltages and processability for application in solar cells," *J. Mater. Chem.*, vol. 21, no. 35, p. 13649, Aug. 2011.

- [5] C. P. Chen, Y. D. Chen, and S. C. Chuang, "High-performance and highly durable inverted organic photovoltaics embedding solution-processable vanadium oxides as an interfacial hole-transporting layer," *Adv. Mater.*, vol. 23, no. 33, pp. 3859–3863, 2011.
- [6] K. K. H. Chan, S. W. Tsang, H. K. H. Lee, F. So, and S. K. So, "Charge injection and transport studies of poly(2,7-carbazole) copolymer PCDTBT and their relationship to solar cell performance," *Org. Electron.*, vol. 13, no. 5, pp. 850–855, May 2012.
- [7] D. R. Lide, "CRC Handbook of Chemistry and Physics, 84th Edition, 2003–2004," *Handb. Chem. Phys.*, vol. 53, p. 2616, 2003.
- [8] P. Peumans and S. R. Forrest, "Very-high-efficiency double-heterostructure copper phthalocyanine/C[₆₀] photovoltaic cells," *Appl. Phys. Lett.*, vol. 79, no. 1, p. 126, 2001.
- [9] T. M. Clarke, J. Peet, A. Nattestad, N. Drolet, G. Dennler, C. Lungenschmied, M. Leclerc, and A. J. Mozer, "Charge carrier mobility, bimolecular recombination and trapping in polycarbazole copolymer:fullerene (PCDTBT:PCBM) bulk heterojunction solar cells," *Org. Electron.*, vol. 13, no. 11, pp. 2639–2646, Nov. 2012.
- [10] J. Meyer, S. Hamwi, M. Kröger, W. Kowalsky, T. Riedl, and A. Kahn, "Transition Metal Oxides for Organic Electronics: Energetics, Device Physics and Applications," *Adv. Mater.*, vol. 24, no. 40, pp. 5408–5427, Oct. 2012.
- [11] J. Griffin, A. J. Pearson, N. W. Scarratt, T. Wang, D. G. Lidzey, and A. R. Buckley, "Organic photovoltaic devices incorporating a molybdenum oxide hole-extraction layer deposited by spray-coating from an ammonium molybdate tetrahydrate precursor," *Org. Electron.*, vol. 15, no. 3, pp. 692–700, Mar. 2014.

Chapter 6 Spray Coating and Scale Up of PEDOT:PSS as a Hole Transport Layer

The previous chapter demonstrated the fabrication of OPV devices wherein both a vanadium oxide hole transport layer and a PCDTBT:PC₇₀BM photoactive layer were spray-cast. Vanadium oxide is an effective hole transport layer, however it has been shown to have a much shorter lifetime than the widely used PEDOT:PSS [1].

6.1 Introduction

PEDOT:PSS is undoubtedly the most popular hole transport material within the field of organic photovoltaic's, and it has been used in a large variety of studies. PEDOT:PSS is typically spin-cast on to a transparent anode material such as indium tin oxide (ITO), however spin coating not a scalable process and alternative deposition techniques must be explored. As discussed in the Background Theory chapter of this thesis, PEDOT:PSS has been deposited via several scalable techniques already. Studies involving spray coating of the material are limited however. PEDOT:PSS is typically supplied in an aqueous medium characterised by a high surface tension. This is not an issue when spin coating layers, as shear forces acting on the wet film force it to spread over the surface of a substrate. This does pose a problem for spray coating however, as droplets must spread and merge without external lateral force acting upon them. Figure 6-1 shows an droplet of an aqueous PEDOT:PSS solution on an ITO substrate in ambient conditions. After initial settling, the droplet reached equilibrium with the surface at a high contact angle of 22°. During spray deposition, droplets of this solution will not spread across a surface and merge into a uniform film. This high contact angle must therefore be overcome via ink formulation and deposition parameters.

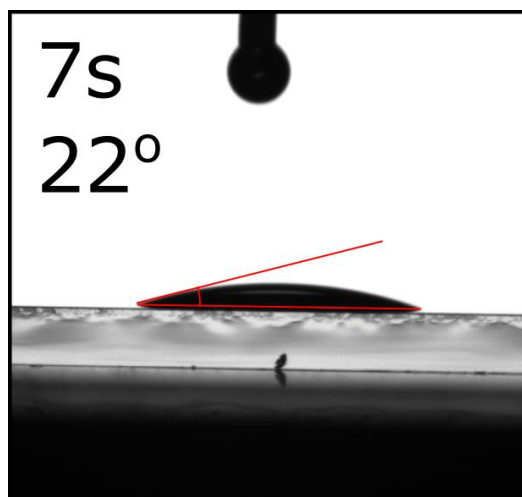


Figure 6-1: A contact angle image taken 7 seconds after PEDOT:PSS was dropped onto an ITO substrate. The droplet had a high contact angle and did not wet well to the surface.

There have been a limited number of successful attempts at spray coating PEDOT:PSS in the past, as detailed in Table 6-1. The aqueous nature of the PEDOT:PSS ink poses a difficulty for spray casting, and many of the reported films have coffee rings after drying due to poor film wetting.

Spray Technique	PCE (%)	Pixel Area (mm ²)	Sprayed HTL	Sprayed Photoactive Layer	Citation
Airbrush	2.7	20	PEDOT:PSS	P3HT:PC ₆₁ BM	Hoth 2009[2]
Ultrasonic	3.5	-	PEDOT:PSS	P3HT:PC ₆₁ BM	Steirer 2009[3]
Airbrush	2.17	4.66	PEDOT:PSS	P3HT:PC ₆₁ BM	Na 2010[4]
Ultrasonic	3.75	3	PEDOT:PSS	P3HT:PC ₆₁ BM	Giroto 2011[5]

Table 6-1: A literature review of spray-cast PEDOT:PSS in OPV devices.

6.2 Chapter Summary

An ultrasonic spray coating process is optimised for the deposition of PEDOT:PSS hole transport layers. Ink formulation and deposition parameters are explored and an optimised deposition process is used to fabricate devices on both small-area and large-area device architectures. PCDTBT:PC₇₀BM and PBDDTT-EFT:PC₇₀BM photoactive layers are then spray-cast onto the optimised PEDOT:PSS layer. The effect of scale-up on performance is discussed. Film uniformity is characterised via atomic force microscopy, and light beam induced current mapping

6.3 IPA As a Wetting Agent

In order to reduce the contact angle of the solution and increase wetting to the substrate surface, the solution was mixed with isopropyl alcohol (IPA) at a ratio of 2:8. Figure 6-2 displays contact angle as a function of time for the PEDOT:PSS ink and a solution of PEDOT:PSS and IPA. The IPA clearly reduces the contact angle and wettability of the solution, quickly spreading over the surface.

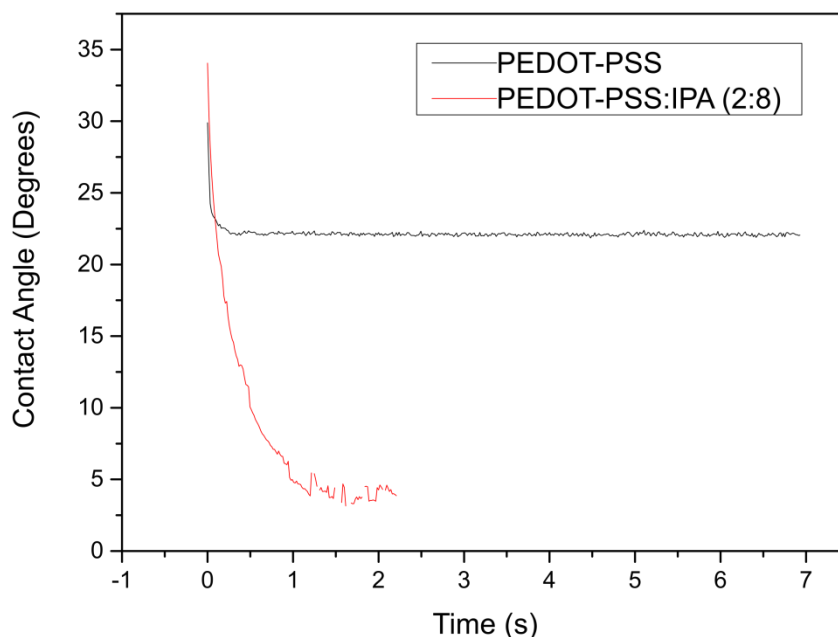


Figure 6-2: Contact angle measurements on ITO of PEDOT:PSS and a mixture of PEDOT:PSS with IPA at a ratio of 2:8. IPA dramatically decreases the contact angle of the solution and the droplet spreads rapidly over the ITO surface.

A single droplet of the mixed solvent ink covered an entire substrate surface (300 mm²) within 2 seconds of contact. This means that coffee rings are less likely to occur, as the droplets will likely spread and merge before drying. To investigate the use of this blend during device fabrication, the 2:8 ratio ink was spray-cast on to ITO substrates held at a temperature of 20°C. While initial wetting was much improved with the addition of IPA to the spray coating process, the films had large inconsistencies in surface coverage upon drying. IPA evaporates quickly, leaving a thin film of water. The solution then dewets before drying, creating holes in the film.

6.4 Ethyl Glycol as a Binding Agent

To solve this problem, a small amount of Ethylene Glycol (EG) was added to the solution at a ratio of PEDOT:PSS, IPA and EG of 2:7:1. EG has a much higher boiling point (197°C) than water (100°C) and IPA (82.6°C) [6]. Once the film has spread during the initial contact with the substrate, the IPA evaporates quickly. This leaves a thin film of EG and water containing the PEDOT:PSS material. The substrate is then transferred to a hot plate at 120°C, at which point the remaining water quickly evaporates. Ethylene glycol has a lower surface tension (47.7 mN m⁻¹) than water (72.8 mN m⁻¹) at 20°C, therefore it does not dewet as readily and keeps the spread PEDOT:PSS material in a single film. The EG then evaporates, leaving a continuous PEDOT:PSS film. A problem with this process is that during the hand-held transfer process, the EG can flow around the surface if the substrate is not held at a flat enough angle. In a real industrial setting, the substrate would be transferred from one annealing stage to another by mechanical means, therefore this would be less of a problem. The spreading process of a droplet of the 2:7:1 solution is shown in Figure 6-3. The droplet wet quickly to the surface, even with the presence of the higher surface tension EG. After three seconds, the droplet is too flat to achieve an accurate contact angle measurement with the optical tensiometer. After four seconds, it is not visible as it has flattened to the surface of the substrate.

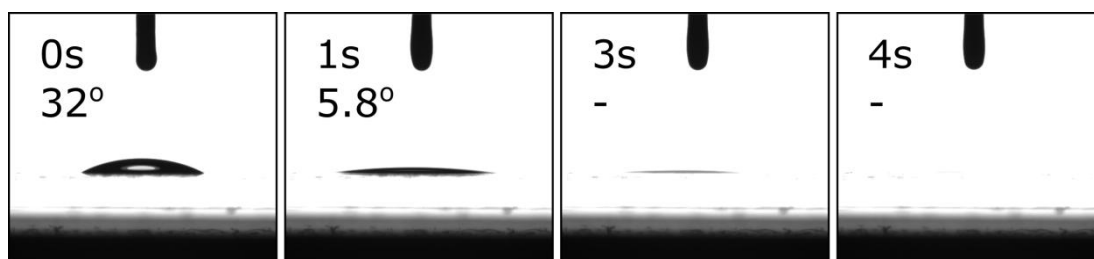


Figure 6-3: Contact angle images for an optimised PEDOT:PSS ink dropped on to an ITO substrate. The ink consisted of PEDOT:PSS, IPA and EG in a ratio of 2:7:1.

6.5 Device Preparation

The vertical device architecture used in this chapter is the same as Chapter 4, as displayed in Figure 6-4(a). The small six pixel architecture in (b) is once again used for the optimisation of the spray-cast film, with a large 36 pixel (c) substrate and large four pixel in (d) used for scale up in section 6.9. Substrate areas are 3 cm^2 and 25 cm^2 for the small and large substrates respectively. Pixel sizes are defined by the overlap of the ITO anode and the evaporated cathode. They are 4mm^2 , 6.45mm^2 and 165mm^2 for the small 6 pixel, large 36 pixel and large 4 pixel architectures respectively. As discussed in the previous two chapters, the large 36 pixel architecture allows investigations into film variations over a larger device substrate area, as the pixel sizes are relatively similar to those of the smaller architecture. The large 4 pixel can be employed for investigations into the effect of increased pixel size on device performance, without the substantial increase in resistance seen for the large single pixel substrate in Chapter 4.

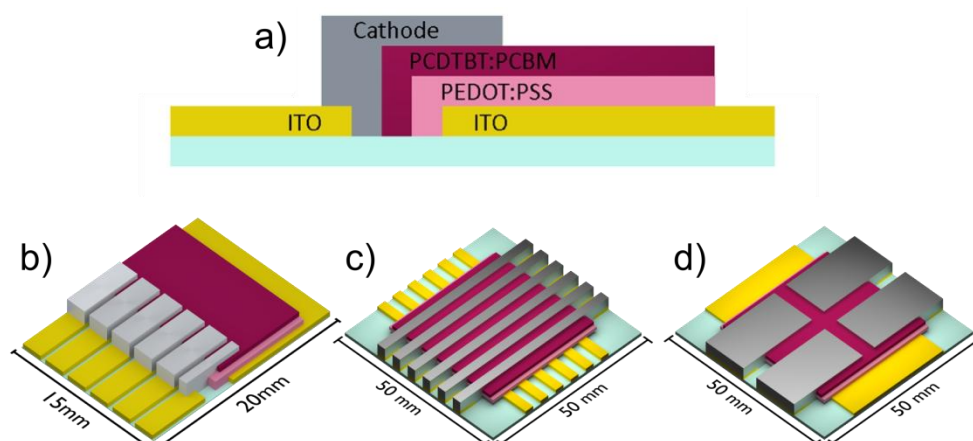


Figure 6-4: Simplified schematics showing the vertical structure of the OPV devices (a) along with small 6 pixel (b), large 36 pixel (c) and large 4 pixel (d) device architectures. Pixel sizes of the various architectures are 4mm^2 , 6.45mm^2 and 165mm^2 for the small 6, large 36 and large 4 architectures respectively.

The materials and thicknesses of the materials in the stack are as follows: ITO/PEDOT:PSS/PCDTBT:PC₇₀BM/Ca (5 nm)/Al (100 nm). The thickness of the PEDOT:PSS and PCDTBT:PC₇₀BM layer will vary throughout the chapter. The

substrate cleaning procedure, evaporation and encapsulation are described in Chapter 3. The substrate to nozzle distance was 40 mm and 65 mm for small and large substrate architectures respectively. Spray parameters are as described in this chapter. After initial spraying of the PEDOT ink at 20°C, the substrates were then transferred to a hotplate held at 120°C. Reference PEDOT:PSS films were spin-cast at 5000rpm and the photoactive layer was then spin-cast at 1200rpm or spray-cast using optimised conditions as described in Chapter 4.

6.6 Film Thickness

Figure 6-5a shows scanned images of PEDOT:PSS films spray-cast from a solution of PEDOT:PSS, IPA and EG in ratios of 1:8:1. The decrease in the PEDOT:PSS component of the blend (from 2:7:1) was to further reduce the water content in a given volume and increase the stage one evaporation time. The films were spray-cast at varying speeds resulting in a spread of film thicknesses and scans were taken using an Epson Perfection V370 scanner. Figure 6-5b shows a manipulated version that enhances contrast in order to distinguish the transparent films. Films appear smooth and continuous until spray speeds reach as low as 40 mm⁻¹. Final film thickness varies over the surface. Profilometer depth measurements of the film cast at 40 mm⁻¹ show a difference in thickness of 57 nm to 100 nm over the substrate surface. This variation is due to a large amount of ethyl glycol present on the surface after the IPA has evaporated. During the transfer from the spray coater to the hot plate, the solution readily flows around the substrate surface as discussed above. This effect can be lessened by depositing a lower volume of solution. The desired thickness of a PEDOT:PSS layer in an OPV has been shown to be ~30 nm. The corresponding spray speed is well within the limits of poor film uniformity imposed by the solution drying time.

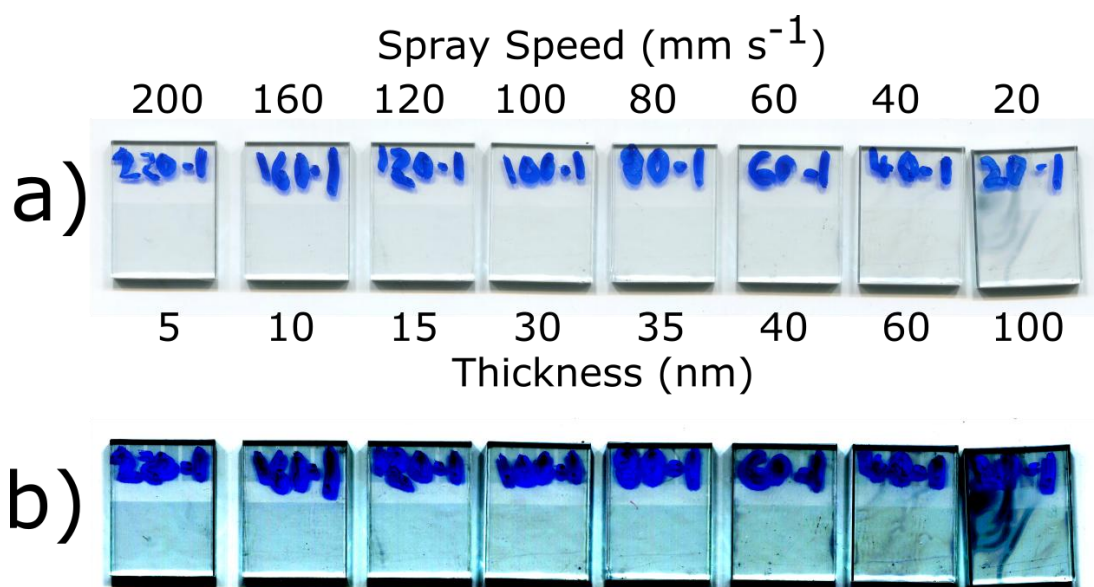


Figure 6-5: Scanned images showing a) PEDOT:PSS films spray-cast at various spray speeds from PEDOT:PSS, IPA and EG in a ratio of 1:8:1. There is a large variation in film thickness for spray speeds $<40 \text{ mms}^{-1}$. b) shows a) with a higher contrast, in order to distinguish the transparent films.

PEDOT:PSS films were spray-cast onto ITO substrates at various speeds to create a variation in film thickness and a spin-cast reference was deposited. A PCDTBT:PC₇₀BM photoactive layer was then spin-cast from a chlorobenzene solution with a concentration of 25 mg ml^{-1} at a speed of 1200rpm, creating a 70 nm thick layer. Device preparation proceeded as described in section 6.5. Figure 6-6 shows the performance characteristics of the fabricated devices, along with a spin-cast reference. The spray-cast PEDOT:PSS performs well, showing a slight decrease in short circuit current density as film thickness decreases, likely due to a reduction in hole transport. Overall the thickness of the PEDOT:PSS layer did not seem to greatly alter the final device performance, unlike the vanadium oxide in Chapter 5 which relied heavily on achieving the optimum thickness. A large thickness threshold is desirable during the scale up process, as variations in thickness will not reduce yield as much.

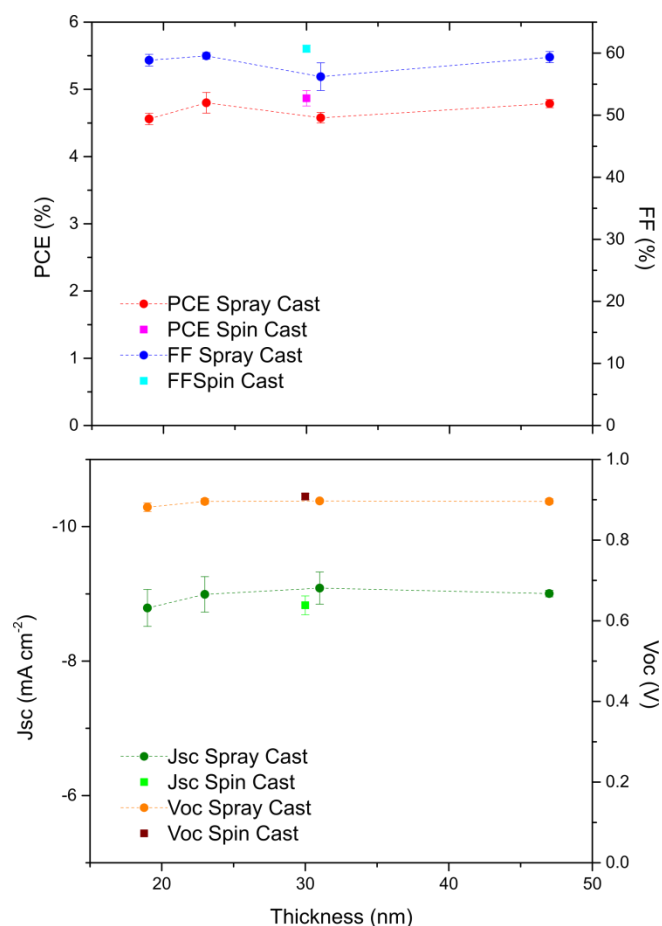


Figure 6-6: Performance characteristics of OPV devices fabricated with spray-cast PEDOT:PSS layers of varying thickness. PEDOT:PSS blend ratio was 1:8:1 and films were deposited at 20°C before being transferred to a hotplate held at 120°C.

6.7 Film Uniformity

When PEDOT:PSS is used as a hole transport layer in an OPV devices, it is usually deposited between an ITO anode and a solution processed photoactive layer. It should therefore ideally provide a smooth surface on which the layer above it can be deposited. A PEDOT:PSS film was spray-cast from a solution of PEDOT:PSS, IPA and ethyl glycol at a ratio of 1:8:1 and a deposition speed of 80 mms⁻¹. Dry film thickness was 30 nm, an appropriate thickness for a PEDOT:PSS hole transport layer. Atomic force microscopy was used to characterise the film surface, as displayed in Figure 6-7. This film has a root-mean-squared (rms) roughness of 2.57 nm and a uniformity of ± 12 nm over an area of 100 μm^2 .

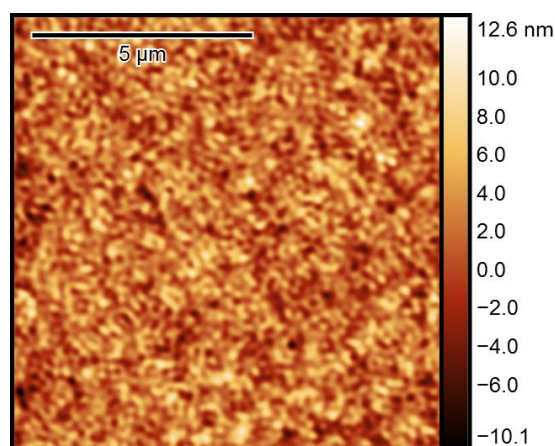


Figure 6-7: Atomic force microscopy image of a spray-cast PEDOT:PSS film. The deposition ink consisted of PEDOT:PSS, IPA and ethylene glycol in a ratio of 1:8:1. The film has an rms roughness of 2.57 nm and a uniformity of ± 12 nm over an area of $100 \mu\text{m}^2$.

The rms roughness is only $\sim 9\%$ of the thickness of the PEDOT:PSS layer. As seen in Section 6.6, such a small variation is unlikely to significantly alter performance.

6.8 Spray coating PEDOT:PSS and PCDTBT:PC₇₀BM

In previous sections of this chapter demonstrated devices fabricated via the spray coating of PEDOT:PSS hole transport layers, while the PCDTBT:PC₇₀BM layer was spin-cast. If the spray coating technique is to be roll to roll compatible, both layers must be spray-cast sequentially. Spin and spray-cast PEDOT:PSS devices were fabricated as described in Section 6.6, however the PCDTBT:PCBM layer was spray-cast from a solution of concentration 8 mg ml^{-1} instead of spin-cast as previously. The PCE results of this fabrication run are displayed in Figure 6-8. Devices in which both layers are spray-cast have similar power conversion efficiencies to those in which only the active layer was spray-cast.

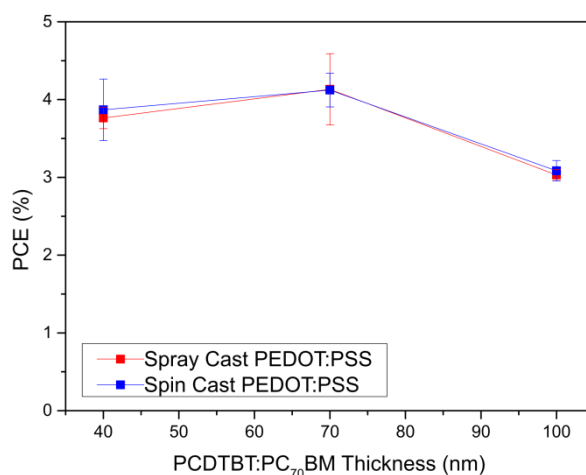


Figure 6-8: Power conversion efficiency as a function of spray-cast active layer thickness for devices fabricated with spin-cast and spray-cast PEDOT:PSS layers.

Table 6-2 shows the performance characteristics of the spray cast PEDOT:PSS devices from Figure 6-8. There is a reduction in efficiency at higher film thickness which appears to be due to a reduction in FF. It has been shown that the FF of a PCDTBT:PC₇₀BM device reduces when the thickness of the film increases over 70 nm due to increased carrier recombination. This is therefore suggested as the loss mechanism in this study.

PCDTBT:PC ₇₀ BM Thickness	PCE (Average)	FF	J _{sc}	V _{oc}
nm	%	%	mA cm ⁻²	V
40	3.87 ± 0.39	54.5 ± 2.8	-8.29 ± 0.3	0.85 ± 0.02
70	4.12 ± 0.22	49.7 ± 1.4	-9.43 ± 0.3	0.88 ± 0.01
100	3.08 ± 0.13	42.2 ± 2.3	-8.31 ± 0.48	0.88 ± 0.01

Table 6-2: Performance characteristics of the devices shown in Figure 6-8.

6.9 Scale Up

This section investigates the effect of scale up on the uniformity and performance of the spray-cast PEDOT:PSS film. Devices were fabricated and characterised using the large 36 pixel and large four pixel architecture designs, as shown in Figure 6-4(c) and (d) respectively.

6.9.1 Large 36 Pixel

The individual pixel sizes of the 36 pixel architecture are similar in size (6.45 mm^2 to 4 mm^2) to those of the small 6 pixel substrates used previously in this chapter. This allows for a study of layer uniformity over a larger device area, without needing to account for the detrimental effects of scaling pixel size. This architecture is therefore used during the first stage of the scale up process.

PEDOT:PSS layer was spray-cast on to a 25 cm^2 36 pixel ITO substrate held at a temperature of 20°C from a solution of PEDOT:PSS, IPA and EG at a ratio of 1:8:1. The sample was then transferred on to a hot plate held at 120°C to evaporate the remaining ethylene glycol. The spray speed was 80 mm s^{-1} and the resulting film thickness was 30 nm. A PCDTBT:PCBM photoactive layer was then spray-cast at 40°C from a chlorobenzene solution with a spray speed of 100 mm s^{-1} to create a 60 nm thick film. Device fabrication then proceeded as described in section 6.5. Devices were characterised using a solar simulator and shadows masks as described in Chapter 3. Figure 6-9 shows the performance characteristics of the spin-cast and spray-cast PEDOT:PSS devices. There is a large reduction in open circuit voltage and fill factor in the devices fabricated via spray coating. The short circuit current does not decrease however, performing better than the spin-cast reference.

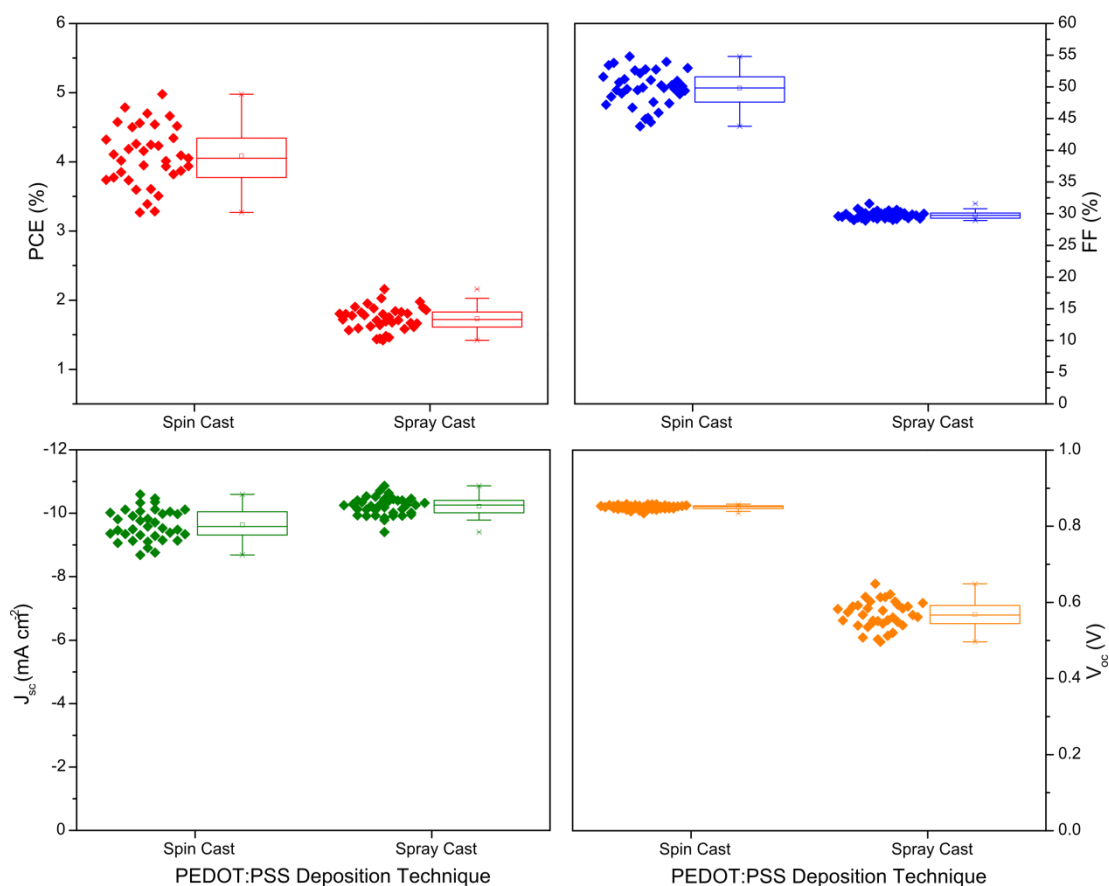


Figure 6-9: Box charts of 36 pixel devices with PEDOT:PSS layers deposited via spin-casting or spray coating. In both cases, the PCDTBT:PC₇₀BM active layer was spray-cast.

This can be explained by a combination of the 36 pixel device geometry and a change in PEDOT:PSS conductivity between the spin-cast and spray-cast films. Several studies have shown that the treatment of a PEDOT:PSS film with EG can increase its interchain and intrachain carrier mobility [7]. The 36 pixel device operates on the principle that each ITO strip is electrically insulated from the other as shown in Figure 6-10. Each crossing of the ITO and the cathode material create a device pixel. Current is prevented from travelling laterally between the electrode strips by large gaps.

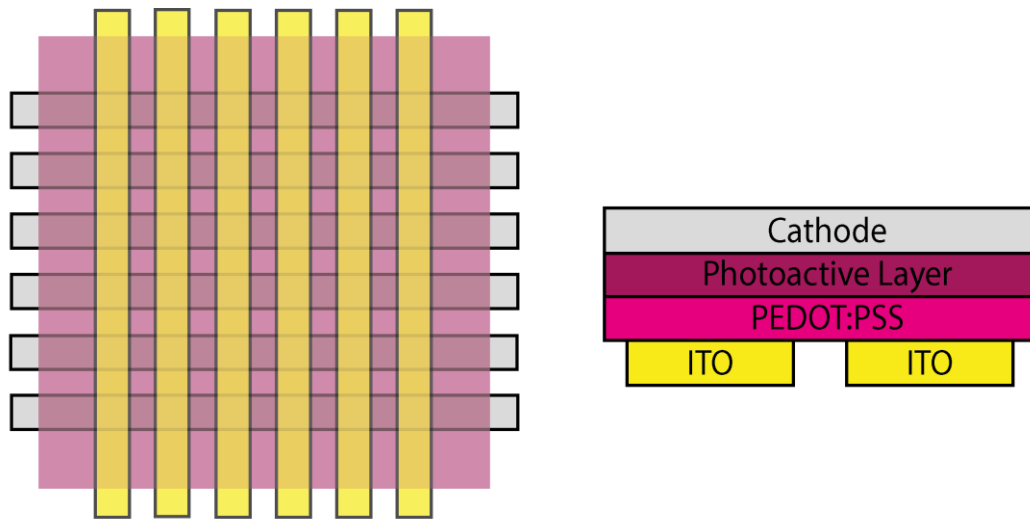


Figure 6-10: Anode and cathode materials crossing in a 36 pixel substrate, wherein each crossing forms a pixel.

If the PEDOT:PSS acts as a conductive material, this can essentially create a single large anode, joining the ITO strips together. If there are any regions where PEDOT:PSS is directly in contact with the cathode material, this can create a short and electrically link the ITO anode with the cathode, bypassing the active layer. Figure 6-11 shows a 36 pixel device covered by a shadow mask used for solar simulator measurements. This mask allows individual pixels to be illuminated independently for testing. Each pixel has a coordinate designated by the letter and number of its anode and cathode strip respectively. Each of these electrode strips is connected to a switch, allowing for J-V measurements of individual sets of strips. If the ITO strips are electrically insulated from one another, illuminating pixel F6 should not result in a measurable photocurrent when connected to strips E and 5 for instance.

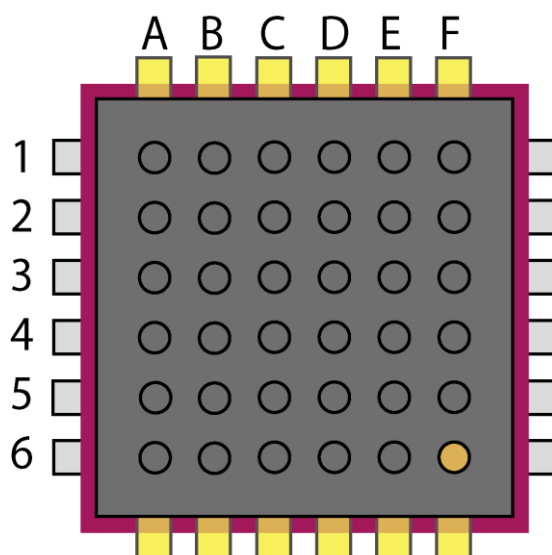


Figure 6-11: A shadow mask covering all but one pixel on a 36 pixel device during a solar simulator measurement.

A series of measurements were taken while pixel F6 was being illuminated, as display in Table 6-3. For a spin-cast device, connecting to the device through ITO strip 'F' and the 6th cathode strip, a non-zero PCE is measured as expected. When connecting via ITO strip 'E' and the 6th cathode strip however, there is zero photocurrent measured. When the process is repeated for the spray-cast device however, a photocurrent can still be measured when connected to an entirely different ITO strip. This extends all the way to ITO strip 'A', 3 cm from the ITO strip being illuminated. The conductive PEDOT:PSS in the spray-cast device is creating a bridge between ITO strips across the substrate, creating a single large anode.

Strips Connected		Measured PCE (%)	
Cathode	Anode	Spin-cast	Spray-cast
Left 6	Top F	3.94	1.65
Left 6	Top E	0.00	0.78
Left 6	Top D	0.00	0.55
Left 6	Top C	0.00	0.49
Left 6	Top B	0.00	0.44
Left 6	Top A	0.00	0.39

Table 6-3: Measured PCE of pixel F6 for two 36 pixel devices with spin-cast and spray-cast PEDOT:PSS layers, when connected via various anode and cathode combinations.

The conductivity of the spin-cast and spray-cast PEDOT:PSS films were measured by Mr Yiwei Zhang to be 0.0023 S cm^{-1} for the spin-cast films and 4.45 S cm^{-1} for the spray-cast films; an increase of three orders of magnitude. While conductive PEDOT:PSS is usually desirable due to its charge carrying ability, it renders this particular device architecture ineffective. More devices were fabricated, using the same experimental method as previously, however the PEDOT:PSS layer was wiped off between the electrode strips using a fine-tipped cotton bud, as shown in Figure 6-12. This created 'islands' of PEDOT:PSS, insulating the individual pixels once again.

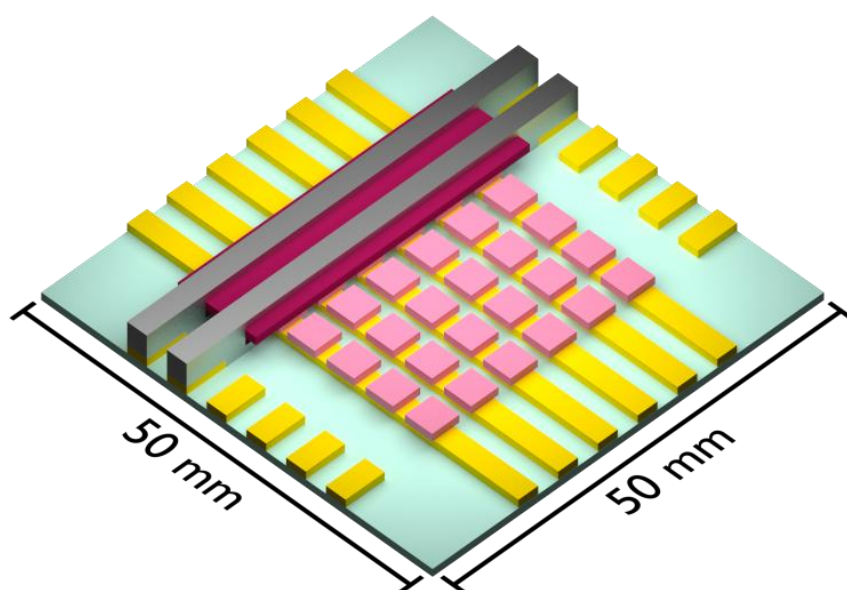


Figure 6-12: A 26 pixel device with a portion of the photoactive layer and top cathode removed, showing the wiped PEDOT:PSS layer.

The performance characteristics of the 'wiped' device are displayed in Figure 6-13. There is no longer a drop in open circuit voltage when spray coating the PEDOT:PSS layer. The fill factor is inconsistent between pixels however, indicating resistance issues within the cell.

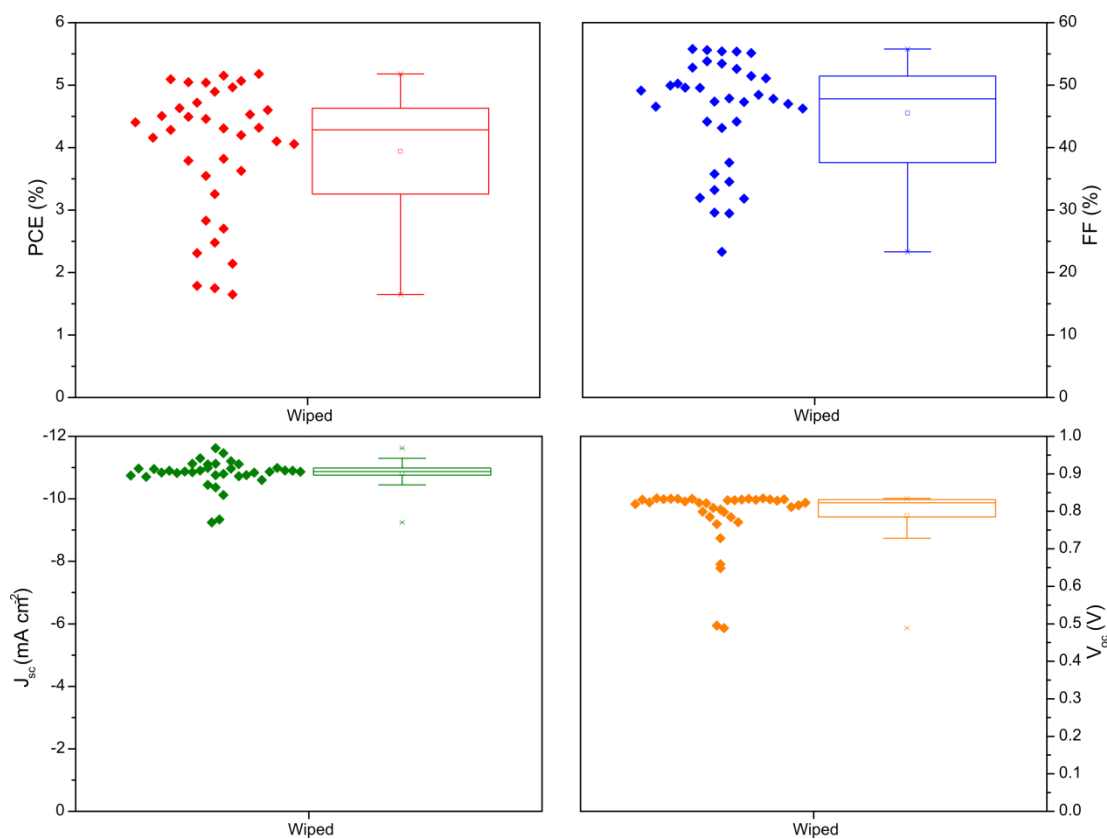


Figure 6-13: Performance characteristics of a 36 pixel device fabricated via spray coating the PEDOT:PSS layer and wiping the final film between pixels. The PCDTBT:PC₇₀BM layer was also spray-cast.

In order to investigate the versatility of the spray-cast PEDOT:PSS process, a different donor:acceptor system was deposited as the photoactive layer in large 36 pixel device. The high-performing polymer poly[4,8-bis(5-(2-ethylhexyl)thiophen-2-yl)-benzo[1,2-b;4,5-b']dithiophene-2,6-diyl-alt-(4-(2-ethylhexyl)-3-fluorothiopheno[3,4-b]thiophene)-2-carboxylate-2,6-diyl)] (PBDTTT-EFT) has been shown to achieve efficiencies of over 9% [8]. A separate material system provides an opportunity to investigate the versatility of the deposition technique.

A large-area PEDOT:PSS film was prepared as described earlier in this chapter and the film was wiped away between electrodes. PBDTTT-EFT was blended with PCBM at a ratio of 1:1.5 and dissolved in chlorobenzene and a DIO additive of 3%. The solution was spray-cast on top of the PEDOT:PSS film and devices were fabricated as described in section 6.5. Active layer deposition and subsequent device fabrication and testing were performed by Yiwei Zhang. Reference samples were also prepared,

wherein PBDTTT-EFT was spray-cast on to spin-cast PEDOT:PSS film. Table 6-4 displayed performance characteristics of the large area devices fabricated. There is a remarkable similarity in performance between the devices with spin and spray-cast PEDOT:PSS layers. These results were published by Yiwei Zhang in reference and at the time of writing are the highest reported efficiencies of OPVs fabricated via the spray coating process. [9].

Deposition Technique	PCE	FF	J_{sc}	V_{oc}
	(%)	(%)	(mA cm^{-2})	(V)
Spin-cast	7.7 ± 0.6	65 ± 2.2	15.7 ± 0.8	0.77 ± 0.09
Spray-cast	7.5 ± 0.3	65 ± 2.1	15.2 ± 0.3	0.77 ± 0.04

Table 6-4: Performance characteristics of 36 pixel devices fabricated via spray coating PBDTTT-EFT on to spin-cast and spray-cast PEDOT:PSS films.

This material system has been shown to achieve PCEs of over 9% when fabricated inside a glove box environment [8]. The result above is promising, as being able to process materials in air while maintaining high efficiencies is crucial for large scale fabrication. A high film uniformity of a large area is also a desirable result and this is also achieved.

6.9.2 Large Four Pixel

A large four pixel substrate architecture allows for a study of how scaling pixel size affects device performance. For the technology to progress to commercialisation, pixel sizes must be increased so as to harvest as much light as possible for a given panel area. A PEDOT:PSS layer was spray-cast on to two large 4 substrate designs from a solution of PEDOT:PSS, IPA and EG at a ratio of 1:8:1. A PCDTBT:PC₇₀BM layer was spray-cast on top of this, and devices were fabricated as described in section 6.5. J-V curves of a large 4 pixel and a small 6 pixel device are displayed in Figure 6-14 and performance characteristics are displayed in Table 6-5. The data displayed includes all eight pixels fabricated on the two large substrates, instead of the top 50% used for the smaller substrates. As discussed in Chapter 5, device yield is an important metric when scaling up manufacture, therefore even very poorly performing pixels are important to note.

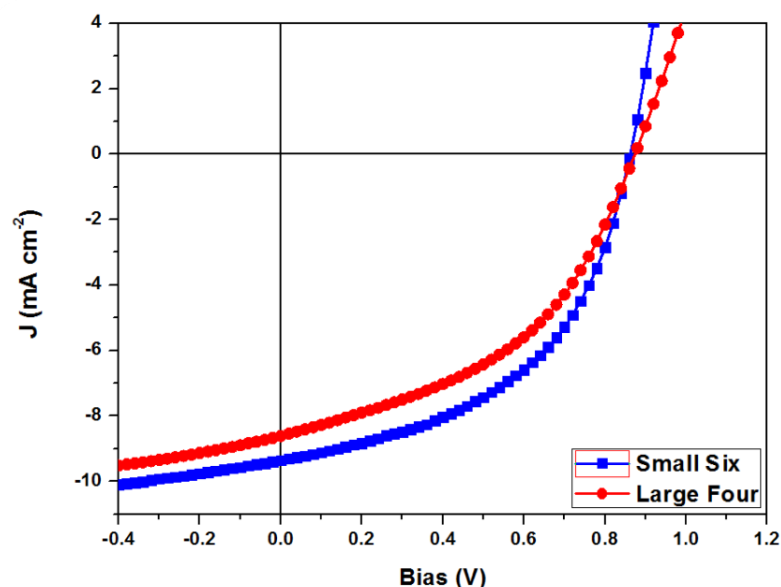


Figure 6-14: J-V characteristics of OPV devices fabricated using the small six and large 4 device architectures shown in Figure 6-4. Both the PEDOT:PSS hole transport layer and the PCDTBT:PC₇₀BM photoactive layer were spray-cast.

There is a decrease in short circuit current density as the area of the pixel increases. This is likely due to an increase in series resistance losses due charges having to travel further through the ITO anode [10]. The resistance of uncoated large and small area ITO substrates was measured from the centre of the pixel to the anode contacts at the substrate edge. These distance were 10 mm and 19 mm for the small and large substrates respectively. The resistance of the small substrate was found to be 29 Ω , while the large substrate had a resistance of 40 Ω . The resistance of the large substrate is therefore 1.4 times that of the small. This is in agreement with the series resistance of the devices calculated from the averaged JV data. 31.3 is 1.8 times 17.1, which explains some of the losses associated with the scale up. Voc is primarily dependent upon the work function of the electrodes and the donor-acceptor energy difference, it is expected to be independent of device area [12], as is seen here. This is promising, as it implies that the vertical structure of the cell is relatively unchanged between the small area and large area devices. In practice the resistance of the ITO substrate can be improved using bus bars or metallic grids and the substrate architecture can be altered to reduced the pixel - contact distance

[11]. This reduction in efficiency therefore may not be an inherent part of the scale up process.

Pixel Size mm ²	Max PCE (%)	FF (%)	J _{sc} (mAcm ⁻²)	V _{oc} (V)	R _{shunt} (Ω cm ²)	R _{series} (Ω m ²)
4	4.12 ± 0.22	49.7 ± 1.4	-9.43 ± 0.3	0.88 ± 0.01	452	17.1
165	3.36 ± 0.24	44.7 ± 0.91	-8.62 ± 0.68	0.87 ± 0.01	319	31.3

Table 6-5: Performance characteristics of fully spray-cast devices for the small 6 and large 4 device architectures.

These efficiencies are still below what it possible with this material system however, and more work must be done to improve film uniformity. Figure 6-15 shows photographs of fully fabricated devices using the small 6 and large 4 pixel architectures. The active layer appears mottled, with film uniformity changes on the order of millimetres. This could be due to mass transfer of polymer material, as the drying edge of the film pulls some material along with it.

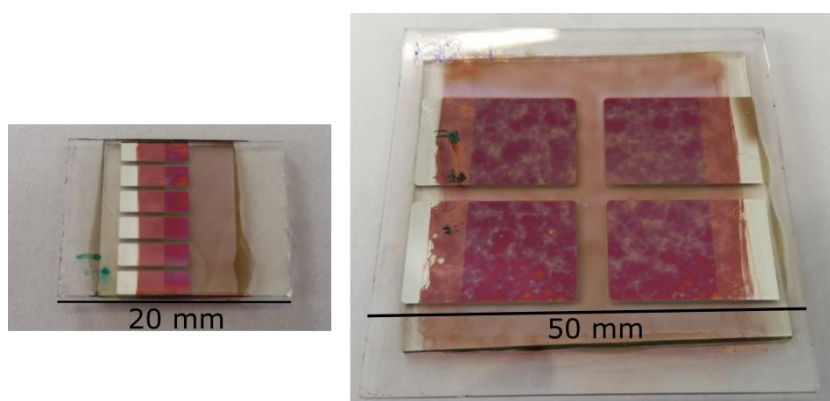


Figure 6-15: A photograph displaying the small 6 pixel and large 4 pixel architectures after full fabrication.

Light beam induced current mapping was performed on a large fully spray-cast pixel, and is shown in Figure 6-16(a). There is a clear fluctuation in photocurrent over the 'mottled' areas as a variation in film thickness alters the photocurrent generation of the cell.

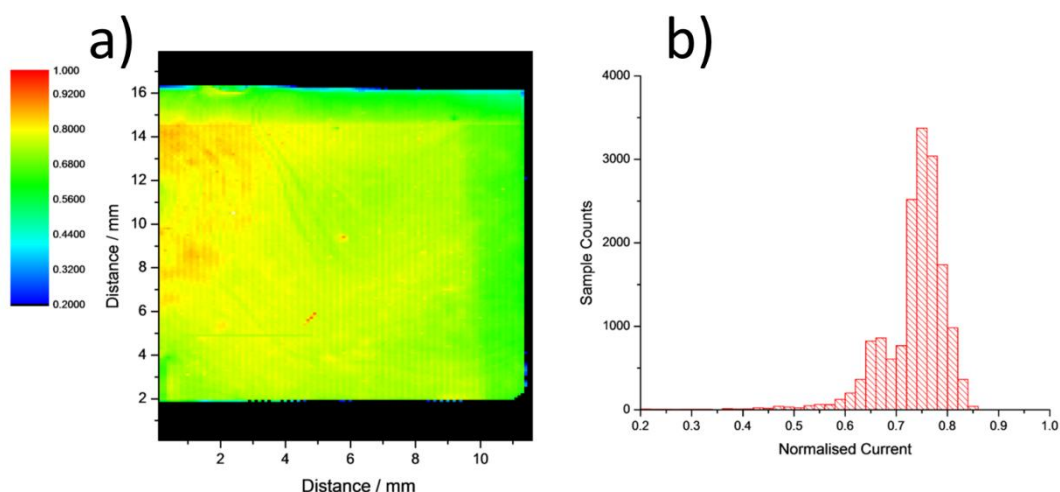


Figure 6-16: Part (a) shows laser beam induced current map of a large 4 architecture pixel, with part (b) showing a histogram of the photocurrent data shown in part (a).

Figure 6-16(b) shows a histogram of the photocurrent in (b). The lower values are not shown, as these are from the ‘dead’ area surrounding the pixel. There is a variation in photocurrent generation of 10 – 20 % across the cell. This variation in photocurrent across a single pixel is larger than the variation of J_{sc} in Table 6-5 across both substrates (8%). This implies that there are film fluctuations on the pixel scale of 165 mm^2 which are evened out at the substrate scale of 900 mm^2 . This can be seen in Figure 6-15, where the mottled effect is fairly uniform over the whole surface. If photocurrent generation can be improved on the pixel-scale by reducing the mottling, the scale up process will become more effective.

The work on scale-up of PCDTBT:PC₇₀BM and PEDOT:PSS cells discussed in this chapter was published in reference [11].

6.10 Conclusion

An aqueous ink of the hole transport material PEDOT:PSS was combined with IPA and EG to aid wetting on to an ITO surface. OPV devices were then fabricated via spray casting the PEDOT:PSS layer and spin casting a PCDTBT:PC₇₀BM active layer, achieving efficiencies of ~5%. PCDTBT:PC₇₀BM and PBDTTT-EFT:PC₇₀BM layers were also spray cast during fabrication, creating devices with no spin cast layers. The

spray coating process was then called up to larger substrate areas, and large device architectures were employed. A 36 pixel architecture achieved similar results to the small device sizes, indicating that the film is unchanged when spray cast over a larger area. A high PCE of over 7.5% was achieved for the ‘fully’ spray-cast large area PBDTTT-EFT devices. A large four pixel device structure showed a decrease in performance when compared with the small area devices, potentially due to increased ITO resistance and a mottling effect created by the drying film.

6.11 References

- [1] E. Bovill, N. Scarratt, J. Griffin, H. Yi, A. Iraqi, A. R. Buckley, J. W. Kingsley, and D. G. Lidzey, “The role of the hole-extraction layer in determining the operational stability of a polycarbazole:fullerene bulk-heterojunction photovoltaic device,” *Appl. Phys. Lett.*, vol. 106, no. 7, p. 073301, Feb. 2015.
- [2] C. N. Hoth, R. Steim, P. Schilinsky, S. a. Choulis, S. F. Tedde, O. Hayden, and C. J. Brabec, “Topographical and morphological aspects of spray coated organic photovoltaics,” *Org. Electron. physics, Mater. Appl.*, vol. 10, no. 4, pp. 587–593, Jul. 2009.
- [3] K. X. Steirer, J. J. Berry, M. O. Reese, M. F. a. M. van Hest, A. Miedaner, M. W. Liberatore, R. T. Collins, and D. S. Ginley, “Ultrasonically sprayed and inkjet printed thin film electrodes for organic solar cells,” *Thin Solid Films*, vol. 517, no. 8, pp. 2781–2786, Feb. 2009.
- [4] S.-I. Na, B.-K. Yu, S.-S. Kim, D. Vak, T.-S. Kim, J.-S. Yeo, and D.-Y. Kim, “Fully spray-coated ITO-free organic solar cells for low-cost power generation,” *Sol. Energy Mater. Sol. Cells*, vol. 94, no. 8, pp. 1333–1337, Aug. 2010.
- [5] C. Girotto, D. Moia, B. P. Rand, and P. Heremans, “High-Performance Organic Solar Cells with Spray-Coated Hole-Transport and Active Layers,” *Adv. Funct. Mater.*, vol. 21, no. 1, pp. 64–72, Jan. 2011.
- [6] D. R. Lide, “CRC Handbook of Chemistry and Physics, 84th Edition, 2003-2004,” *Handb. Chem. Phys.*, vol. 53, p. 2616, 2003.
- [7] J. Ouyang, C. W. Chu, F. C. Chen, Q. Xu, and Y. Yang, “High-conductivity poly(3,4-ethylenedioxythiophene):poly(styrene sulfonate) film and its application in polymer optoelectronic devices,” *Adv. Funct. Mater.*, vol. 15, no. 2, pp. 203–208, 2005.

- [8] W. Huang, E. Gann, L. Thomsen, C. Dong, Y.-B. Cheng, and C. R. McNeill, "Unraveling the Morphology of High Efficiency Polymer Solar Cells Based on the Donor Polymer PBDDTT-EFT," *Adv. Energy Mater.*, vol. 5, no. 7, p. n/a–n/a, Apr. 2015.
- [9] Y. Zhang, J. Griffin, N. W. Scarratt, T. Wang, and D. G. Lidzey, "High efficiency arrays of polymer solar cells fabricated by spray-coating in air," *Prog. Photovoltaics Res. Appl.*, p. n/a–n/a, 2015.
- [10] W.-I. Jeong, J. Lee, S.-Y. Park, J.-W. Kang, and J.-J. Kim, "Reduction of Collection Efficiency of Charge Carriers with Increasing Cell Size in Polymer Bulk Heterojunction Solar Cells," *Adv. Funct. Mater.*, vol. 21, no. 2, pp. 343–347, Jan. 2011.
- [11] N. W. Scarratt, J. Griffin, T. Wang, Y. Zhang, H. Yi, A. Iraqi, and D. G. Lidzey, "Polymer-based solar cells having an active area of 1.6 cm² fabricated via spray coating," *APL Mater.*, vol. 3, no. 12, 2015.
- [12] S. Choi, W. J. Potscavage, and B. Kippelen, "Area-scaling of organic solar cells," *J. Appl. Phys.*, vol. 106, no. 5, p. 054507, 2009.

Chapter 7 Conclusions and Further Work

7.1 Conclusions

Organic photovoltaic's present a promising technology for the manufacture of cheap, light weight and flexible solar power. The potential of roll-to-roll fabrication techniques are high as large sheets of OPV cells can be printed rapidly onto flexible substrates, unlike more the traditional silicon based technology [1]. More work must be done to improve the quality of printing films and the performance of large-area cells however. Along with device efficiencies, the long term performance and lifetimes of OPV cells must be improved in order to produce a commercially viable technology [2] [3].

A concept roll-to-roll production line has already been demonstrated by Krebs et al. and a resultant 'solar park' installation has been operating for over a year [4].

Out of the many large-scale solution deposition techniques, ultrasonic spray coating offers rapid, low temperature fabrication of a large range of materials. This work aimed to demonstrate the feasibility of ultrasonic spray coating as a technique for the fabrication of low band gap organic photovoltaic devices. All of the solution processed materials in a device stack were spray cast, achieving comparable results to those of spin cast references.

Chapter 4 showed an ultrasonic spray coating process optimised for the deposition of PCDTBT:PC₇₀BM active layers. The ultrasonic spray coater deposition technique was investigated and several deposition parameters were explored. An optimised process is then used to fabricate devices, with a maximum PCE of 4.79% achieved. The process was then applied to a large scale 36-pixel device, achieving a 100% yield and efficiencies above 3.5%. Finally, a 900mm² single pixel is fabricated with a PCE of 1.75% achieved. Light beam induced current maps show a variation in photocurrent generation across the cell.

In **Chapter 5**, a spray coating process was optimised for the metal oxide hole transport layers vanadium oxide and molybdenum oxide. Small-area devices were fabricated and performances matched those of devices with spin cast PEDOT:PSS hole transport layers of around 5% PCE. Film uniformity was characterised via atomic force microscopy and it was found that the vanadium oxide film matches the surface morphology of the ITO substrate on to which it is cast. Large 36 pixel devices were then fabricated, providing high pixel yields of 86% and 89% for vanadium oxide and molybdenum oxide devices respectively.

Chapter 6 described the formulation of an ink for deposition of the hole transport material PEDOT:PSS. By combining an aqueous solution with isopropyl alcohol and ethylene glycol, wetting was improved on an ITO surface. OPV devices were then fabricated via spray casting the PEDOT:PSS layer and spin casting a PCDTBT:PC₇₀BM active layer, achieving efficiencies of ~5%. PCDTBT:PC₇₀BM and PBDTTT-EFT:PC₇₀BM layers were also spray cast during fabrication, creating 'fully' spin cast devices. The spray coating process was then scaled up to larger substrate areas, and large device architectures were employed. 36 pixel architectures achieved similar results to the small device sizes, with the large PBDTTT-EFT devices achieving PCEs of over 7.5%. A large four pixel device structure showed a decrease in performance when compared with the small area devices, potentially due to a mottling effect created by the drying film.

7.2 Further Work

Chapter 4

The mottling effect of spray cast PCDBT:PC₇₀BM causes a decrease in performance across the cell area. Further investigation into the cause of this mottling during drying is required. Further solvent blends and processing conditions can be investigated in order to increase film uniformity. Other photoactive material systems can be spray cast in order to investigate the versatility of the spray coating process.

Chapter 5

While both the vanadium oxide and molybdenum oxide layers performed well when spray cast on large 36-pixel devices, the pixel area was not significantly increased during the investigation. The large pixel architectures employed in chapters 4 and 6 can be used to access film performance over a larger area.

Chapter 6

The performance of PEDOT:PSS over a large area appears to be consistent with that of small area devices. The conductivity of the spray cast layer may aid with this process, and this should be investigated.

New device architectures could be designed, with conductive PEDOT:PSS in mind so as to reduce the impact a higher conductivity has on shunt resistance in the device. The conductive PEDOT:PSS could also potentially be used as a replacement for the ITO anode layer.

7.3 References

- [1] Z. Yin, S. Sun, T. Salim, S. Wu, X. Huang, Q. He, Y. M. Lam, and H. Zhang, "Organic Photovoltaic Devices Using Highly Flexible Reduced Graphene Oxide Films as Transparent Electrodes," *ACS Nano*, vol. 4, no. 9, pp. 5263–5268, Sep. 2010.
- [2] C. H. Peters, I. T. Sachs-Quintana, J. P. Kastrop, S. Beaupré, M. Leclerc, and M. D. McGehee, "High Efficiency Polymer Solar Cells with Long Operating Lifetimes," *Adv. Energy Mater.*, vol. 1, no. 4, pp. 491–494, Jul. 2011.
- [3] S. A. Gevorgyan, M. V. Madsen, H. F. Dam, M. Jørgensen, C. J. Fell, K. F. Anderson, B. C. Duck, A. Mescheloff, E. A. Katz, A. Elschner, R. Roesch, H. Hoppe, M. Hermenau, M. Riede, and F. C. Krebs, "Interlaboratory outdoor stability studies of flexible roll-to-roll coated organic photovoltaic modules: Stability over 10,000h," *Sol. Energy Mater. Sol. Cells*, vol. 116, pp. 187–196, Sep. 2013.
- [4] F. C. Krebs, N. Espinosa, M. Hösel, R. R. Søndergaard, and M. Jørgensen, "25th Anniversary Article: Rise to Power - OPV-Based Solar Parks," *Adv. Mater.*, vol. 26, no. 1, pp. 29–39, Jan. 2014.